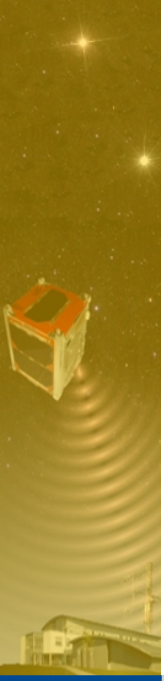

Institut für Informatik
Lehrstuhl für Robotik und Telematik
Prof. Dr. K. Schilling
Prof. Dr. A. Nüchter

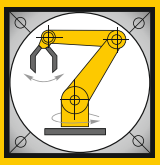

Würzburger Forschungsberichte
in Robotik und Telematik

Uni Wuerzburg Research Notes
in Robotics and Telematics

Julius-Maximilians-
UNIVERSITÄT
WÜRZBURG

Band 19

Dissertation an der Graduate School
of Science and Technology

Philip Bangert

Magnetic Attitude Control of Miniature Satellites and its Extension towards Orbit Control using an Electric Propulsion System

Die Schriftenreihe

wird vom Lehrstuhl für Informatik VII: Robotik und Telematik der Universität Würzburg herausgegeben und präsentiert innovative Forschung aus den Bereichen der Robotik und der Telematik.

Die Kombination fortgeschrittener Informationsverarbeitungsmethoden mit Verfahren der Regelungstechnik eröffnet hier interessante Forschungs- und Anwendungsperspektiven. Es werden dabei folgende interdisziplinäre Aufgabenschwerpunkte bearbeitet:

- Robotik und Mechatronik: Kombination von Informatik, Elektronik, Mechanik, Sensorik, Regelungs- und Steuerungstechnik, um Roboter adaptiv und flexibel ihrer Arbeitsumgebung anzupassen.

- Telematik: Integration von Telekommunikation, Informatik und Steuerungstechnik, um Dienstleistungen an entfernten Standorten zu erbringen.

Anwendungsschwerpunkte sind u.a. mobile Roboter, Tele-Robotik, Raumfahrtsysteme und Medizin-Robotik.

Lehrstuhl Informatik VII
Robotik und Telematik
Am Hubland
D-97074 Wuerzburg

Tel.: +49 (0) 931 - 31 - 86678
Fax: +49 (0) 931 - 31 - 86679

schi@informatik.uni-wuerzburg.de
http://www7.informatik.uni-wuerzburg.de

Dieses Dokument wird bereitgestellt durch den Online-Publikationsservice der Universität Würzburg.

Universitätsbibliothek Würzburg
Am Hubland
D-97074 Würzburg

Tel.: +49 (0) 931 - 31 - 85906

opus@bibliothek.uni-wuerzburg.de
https://opus.bibliothek.uni-wuerzburg.de

ISSN: 1868-7474 (online)
ISSN: 1868-7466 (print)
ISBN: 978-3-945459-28-7 (online)

Zitation dieser Publikation

BANGERT, P. (2019). Magnetic Attitude Control of Miniature Satellites and its Extension towards Orbit Control using an Electric Propulsion System. Schriftenreihe Würzburger Forschungsberichte in Robotik und Telematik, Band 19. Würzburg: Universität Würzburg.
URN: urn:nbn:de:bvb:20-opus-177020

Dissertation an der Universität Würzburg im Rahmen der Graduate School of Science and Technology

Julius-Maximilians-Universität Würzburg
Graduate School of Science and Technology

Doctoral thesis / *Dissertation*

for the doctoral degree / *zur Erlangung des Doktorgrads*

Doctor rerum naturalium (Dr. rer. nat.)

Magnetic Attitude Control of Miniature Satellites and its Extension towards Orbit Control using an Electric Propulsion System

Magnetische Lageregelung von Kleinstsatelliten und ihre Erweiterung zur Orbitregelung durch die Integration eines Elektrischen Antriebssystems

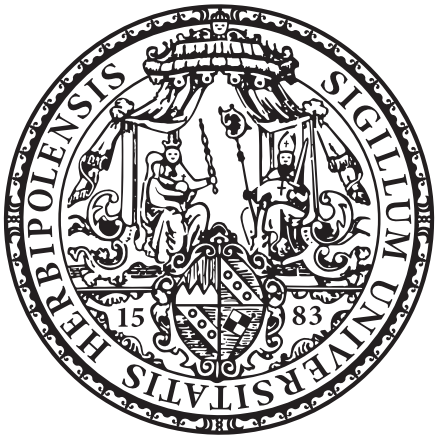

Submitted by / *Vorgelegt von*

Philip Bangert

from / aus

Darmstadt

Würzburg, 2018

Submitted on / *Eingereicht am:*	03.07.2018
Members of thesis committee / *Mitglieder des Promotionskomitees*	
Chairperson / Vorsitz:	Prof. Dr. Werner Porod
1. Reviewer and Examiner / *1. Gutachter und Prüfer:*	Prof. Dr. Klaus Schilling
2. Reviewer and Examiner / *2. Gutachter und Prüfer:*	Prof. Dr. Sergio Montenegro
3. Examiner / *3. Prüfer:*	Prof. Dr. Moshe Guelman
Day of thesis defense / *Tag des Promotionskolloquiums:*	28.11.2018

Abstract

The attitude and orbit control system of pico- and nano-satellites to date is one of the bottle necks for future scientific and commercial applications. A performance increase while keeping with the satellites' restrictions will enable new space missions especially for the smallest of the CubeSat classes. This work addresses methods to measure and improve the satellite's attitude pointing and orbit control performance based on advanced sensor data analysis and optimized on-board software concepts. These methods are applied to spaceborne satellites and future CubeSat missions to demonstrate their validity.

An in-orbit calibration procedure for a typical CubeSat attitude sensor suite is developed and applied to the UWE-3 satellite in space. Subsequently, a method to estimate the attitude determination accuracy without the help of an external reference sensor is developed. Using this method, it is shown that the UWE-3 satellite achieves an in-orbit attitude determination accuracy of about 2 °.

An advanced data analysis of the attitude motion of a miniature satellite is used in order to estimate the main attitude disturbance torque in orbit. It is shown, that the magnetic disturbance is by far the most significant contribution for miniature satellites and a method to estimate the residual magnetic dipole moment of a satellite is developed. Its application to three CubeSats currently in orbit reveals that magnetic disturbances are a common issue for this class of satellites. The dipole moments measured are between 23.1 $\mathrm{mA\,m^2}$ and 137.2 $\mathrm{mA\,m^2}$. In order to autonomously estimate and counteract this disturbance in future missions an on-board magnetic dipole estimation algorithm is developed.

The autonomous neutralization of such disturbance torques together with the simplification of attitude control for the satellite operator is the focus of a novel on-board attitude control software architecture. It incorporates disturbance torques acting on the satellite and automatically optimizes the control output. Its application is demonstrated in space on board of the UWE-3 satellite through various attitude control experiments of which the results are presented here.

The integration of a miniaturized electric propulsion system will enable CubeSats to perform orbit control and, thus, open up new application scenarios. The in-orbit characterization, however, poses the problem of precisely measuring very low thrust levels in the order of µN. A method to measure this thrust based on the attitude dynamics of the satellite is developed and evaluated in simulation. It is shown, that the demonstrator mission UWE-4 will be able to measure these thrust levels with a high accuracy of 1 % for thrust levels higher than 1 µN.

The orbit control capabilities of UWE-4 using its electric propulsion system are evaluated and a hybrid attitude control system making use of the satellite's magnetorquers and the electric propulsion system is developed. It is based on the flexible attitude control architecture mentioned before and thrust vector pointing accuracies of better than 2 ° can be achieved. This results in a thrust delivery of more than 99 % of the desired acceleration in the target direction.

Zusammenfassung

Eine präzise Lage- und Orbitregelung stellt derzeit eine der größten Limitierungen der Einsatzmöglichkeiten von Kleinstsatelliten dar. Um zukünftige wissenschaftliche und kommerzielle Missionen auch mit dieser Klasse von Satelliten erfolgreich durchführen zu können, ist eine Leistungssteigerung bei gleichbleibender Größe und Masse nötig. Die vorliegende Arbeit beschäftigt sich mit der Verbesserung des Lageregelungssystems, der Vermessung der Ausrichtgenauigkeit im Orbit und der Herstellung von Orbitregelungskapazitäten mithilfe von fortschrittlicher Sensordatenanalyse und optimierter on-board Software. Die hier entwickelten Methoden wurden an im Orbit befindlichen Satelliten demonstriert und deren Gültigkeit gezeigt.

Neben einer Methode um die typische CubeSat Lageerkennungssensorik im Orbit zu kalibrieren wurde ein Verfahren entwickelt, um die Ausrichtgenauigkeit ohne die Zuhilfenahme eines externen Referenzsensors zu bestimmen. Beide Verfahren wurden mithilfe des UWE-3 Satelliten im Orbit demonstriert.

Die genaue Analyse der Dynamik eines Satelliten gibt Aufschluss über die vorwiegend herrschenden Störmomente. Für Kleinstsatelliten im erdnahen Orbit kann gezeigt werden, dass Störungen aufgrund von statischen magnetischen Verunreinigungen bei Weitem am meisten Einfluss auf die Dynamik des Satelliten haben. In dieser Arbeit wird eine Methode präsentiert, die Daten der Lageerkennung nutzt um das magnetische Dipolmoment eines Kleinstsatelliten zu bestimmen. Mithilfe dieses Verfahrens konnte das Dipolmoment von drei unterschiedlichen CubeSats im Bereicht von $23.1\,\mathrm{mA\,m^2}$ bis $137.2\,\mathrm{mA\,m^2}$ präzise bestimmt werden.

Um die Lageregelungsgenauigkeit zu steigern wird ein Software Konzept präsentiert, welches die bekannten Störungen der Satellitendynamik inherent und energieoptimiert kompensiert. Die Anwendung dieser on-board Software wurde mit UWE-3 in einer Vielzahl von Lageregelungsexperimenten im Orbit demonstriert.

Die Integration von elektrischen Antrieben wird zukünftigen Kleinstsatelliten die Möglichkeit zur Orbitkontrolle geben und damit viele neue Anwendungsszenarien eröffnen. Die Qualifizierung und Vermessung der Triebwerke im Orbit stellt jedoch eine technische Schwierigkeit dar, da Schübe im Bereich von µN gemessen werden müssen. Ein Verfahren zur genauen Bestimmung des Schubs eines solchen Triebwerks basierend auf dessen Auswirkung auf die Satellitendynamik wurde entwickelt und wird hier mit Hilfe von Simulationen für die UWE-4 Mission demonstriert. Es wird gezeigt, dass mit Hilfe von UWE-4 der Schub der Triebwerke mit einer hohen Genauigkeit von 1 % Fehler für Schübe größer 1 µN gemessen werden können.

Eine magnetische Lageregelung unter Zuhilfenahme der elektischen Antriebe stellt das Konzept der hybriden Lage- und Orbitregelung für UWE-4 dar. Die damit erzielbare Leistung hinsichtlich der Ausrichtgenauigkeit sowie Orbitregelung wurde untersucht und ist hier für verschiedene Szenarien gezeigt.

Danksagung

Diese Arbeit wäre ohne die Unterstützung von Vielen nicht möglich gewesen und diesen Menschen möchte ich gerne im Folgenden danken.
Zunächst bedanke ich mich bei Prof. Dr. Klaus Schilling für die Möglichkeit, an den beiden interessanten und lehrreichen Projekten UWE-3 und UWE-4 mitzuwirken. Ich habe die hohe Autonomie bei der Leitung von UWE-4 und der Gestaltung dieser Arbeit, sowie das damit verbundene Vertrauen sehr zu schätzen gewusst. Außerdem möchte ich mich bei Prof. Dr. Sergio Montenegro, Prof. Dr. Moshe Guelman und Dr. Stephan Schröder-Köhne für die fortlaufende Unterstützung während meiner Promotion bedanken.
Der Bau der UWE Satelliten, und damit auch diese Arbeit, wäre nicht möglich gewesen ohne die wertvolle Mitarbeit meines Kollegen Dieter Ziegler, bei dem ich mich auch für die vielen angenehmen und Horizont-erweiternden Gespräche außerhalb der Arbeitszeiten bedanken möchte. Nicht weniger bedeutsam für mich und diese Arbeit war mein ehemaliger Kollege Stephan Busch, ohne dessen Unterstützung und Motivation diese sicher nie entstanden wäre. Ich danke dir, Stephan, dafür, dass du die Rolle meines Mentors so gut ausgefüllt hast!
Außerdem möchte ich mich bei meinen vielen Kollegen an der Uni aber auch am ZfT bedanken, die auf vielfältigste Weise die Projekte unterstützt haben. Besonders bei Alexander Kramer und Slavi Dombrovski möchte ich mich für die unermüdliche Zusammenarbeit, das Durchhaltevermögen auch in schwierigen Situationen und die vielen freundschaftlichen Gespräche auf und nach der Arbeit bedanken!
Darüber hinaus gab es natürlich viele mir sehr wichtige Menschen, die mir den nötigen Ausgleich zur Arbeit geschaffen haben und ohne die das ganze zumindest nicht so viel Spaß gemacht hätte. Da will ich mich vor Allem bei Jesko, David, Olli, Fabi und Alex bedanken – ohne euch Jungs wäre Würzburg nicht dasselbe! Mein Dank gilt auch Max und Sven für die gemeinsam geschaffene Motivation in der Endphase der Promotion.
Einer ganz besonderen Person in meinem Leben bin ich für die vielen schönen Stunden und die fortwährende Motivation in dieser Zeit unendlich dankbar. Tin, ich glaube ohne Dich hätte ich in so mancher schwierigen Situation nicht weiter gemacht und Du hast es geschafft, dass auch ich immer wieder daran geglaubt habe diese Arbeit fertigzustellen. Aber vor Allem habe ich von dir gelernt, immer nach vorne zu schauen und das Gute dort zu suchen!
Zum guten Schluss möchte ich meinen Eltern danken, die mich nicht nur während meines Studiums immer unterstützt haben, sondern auch mit viel Geduld und Aufmerksamkeit während meiner Promotion begleitet haben. Danke, dass Ihr mir das alles hier ermöglicht habt!

Table of Contents

1

Introduction

In this work challenges of the attitude and orbit control system of miniature satellites are addressed. Methods to measure and improve the satellite's pointing performance based on advanced sensor data analysis are presented and their application potential is demonstrated in-orbit on board the University Würzburg Experimental Satellite 3 (UWE-3). Furthermore, a generic attitude control software architecture is presented that allows to flexibly implement and exchange attitude control algorithms on any CubeSat platform and which has been demonstrated in orbit. This architecture also allows to implement an efficient attitude and orbit control system using magnetorquers and an electric propulsion system which shall be demonstrated with the next UWE mission. A method to measure the very low thrust of the electric propulsion system in orbit and thus characterize the propulsion system itself has been developed and is also presented in this work.

1.1 Motivation

The introduction of the CubeSat standard in 1999 has opened a new chapter in the history of space technology with special emphasis on miniaturization (Helvajian and Janson, 2009). In the beginning, this new class of satellites was intended to provide hands-on experience to graduate students to design, build, test, and operate a spacecraft. Soon, attention also by commercial companies was drawn to this type of spacecraft due to their high cost efficiency. In recent years, scientific and commercial applications of CubeSats have become more prominent making use of the short development cycles and frequent launch opportunities as shown in Figure 1.1. Especially since in 2012, when the first CubeSats were placed in orbit from the International Space Station, a large market has evolved around these miniature satellites.

With their increasing use for scientific and commercial missions the requirements

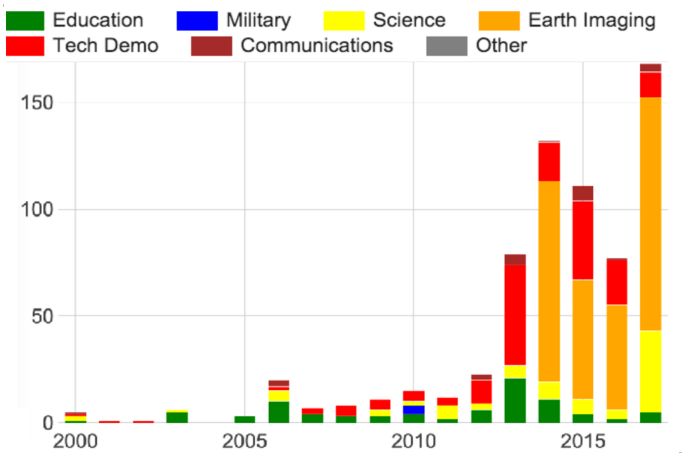

Figure 1.1: Mission type of launched CubeSats (Swartwout, 2017).

towards the small satellites have been increasing over time. While the first CubeSats offered about the same amount of functionality as Sputnik in 1957, modern day CubeSats serve in Earth observation missions, such as Planet Labs' Flock Satellite constellation (European Space Agency: eoPortal – Sharing Earth Observation Resources, 2018c), in astronomy missions such as the BRITE constellation (European Space Agency: eoPortal – Sharing Earth Observation Resources, 2018a), or in RF sensing missions as demonstrated with GOMX-3 (European Space Agency: eoPortal – Sharing Earth Observation Resources, 2018b). All these examples, however, indicate that the original volume restriction of CubeSats to 10x10x10 cm^3 (i.e. 1U CubeSat) did not suffice to fulfill their respective technical requirements. Typically, 3U CubeSats with 10x10x30 cm^3 volume are now the baseline for a large number of missions as shown in Figure 1.2. Since 2014, 3U CubeSats have outnumbered the 1U CubeSats in launches.

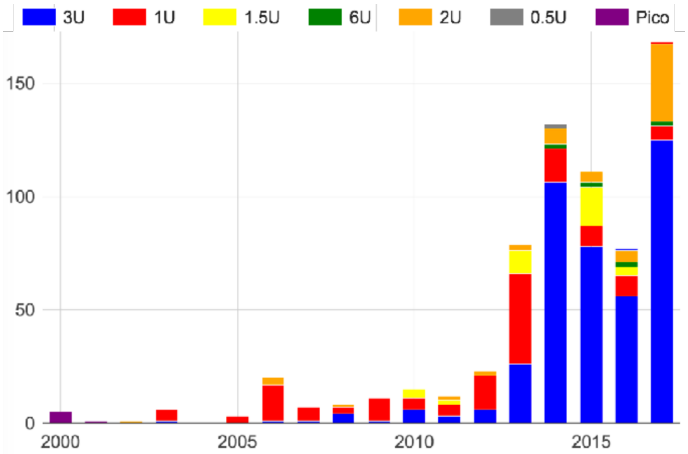

Figure 1.2: CubeSats launched each year by their respective form factor (Swartwout, 2018).

Despite the trend towards larger CubeSats, there are still numerous application scenarios for the smallest class of 1U CubeSats. The implementation of precise attitude and orbit control on this class of satellites is to date an active field of technology development and requires further scientific attention. A performance increase in this respect will open up new application areas for pico-satellites such as cooperative satellite formations, fractionated scientific instruments, and large satellite constellations. The ability to control the satellites' orbit will also enable CubeSats to operate in orbital altitudes that currently are either unavailable for long term operations (due to short orbit lifetime) or do not comply with international regulations (due to too long orbit lifetimes).

The reasons to restrict the satellite size to its absolute minimum are plenty, such as frequent launch opportunities, low cost, low significance for space debris, and last but not least a smaller environmental footprint. Increasing the performance without increasing the satellites' size and mass therefore plays a significant role in the future development of CubeSats.

1.2 Contribution

The work presented here strives to advance the current state of miniature satellite attitude and orbit control by a set of methods applicable to any satellite of this class. The shortcomings due to the miniaturization of sensors and actuators are counteracted by employing advanced data analysis methods and flexible software architectures. The main contributions presented in this work are as follows:

- **An in-orbit sensor calibration procedure and an attitude determination accuracy estimation method.**
  The mass and size restrictions of miniature satellites require to limit the sensor suite of the satellites' attitude determination system to the bare minimum. Thus, sensors such as cameras or star trackers are not available on satellites which do not require this type of instrumentation. The calibration process for the attitude sensor suite therefore cannot rely on such an external reference which also applies to the assessment of the attitude determination accuracy.
  The calibration procedure presented here makes use of inherently available information of the typical CubeSat attitude sensor suite, i.e. magnetometers, sun-sensors, and gyroscopes, and provides the means to calibrate the sensors in orbit. The application of this calibration method is demonstrated with the UWE-3 satellite in orbit and its results are presented.

The attitude determination accuracy estimation presented here is based on analyzing the consistency of the attitude solution with respect to independently calibrated sensor data. The method is applied to UWE-3 and the results are compared to simulations which show the validity of this approach. It is also used to estimate the attitude determination accuracy of the prospective UWE-4 satellite mission.

- **A precise attitude disturbance estimation method.**

  Attitude disturbances are a major risk for miniature satellites because of their limited control capabilities due to the miniaturized actuators. While many typical attitude disturbance torques do not play a significant role for this class of satellites, already a small magnetic uncleanliness can severly corrupt the attitude control system up to the point of mission failure. Magnetic cleanliness, on the other hand, can often not be guaranteed for satellite missions carrying commercial of the shelf components and without access to high-quality materials such as Titanium.

  This work presents a method to precisely estimate a satellite's residual magnetic dipole moment in orbit such that it can be taken into account for attitude control. This method is based on the analysis of the satellite's dynamics and only requires magnetic field and gyroscopic data from the satellite. It has been applied to the UWE-3 satellite as well as to the CubeSats ESTCube-1 and BEESAT-2 to show the significance of the magnetic disturbance.

- **A flexible attitude control software architecture.**

  The introduction of the CubeSat standard has enabled a multitude of institutions and companies to pursue their own space missions with new scientific instrumentation or other specific payloads developed by the teams. Attitude control is a domain strongly linked to the spacecraft bus and the payload at the same time, but often not excelled by the satellite developer.

  The attitude control software architecture developed in this work strives to facilitate operations with the control system and supports a wide range of miniature satellites. It allows flexible exchange of attitude control algorithms and can integrate any available attitude control actuator. The approach divides attitude control in several layers and takes into account any known dynamic effects on the satellite such as disturbance torques. Therefore, the operator can focus on a high level control that fits its mission's purpose while the underlying algorithms optimize the control torque and operate the actuators.

  This architecture has been demonstrated on the UWE-3 satellite in orbit and its ability to cope with the magnetic disturbance torque is presented.

- **A method to estimate the very low thrust of a miniature electric propulsion system.**

  Electric propulsion promises great application potential for miniature satellites. With its typical high mass efficiency already a few grams of propellant can generate a significant orbit maneuverability. The common downside of electric propulsion is its low thrust, but paired with the very low mass of this class of satellites a considerable acceleration can be achieved.

  The development of miniaturized electric propulsion systems is an ongoing research topic in a number of institutions worldwide. To date, no electric propulsion system applicable to a 1U CubeSat has been demonstrated in orbit. Not only the development and integration of this type of thrusters is an open issue but also its characterization in orbit poses extensive difficulties. In order to measure the applied thrust level via a change in the satellite's orbit the propulsion system has to be operated for a long duration and thrust vector pointing needs to be achieved precisely in order not to degrade the thrust estimation. Thus, this method is difficult to achieve with a miniature satellite and a matching propulsion system.

  In this work a method to estimate the thrust produced by a propulsion system is presented that relies on the torque created by such thrusters. The method is applied to the UWE-4 satellite which will carry a newly developed electric propulsion system for 1U CubeSats. It is shown that with this method a precise thrust estimation and thus characterization of the propulsion system is feasible in a short time period.

- **A hybrid attitude and orbit control system.**

  The accommodation of an electric propulsion system for CubeSats also requires attitude control capabilities in order to point the thrust vector accordingly. However, the integration and simultaneous operation of reaction wheels cannot be achieved with the size, mass, and power budgets of a 1U CubeSat. This is especially true considering the necessary long continuous operation times required for orbit control when using a low thrust electric propulsion system.

  Therefore, an attitude control system based on magnetorquers and the electric propulsion system has been developed for UWE-4. It is based on the flexible control software architecture previously developed and optimizes the use of the magnetorquers, thus, minimizing the use of propellant. Its application potential is demonstrated in the context of an attitude control simulation based on two formation flight scenarios.

1.3 Thesis Outline

The thesis at hand is divided into this introduction, four major chapters, and a conclusion. The chapters are complete in themselves in the sense that they provide a short motivation and summary of the content presented. Chapter 6 concludes this document and summarizes the main contribution of this work and the accomplishments achieved. The chapters are organized as follows:

- **Chapter 1: Introduction**
  The introduction to this thesis gives the motivation and broad context for the research presented and states the main contribution to the field. It serves as an outlook to the work itself and gives the reader an overview over the content that can be expected of this work. Furthermore, the thesis outline is presented such that readers can easily navigate to the part they are most interested in.
- **Chapter 2: Sensor Calibration and Attitude Determination**
  The second chapter in this document presents methods to calibrate typical CubeSat attitude sensors in orbit. Special emphasis is on the calibration of the magnetometers that often play the most significant role for miniature satellite attitude determination. These may undergo changes primarily of their static offsets during integration and launch of the satellite and require precise calibration in orbit. The method is applied to the UWE-3 CubeSat and the correct calibration matrices and offsets are found.
  Furthermore, this chapter elaborates on the issue of estimating the attitude determination accuracy in orbit without the help of an external absolute reference sensor. The solution found to this is a consistency analysis comparing the calibrated sensor data with the fused attitude solution computed on-board of the satellite. This approach is verified using a validated attitude dynamics and sensor simulation.
- **Chapter 3: Attitude Disturbance Estimation**
  In this chapter the development of a precise attitude disturbance estimation method is explained. Before elaborating on the algorithm itself a brief overview of the significance of the different attitude disturbance torques is given. Then, the method to estimate the residual dipole moment is presented with its intermediate steps: the oscillation frequency analysis, the smoothing and numeric derivation of noisy sensor data, the numeric optimization and its objective function, and the normalization issue of this approach.
  Eventually, the application of this method to the UWE-3 satellite is presented for which a long term analysis of the residual magnetic dipole moment is performed.

Furthermore, the satellite's magnetorquers are also measured with this approach and compared to their design values.

In order to demonstrate the importance and generality of this method the residual magnetic dipole moments of two other CubeSats are determined. For this, in-orbit data from the ESTCube-1 and BEESAT-2 satellites is evaluated.

As a consequence of this analysis an on-board estimation process of a satellite's residual magnetic dipole moment is developed and presented. Its validity is shown with the help of the verified attitude dynamics and sensor simulation.

- **Chapter 4: Magnetic Attitude Control**

  The fourth chapter introduces a flexible attitude control software architecture and its application to magnetic control with UWE-3. Its emphasis is on the decoupling of dynamic processes in the background and an objective control implemented by the user.

  First, the control architecture is presented in its detail and its different layers are explained. Then, the magnetic attitude control experiments performed with UWE-3 in orbit are shown and discussed. These experiments range from high-rate detumbling of the satellite over rate-control operations to spin-stabilization experiments.

- **Chapter 5: Attitude and Orbit Control Using Magnetic and Electric Actuators**

  This chapter focuses on the integration of the methods and algorithms developed in the previous chapters and presents a hybrid attitude and orbit control system for an electrically propelled 1U CubeSat. The UWE-4 satellite will integrate miniaturized electric thrusters such that it can perform attitude and orbit control together with its magnetorquers at the same time.

  First, the UWE-4 satellite design related to attitude and orbit control is presented. The attitude control system's sensors and actuators are described and its attitude determination performance is estimated using a simulation and the consistency analysis developed in Chapter 2.

  Then, a method to characterize the low thrust propulsion system based on the satellite's attitude dynamics is described and assessed in simulation. The orbit control capabilities of a miniature satellite using such propulsion system is estimated in different scenarios.

  Eventually, the hybrid attitude control making use of magnetorquers and the electric propulsion system is described and its capabilities are presented in two formation

flight application scenarios.

- **Chapter 6: Conclusion**

  The conclusion summarizes the contributions presented in this work and recaps the achievements accomplished. Furthermore, it elaborates on the future perspective of miniature satellites with an advance attitude and orbit control as developed throughout this thesis. Formation flight of miniature satellites is the main focus and future application scenarios for this class of satellites are presented.

2

Sensor Calibration and Attitude Determination

Due to their power, size, and mass restrictions miniature satellites often do not carry more than the most essential sensors for attitude determination. Those consist, for typical Low Earth Orbit missions, of magnetic field sensors and sun-sensors. This set of sensors provides an unambiguous attitude estimation in the sun-lit part of the orbit. Often a sufficiently accurate propagation into the orbit's eclipse can be achieved using an additional angular rate sensor.

However, usually an independent sensor is required for in-orbit calibration procedures and verification of the satellite's attitude estimation solution. Especially for 1U CubeSats, though, a third independent absolute attitude sensor is very difficult to accommodate in the satellite's budgets. Therefore, the development of calibration procedures and algorithms to verify the correct attitude estimation without any additional sensor have been developed.

The calibration procedure primarily makes use of the attitude independent magnetic field strength that is well known through models such as the International Geomagnetic Reference Model (IGRF). The calibrated magnetometers are then used to calibrate the other sensors in order to achieve a consistent Body reference. The procedure is elaborated in Chapter 2.1.

The verification of the satellite's attitude estimation also lacks an external reference. Therefore, a consistency analysis has been developed in order to evaluate the attitude determination accuracy only using the information available from the magnetometer and sun-sensor pair, and the fused attitude estimation. Chapter 2.2 presents this algorithm, its application in the UWE-3 mission, and a simulation that further proves this approach valid.

2.1 In-Orbit Sensor Calibration

The in-orbit calibration of attitude sensors of satellites similar to UWE-3 lacks an external reference that provides an accurate attitude solution by itself. Such reference for instance can be given by a star-tracker or also by post-processing camera data to find the instantaneous camera's pointing as shown by Slavinskis et al. (2016).

If no such sensors are available on the satellite platform a different approach has to be found. Inamori and Nakasuka (2012) report on the calibration of magnetometers and gyroscopes to find scale factors and biases of these types of sensor. Based on this approach, the complete calibration matrix and offset vectors of the magnetometers and gyroscopes of UWE-3 were estimated, taking into account also non-orthogonal entries arising from mounting inaccuracies of the single-axis sensors.

2.1.1 On-Board Reference Model Validation

Before the satellite's attitude sensors can be calibrated, the implemented reference models have to be verified. Therefore, the reference models' output vectors were recorded on UWE-3 for one orbit and compared to the reference on ground.

Shown in Figure 2.1 are the different reference models involved in the attitude determination and control process. Figure 2.1a, Figure 2.1b, Figure 2.1c, and Figure 2.1d show the real-time orbital position and velocity propagation performed by the on-board SGP4 propagator and the relative distance/velocity error with respect to a post-processed SGP4 propagator on ground, respectively. Propagation errors between 10 km to 20 km and up to 0.03 km/s arise due to floating point inaccuracies as well as simplified coordinate system transformations on board but are not critical for the attitude determination accuracy.

This can be seen in Figure 2.1e where the reference magnetic field vector is plotted as it is computed on-board and post-processed on ground. The angular displacement between on-board and on-ground computation is shown in Figure 2.1f and stays well below 1 ° throughout the orbit. Again, the predominant error source is the floating point accuracy of the 16 bit micro-processor and simplified coordinate transformations, in this case resulting from the necessary ECEF to ECI conversion. However, as the attitude determination targets an accuracy of about 5 ° this is of no critical concern.

The Sun-vector model is shown in Figure 2.1g and its angular error to the on-ground computed model in Figure 2.1h. The angular error of the Sun-model is very small ($< 7 \cdot 10^{-4}$°) because there are no coordinate transformations involved in the model computation and little floating point operations.

Overall, the recording shows that the reference models on board of UWE-3 were implemented correctly with the inevitable inaccuracies linked to the computational limitations of the CubeSat.

2.1.2 In-Orbit Magnetometer Calibration

The in-orbit calibration of the magnetometers is based on an analysis of the measured magnetic field strength. This quantity is invariant to rotations of the satellite and thus only changes over the course of the orbit. The task is to find a calibrated magnetic field measurement $\tilde{\mathbf{b}}$ that matches the reference magnetic field strength $|\mathbf{b}_{model}|$ at all times and thus under all rotations of the satellite. The only requirement to apply this procedure is that the satellite is not entirely stabilized about a single axis but rotates about all three axes with respect to the Earth magnetic field such that the magnetic field strength measured along one axis changes over time.

The calibration of the magnetic field sensors of UWE-3 was done prior to launch using a dedicated testbed specifically designed at the University Würzburg (Kiefel, 2011; Kiefel et al., 2011). It consists of a precise turn table which rotates about one fixed axis of which the angular displacement is measured to an accuracy of $0.09\,^{\circ}$ using an optical encoder.

However, the sensors were calibrated after final integration of the satellite and in launch configuration, i.e. the antennas were not deployed during the procedure. The pre-launch calibration did not perform as expected and an accurate attitude determination was not possible using the previously stored configuration. Therefore, an in-orbit calibration was developed being described in the following paragraphs.

Using standard minimization algorithms a calibration matrix C (taking into account gain and cross-axis effects that arise from the fact, that the satellite carries three independent single axis magnetometers) and offset μ can be found such that the measured magnetic field $\mathbf{b}$ can be corrected to produce the calibrated magnetic field

$$\tilde{\mathbf{b}} = C \cdot (\mathbf{b} - \mu) \tag{2.1}$$

while minimizing the error function

$$E = \frac{1}{N} \sum_{i}^{N} \left(|\tilde{\mathbf{b}}_i| - |\mathbf{b}_{model,i}| \right)^2 . \tag{2.2}$$

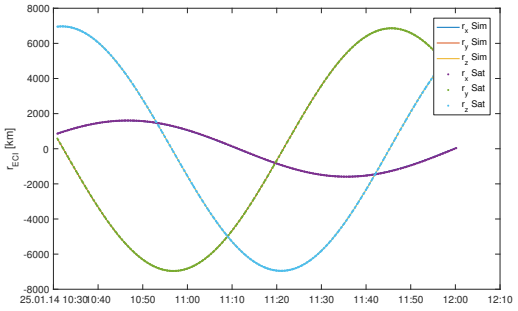

(a) Position vector r_{ECI} as computed by the on-board SGP4-propagator and on ground.

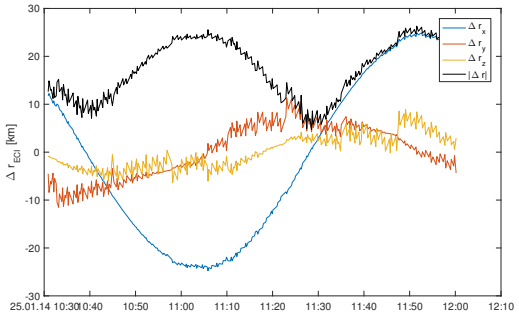

(b) Error of position vector r_{ECI} between the on-board SGP4-propagator and on ground.

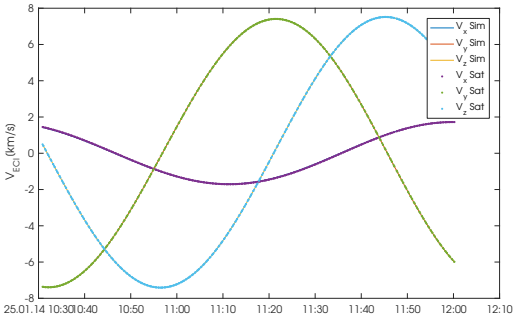

(c) Velocity vector v_{ECI} as computed by the on-board SGP4-propagator and on ground.

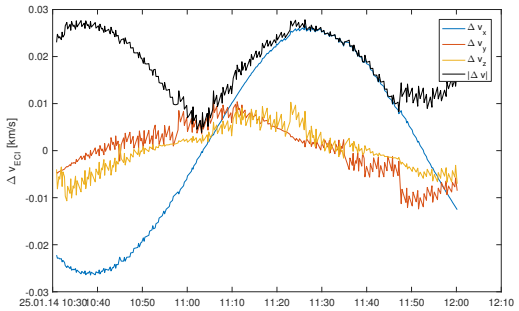

(d) Error of position vector v_{ECI} between the on-board SGP4-propagator and on ground.

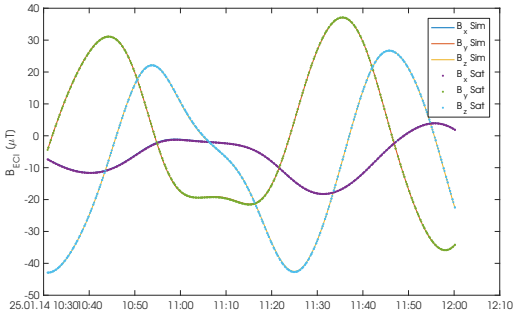

(e) Magnetic field reference vector B_{ECI} as computed by the on-board IGRF model and on ground.

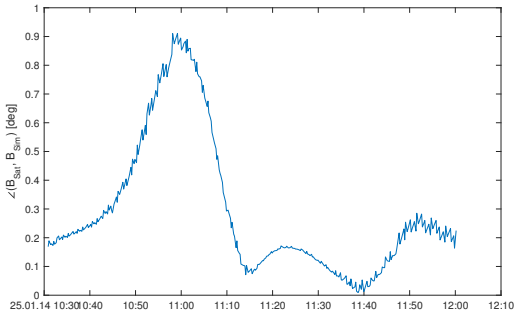

(f) Angle of the magnetic field reference vector B_{ECI} as computed by the on-board IGRF model and on ground.

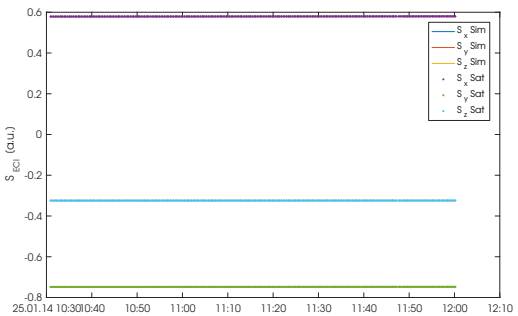

(g) Sun reference vector S_{ECI} as computed on-board and on ground.

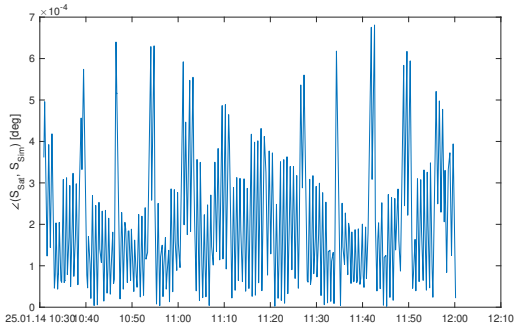

(h) Angle of the Sun reference vector S_{ECI} as computed on-board and on ground.

Figure 2.1: In-orbit reference model verification.

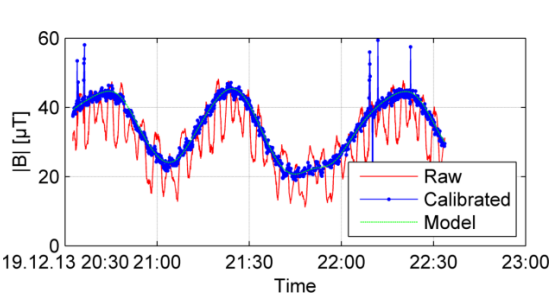

(a) Magnetic field strength before (red) and after (blue) in-orbit calibration.

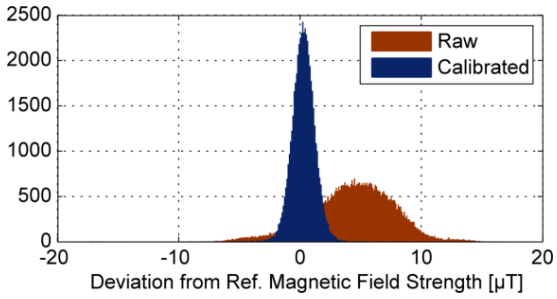

(b) Histogram of the magnetic field strength before (red) and after (blue) in-orbit calibration.

Figure 2.2: Result of magnetometer calibration on magnetic field strength.

The calibration found was

$$\mu = \begin{bmatrix} -6.161 \\ 4.885 \\ 4.045 \end{bmatrix} \mu\text{T} \tag{2.3}$$

and

$$C = \begin{bmatrix} 1.140 & -0.066 & -0.041 \\ 0.063 & 1.141 & 0.013 \\ 0.037 & -0.079 & 1.081 \end{bmatrix} \tag{2.4}$$

was uplinked on January 23^{rd} 2014.

Figure 2.2 shows the result of this calibration for the mentioned data recording. In the figure on the left the magnetic field strength is shown over time. Shown in red is the field strength as measured by the uncalibrated magnetometers, in blue the measurements after the correct calibration is applied and in green the magnetic field strength of the IGRF-11 model. It is obvious that the uncalibrated field strength not only varies due to the orbital movement (slow variation) but oscillates according to the rotational movement of the satellite. This component vanishes when the calibration is applied to the raw data, as can be seen in the blue graph.

Shown in Figure 2.2b is the distribution of the deviation of the magnetic field strength from the IGRF-11 reference field for all data recordings until March 4^{th} (more than 52.000 data points). Again, shown in red is the uncalibrated raw data and in blue the data after applying the computed calibration based on the data from December 19^{th}. It is visible that the calibrated measurements form a narrow distribution with the center almost at zero µT deviation while the raw data shows a wide distribution with an offset of 4.5 µT.

After calibration the magnetic field measurements are accurate to 1.8 µT (99% confidence) with respect to the reference magnetic field. Figure 2.3 shows the magnetic field as measured on board of UWE-3 and plotted on the instantaneous sub-satellite point. This magnetic field data can be interpolated to generate a map as shown in Figure 2.3b where the data from UWE-3 is compared to the International Geomagnetic Reference Field which is shown as contours.

The calibration was uplinked on January 23rd 2014 and is still found to be valid with minor adjustments made accounting for more data available to the calibration algorithm.

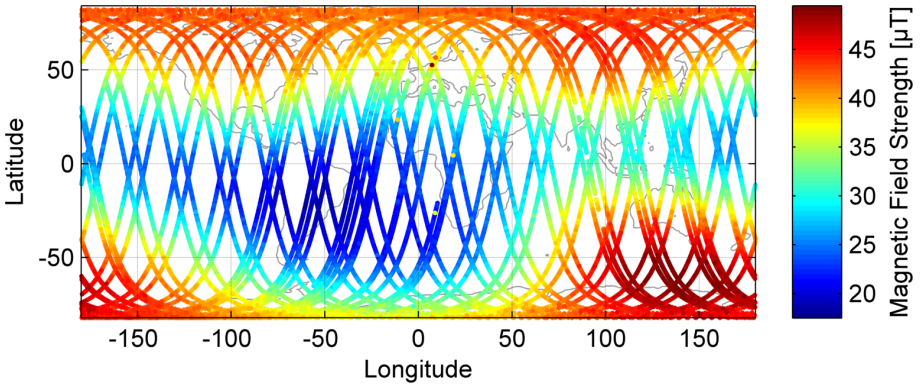

(a) Sub-satellite point plot.

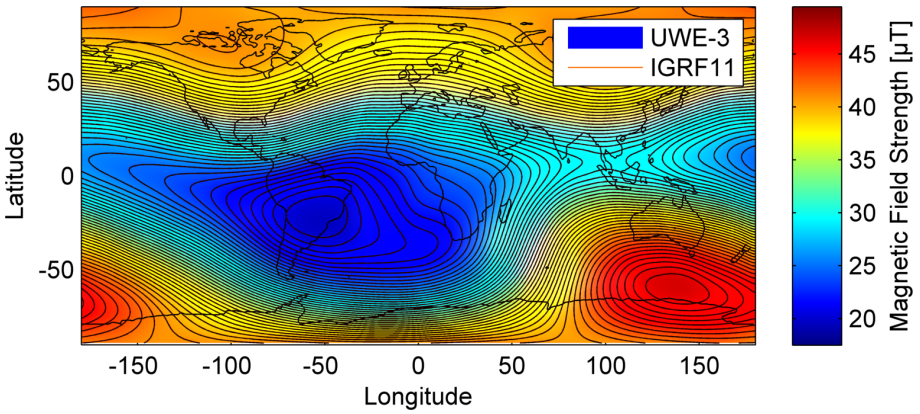

(b) Interpolation of measured data in comparison with the International Geomagnetic Reference Field.

Figure 2.3: Magnetic field strength as measured by UWE-3 and predicted by the IGRF model.

2.1.3 In-Orbit Sun-Sensor Calibration

The sun-sensors do not undergo major changes during launch and carry no offset. During operations of UWE-3 their behavior was found as expected and anticipated during ground-

testing. Therefore, their pre-launch calibration is still valid and only minor inaccuracies can be observed.

This is shown in Figure 2.4 where all six sun-sensor measurements are shown in body frame resulting in a consistent sun-vector even under rotation and while different sun-sensors identify the sun. The sun-sensors have a field of view (FOV) of approximately 150 ° which allows at least two sensors to measure the Sun direction at all times. It also can be seen that the -X sun-sensor produces only few valid measurements which did not change over the lifetime of UWE-3.

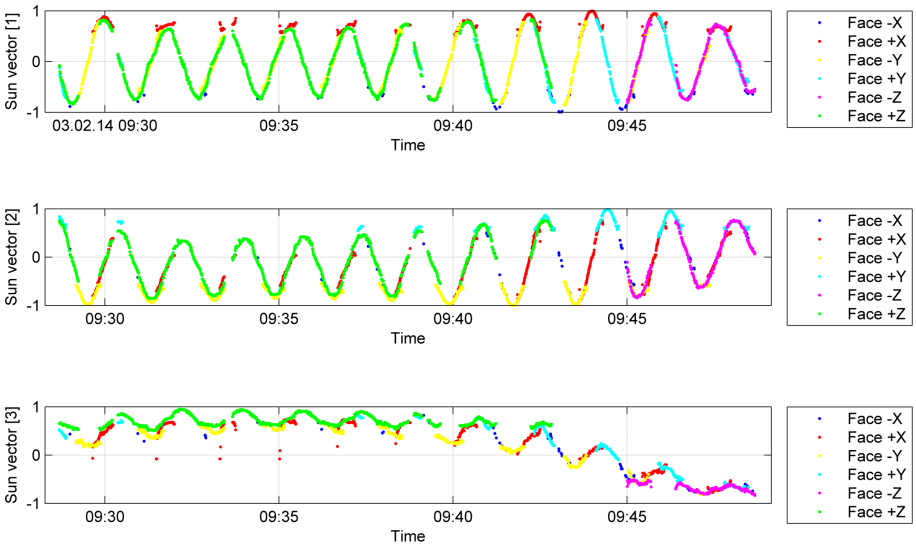

Figure 2.4: Sun vector in body frame measured by all six sun-sensors.

The filtering for the Sun intensity is shown in Figure 2.5, where the individual intensity measurements are presented. Also plotted (as red line) is the on-board computed intensity threshold which is an adaptive mechanism as can be seen when the satellite enters eclipse at 12:15h. The algorithm decreases the threshold until a fixed minimum is reached. When exiting the eclipse, the threshold is increased again immediately. This algorithm was implemented in order to avoid wrong configurations of an intensity threshold and delivered valid threshold estimates throughout the mission. Scholz et al. (2010) describe problems due to a wrong intensity threshold in the Compass-1 mission which rendered the attitude determination system of the CubeSat unable to estimate its 3-axis orientation. Such an issue could be avoided using the adaptive algorithm which is even more important due to the fact that on-ground tests with the sun-sensors do not obtain the same thresholds as in space.

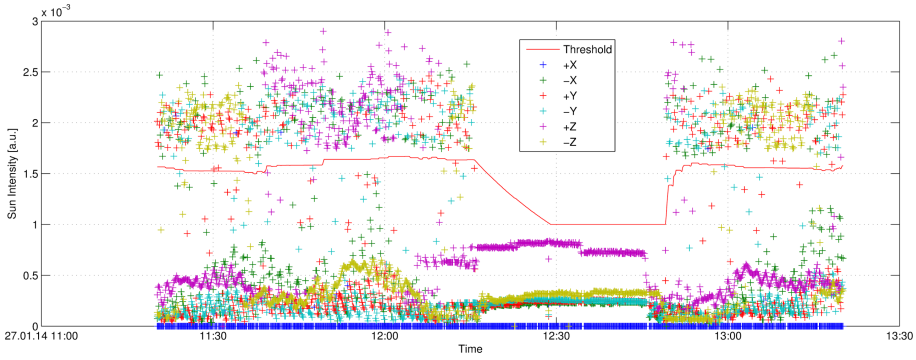

Figure 2.5: Intensity measured by the six sun-sensors over one orbit. Shown in red is the adaptive threshold which helps to discriminate between the Sun and other bright objects in the FOV of the sensors.

2.1.4 In-Orbit Gyroscope Calibration

The in-orbit calibration of the rate gyroscopes is based on the previous calibration of the magnetic field sensors and makes use of the fact that the orbital variation of the magnetic field vector is much smaller than the change due to tumbling of the satellite.

During launch of the satellite especially offsets of the MEMS gyroscopes can change due to the large mechanic loads experienced. Furthermore, minor changes in their mounting matrix may occur due to those loads such that an in-orbit calibration helps to increase the attitude determination accuracy.

The UWE-3 gyroscopes were calibrated prior to launch and the first sensor fusion experiments showed no significant deviation from this calibration. Only in October 2014 a dedicated calibration analysis was carried out that revealed indeed that the laboratory calibration was still valid.

The gyroscopes have a mounting matrix

$$M_{mount} = \begin{bmatrix} -1 & 0 & 0 \\ 0 & -1 & 0 \\ 0 & 0 & -1 \end{bmatrix} \tag{2.5}$$

and their offset was internally adjusted to zero before launch.

The calibration procedure is inspired by the work of Inamori and Nakasuka (2012) and makes use of the previously calibrated magnetometers. The idea is to derive the satellite's angular rate with the assumption that changes of the measured magnetic field are solely due to a rotation of the satellite. The change due to the satellite's orbital movement happens on a different time scale and can thus be neglected.

Therefore, any change of the body magnetic field vector $\mathbf{B}^b$ is to be described by a

rotation given by

$$\dot{\mathbf{B}}^b = \underbrace{\dot{\mathbf{B}}^i}_{\approx \mathbf{0}} + \tilde{\omega} \times \mathbf{B}^b \approx \tilde{\omega} \times \mathbf{B}^b, \tag{2.6}$$

where

$$\tilde{\omega} = C_{gyro}\,(\omega - \omega_0) \tag{2.7}$$

with $\tilde{\omega}$ being the calibrated angular rate, ω the measured raw angular rate, and C_{gyro} and ω_0 are the calibration matrix and offset correction.

Therefore, an error function can be found which in turn is minimized by an global optimization program to find C_{gyro} and ω_0. The error function is given by

$$E = \frac{1}{N}\sum_{i}^{N}\left(\dot{\mathbf{B}}^b + C_{gyro}\,(\omega - \omega_0) \times \mathbf{B}^b\right)^2. \tag{2.8}$$

The time derivative of the measured magnetic field is found numerically and care must be taken in order to interpolate correctly between the uncorrelated measurements of $\mathbf{B}^b$ and ω.

The result of this calibration procedure is shown in Figure 2.6 where the raw data, the pre-flight calibration, and the calibration through optimization is shown. The raw data clearly has the opposite sign due to the gyroscopes' mounting matrix. The pre-flight and in-orbit calibrated signals are almost indistinguishable due to their numerical similarity. The offset and calibration matrix found through this analysis are

$$\omega_0 = \begin{bmatrix} -0.9079 \\ 0.7936 \\ 0.8474 \end{bmatrix} \cdot 10^{-3}\mathrm{rad/s} \tag{2.9}$$

and

$$C_{gyro} = \begin{bmatrix} -0.9789 & 0.0600 & -0.0076 \\ -0.0220 & -1.0425 & -0.0022 \\ -0.0255 & 0.0044 & -0.9189 \end{bmatrix}. \tag{2.10}$$

It is easily visible that the calibration matrix resembles the initial mounting matrix from Eq. (2.5) to a high extent. The numerical offset found for the gyroscopes also is in an insignificant range such that only a minor increase in the attitude determination performance was expected due to the calibration.

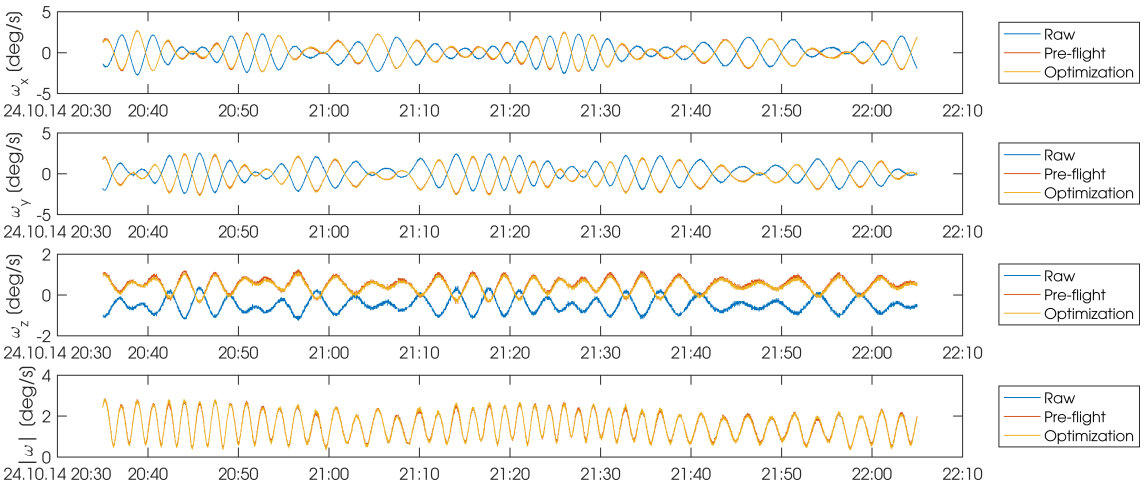

Figure 2.6: Gyroscope measurements before and after calibration.

2.2 Attitude Determination Performance Analysis

Miniature satellites only carry the bare essentials due to their power, size, and mass restrictions. Satellites that do not require high-precision attitude control avoid the integration of star-trackers and, if there is no additional optical payload, these satellites lack an external reference to their traditional attitude determination sensor suite. Especially CubeSats with a mission related to communication services, biological experiments, or technology demonstrations face the need for a self contained attitude determination verification.

The UWE-3 satellite does not carry additional sensors that could provide absolute pointing accuracy complementing its magnetometers and sun-sensors. Therefore, a procedure has been implemented to verify the correct functioning of the attitude determination system and assess its accuracy without the need for an external reference.

The UWE-3 satellite's attitude determination accuracy was estimated before launch of the satellite in the University's laboratories to be in the order between 2 ° and 7 ° depending on the rotation rate of the satellite (Bangert, 2012). This performance was measured with the help of an external optical encoder that detected the precise orientation of the satellite on its test bench. However, UWE-3 misses such an external and independent sensor type for in-orbit attitude determination performance estimation. Other CubeSats have countered this analysis with the help of optical instruments whose images give information about the satellite's current pointing and have compared it to the ADCS's current attitude estimation (e.g. Slavinskis et al. (2016)).

Hence, a consistency analysis was selected as the best possible method. This analysis compares the raw sensor data recorded on board of the satellite against the Kalman filter's

actual attitude estimation. This approach was also tested in simulation from which further insights in the absolute attitude estimation accuracy become available.

In the following sections, first the analysis procedure is formulated and its extent of validity is stated. Then, the in-orbit data is presented together with its concluding attitude estimation accuracy. Chapter 2.2.3 shows the application of the procedure onto a simulated attitude estimation and concludes with an absolute accuracy estimation.

2.2.1 Attitude Estimation Consistency Analysis

In order to verify the correct functioning of the attitude determination system a consistency analysis was carried out. This analysis compares the raw sensor measurements $\tilde{\mathbf{X}}$ transformed into the inertial reference frame according to the satellite's attitude knowledge $\tilde{q}$ with the model reference values $\hat{\mathbf{X}}$ in inertial frame. Any measured reference vector $\tilde{\mathbf{X}}$ is subject to noise n_X and offsets or biases $\mathbf{b}_X$ either due to the satellite's environment or for instance a slightly imprecise mounting. Therefore

$$\tilde{\mathbf{B}} = \hat{q} * \hat{\mathbf{B}} + \mathbf{b}_B + n_B, \tag{2.11}$$

$$\tilde{\mathbf{S}} = \hat{q} * \hat{\mathbf{S}} + \mathbf{b}_S + n_S, \tag{2.12}$$

where $\tilde{\mathbf{B}}$ is the measured magnetic field vector in body coordinates and $\tilde{\mathbf{S}}$ the measured sun-vector in body coordinates. $\hat{q}$ denotes the satellite's true orientation with respect to the inertial reference frame and $\hat{q}*$ then denotes the transformation from the inertial reference frame to the satellite's body frame.

The satellite's estimated attitude $\tilde{q}$ transforming reference vectors from inertial into the body coordinate frame can be written as

$$\tilde{q} = \hat{q} * q_e, \tag{2.13}$$

where $\hat{q}$ is the true satellite orientation and q_e is an erroneous rotation which is equivalent to the overall attitude estimation accuracy.

When comparing the measured sensor data to the expected models based on the satellite's own attitude estimation we determine the angles β and γ such that

$$\beta = \angle(\tilde{q}^{-1} * \tilde{\mathbf{B}}, \hat{\mathbf{B}}), \tag{2.14}$$

$$\gamma = \angle(\tilde{q}^{-1} * \tilde{\mathbf{S}}, \hat{\mathbf{S}}), \tag{2.15}$$

$\tilde{q}^{-1}*$ is the transformation from body into the inertial frame based on the satellite's

estimated attitude. β therefore denotes the angle between the expected magnetic field vector and the measured magnetic field vector transformed into the inertial reference frame, and γ the same for the sun-vector. In general, the expression for these two angles can be written as

$$\cos(\alpha) = \frac{\left(\tilde{q}^{-1} * \tilde{\mathbf{X}}\right) \cdot \hat{\mathbf{X}}}{\left|\tilde{q}^{-1} * \tilde{\mathbf{X}}\right| \left|\hat{\mathbf{X}}\right|}, \tag{2.16}$$

where α is either β for $\mathbf{X} = \mathbf{B}$ and γ for $\mathbf{X} = \mathbf{S}$. Rewriting Eq. (2.16) with Eq. (2.12) and Eq. (2.13), and denoting $\mathbf{x}$ as normalized $\mathbf{X}$ gives

$$\begin{aligned}
\cos(\alpha) &= \left(\tilde{q}^{-1} * (\hat{q} * \hat{\mathbf{x}} + \mathbf{b}_x + n_x)\right) \cdot \hat{\mathbf{x}} && (2.17)\\
&= \left((\hat{q} * q_e)^{-1} * \hat{q} * \hat{\mathbf{x}}\right) \cdot \hat{\mathbf{x}} + \left((\hat{q} * q_e)^{-1} * \mathbf{b}_x\right) \cdot \hat{\mathbf{x}} + \left((\hat{q} * q_e)^{-1} * n_x\right) \cdot \hat{\mathbf{x}} && (2.18)\\
&= \left(q_e^{-1} * \hat{q}^{-1} * \hat{q} * \hat{\mathbf{x}}\right) \cdot \hat{\mathbf{x}} + \left((\hat{q} * q_e)^{-1} * \mathbf{b}_x\right) \cdot \hat{\mathbf{x}} + \left((\hat{q} * q_e)^{-1} * n_x\right) \cdot \hat{\mathbf{x}} && (2.19)\\
&= \cos\left(\angle\left(q_e^{-1}\right)\right) + \cos\left(\angle\left((\hat{q} * q_e)^{-1} * \mathbf{b}_x, \hat{\mathbf{x}}\right)\right) + \cos\left(\angle\left((\hat{q} * q_e)^{-1} * n_x, \hat{\mathbf{x}}\right)\right) && (2.20)\\
&= \cos(\alpha_e) + \cos(\alpha_b) + \cos(\alpha_n). && (2.21)
\end{aligned}$$

This means, that α has three components that are inherent to this analysis. The first one, $\alpha_e = \angle(q_e^{-1})$, is the absolute attitude determination accuracy which is the actual value that we are interested in. The second term $\alpha_b = \angle((\hat{q} * q_e)^{-1} * \mathbf{b}_x, \hat{\mathbf{x}})$ is due to wrong calibration of the sensors and couples with the attitude determination accuracy as well. The third term, $\alpha_n = \angle((\hat{q} * q_e)^{-1} * n_x, \hat{\mathbf{x}})$, is due to noise of the sensors and again couples with the attitude determination accuracy.

The sensor calibration minimizes the second term such that by measuring α this effect is not dominant, but the term due to the sensor noise cannot be eliminated. Therefore, the attitude determination accuracy estimation by consistency analysis will always find a worst case accuracy estimate and β and γ will be inherently different for the two sensor types due to their different noise characteristics. However, by knowing the noise levels of the used sensors, one can roughly estimate the contribution of the third term.

In the following section this analysis is performed with the in-orbit data of UWE-3 and in Chapter 2.2.3 the analysis is carried out on simulated data. There, the absolute pointing error q_e is known such that the findings can be compared to the ones from Chapter 2.2.2 in order to obtain an estimate for the absolute pointing error q_e of the in-orbit data.

2.2.2 Attitude Estimation Accuracy of UWE-3

Having calibrated the magnetometers of UWE-3, the attitude determination was characterized again using data recorded on January 27$^{\text{th}}$ 2014. The recorded data consisted of magnetic field measurements, sun-vector measurements, and the on-board computed quaternions.

The measurements made in body coordinates have been transformed into ECI coordinates using the quaternions and their angular displacement towards the according reference vector computed as given in Eq. (2.16). For the data recording conducted on January 27$^{\text{th}}$ 2014 the transformed measurements are shown in Figure 2.7 and Figure 2.8 for the magnetic field vector and for the sun-vector, respectively. The angular error is also shown, both as time series and as distribution.

β was found to have a median of 1.82 ° and does not show systematic behavior in the time series. The sun-vector is only shown where no eclipse was detected by the on-board algorithms and γ can be computed on these intervals to have a median of 5.28 °.

During the eclipse the attitude determination is purely based on the magnetic field measurements and attitude predictions based on the gyroscopes and is therefore missing information about one rotational axis (about the magnetic field direction) and is allowed to drift about this axis. However, after exiting the eclipse the satellite acquires valid sun-sensor data again. The first few measurements show a slightly higher mismatch until the necessary adjustments to the estimated attitude are made by the Kalman filter. Just after exiting the eclipse at about 12:50 UTC the error angle reaches values of up to 50 °, which results in a 99% quantile of 23.98 °.

As shown in Eq. (2.21) these accuracies give a worst case estimate of the attitude determination since they still include the sensor noise on top of the attitude estimation noise. This sensor noise was estimated before launch which can be found in Bangert (2012) and Reichel et al. (2013). The precision of the magnetometers has been proven to be better than 3 ° and the sun-sensors have a resolution of 2.7 ° with an accuracy of 5 °. Therefore, the mean angular error of both sensors lie within their respective noise cone, from which can be concluded that the attitude estimation α_e also lies within these limits.

It should also be noted that the deviation between the on average measured sun-vector in ECI frame and the reference vector is only 0.2° which means that there is only a negligible systematic attitude error bias present through α_b.

The attitude determination accuracy was evaluated several times over the lifetime of the satellite. An overview of the results is presented in Table 2.1 and shown in Figure 2.9.

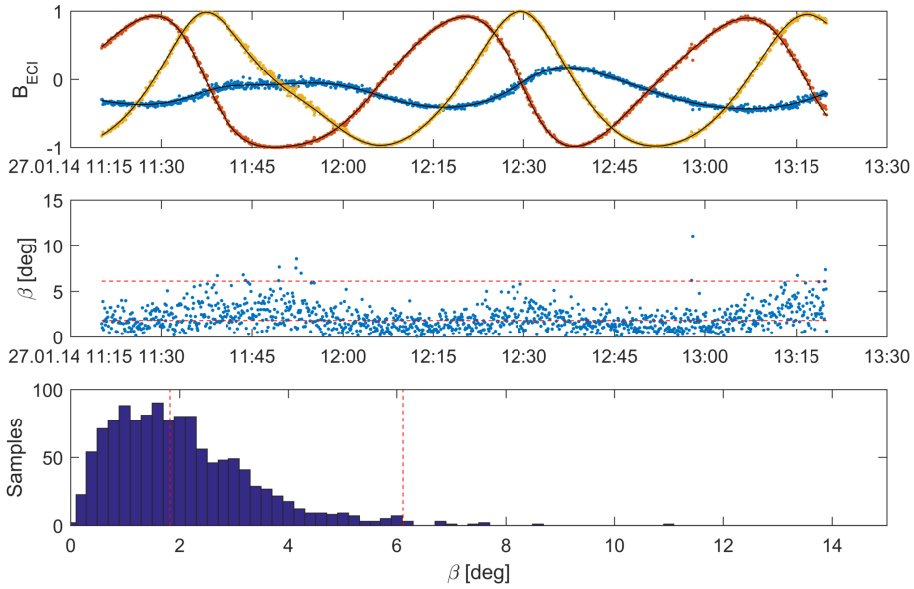

Figure 2.7: Magnetic field measurements after calibration transformed to ECI and compared with the IGRF reference model. The angular error as computed according to Eq. (2.21) has a median of 1.82 ° and a 99% quantile of 6.11 °, as indicated in red dashed lines.

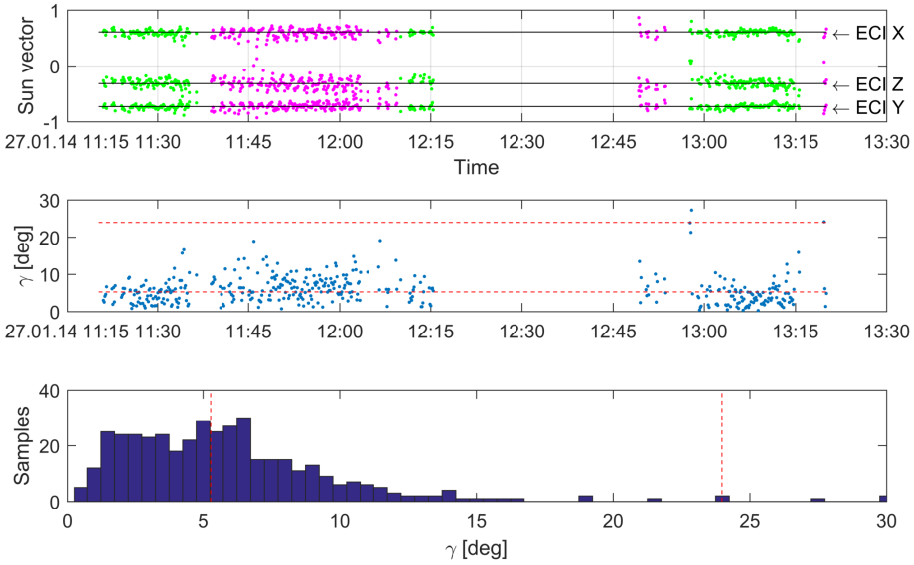

Figure 2.8: Sun vector measurements of all 6 Sun sensors transformed to ECI coordinates and compared with expected Sun vector. The mean of the angular error is found to be 5.28 ° and 99% of all measurements are within 23.98 °.

The mean values found for β and γ are

$$\bar{\beta} = 2.04\,^\circ \tag{2.22}$$

and

$$\bar{\gamma} = 6.00\,^\circ. \tag{2.23}$$

Over almost three years of operation, the attitude determination accuracy did not change significantly, until the beginning of 2016 when some of the sun-sensors failed. The last two measured attitude accuracies in 2016 have already been subject to this issue and especially the last measurement from 04.04.2016 shows that when the failed sensors have been included into the attitude determination process it could heavily been disturbed. In May 2016, only two out of six sun-sensors were functioning correctly, rendering attitude determination impossible under certain configurations.

This analysis concludes that the satellite's in-orbit attitude determination accuracy was found to be consistent with the pre-launch laboratory tests which stated an accuracy in the range between 2 ° and 7 ° (Bangert, 2012). In the following sections, simulations are presented that give further insight in the relation between β and γ and the absolute attitude determination error α_e.

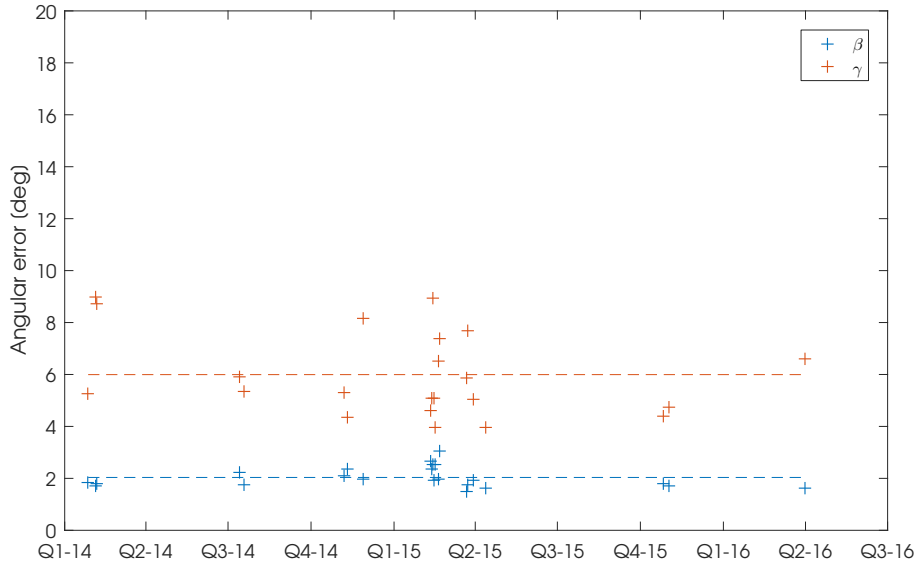

Figure 2.9: Attitude accuracy analysis over the lifetime of the UWE-3 satellite as described in Chapter 2.2.1. The mean values for β and γ are 2.04 ° and 6.00 °, respectively, and are shown as dashed lines.

Date	median β	median γ
27.01.2014	1.82 °	5.28 °
04.02.2014	1.73 °	8.97 °
05.02.2014	1.81 °	8.73 °
14.07.2014	2.24 °	5.92 °
19.07.2014	1.74 °	5.36 °
07.11.2014	2.10 °	5.29 °
10.11.2014	2.37 °	4.34 °
28.11.2014	1.98 °	8.14 °
11.02.2015	2.65 °	4.61 °
12.02.2015	2.36 °	5.07 °
13.02.2015	2.54 °	8.96 °
14.02.2015	1.91 °	5.09 °
15.02.2015	2.53 °	3.96 °
19.02.2015	1.96 °	6.51 °
20.02.2015	3.05 °	7.40 °
23.03.2015	1.51 °	5.85 °
24.03.2015	1.76 °	7.67 °
30.03.2015	1.92 °	5.03 °
13.04.2015	1.64 °	3.98 °
27.10.2015	1.80 °	4.38 °
02.11.2015	1.73 °	4.75 °
01.04.2016	1.62 °	6.60 °
04.04.2016	1.54 °	25.10 °

Table 2.1: Angular errors β and γ for several attitude determination accuracy evaluations.

2.2.3 Simulation Results and Absolute Attitude Determination Accuracy

The consistency analysis of the in-orbit data can only produce estimates of the true attitude determination accuracy which is only accessible when there is a third uncorrelated sensor measurement available, such as a payload camera or a star tracker. However, having established a precise and reliable simulation framework, it is possible to estimate the true determination accuracy in conjunction with the consistency of the two sensors. In the simulation, both the true attitude $\hat{q}$ and the satellite's estimated attitude $\tilde{q}$ are known as well as the sensor readings with their characteristic noise and discretization.

In order to obtain an absolute attitude determination accuracy the simulation was run over two orbits for different starting days in the year 2014. In order to statistically rule out any correlation with the Earth's orbital position and orientation, i.e. time of the day, which

both slightly influence the angle between the Earth's magnetic field and the Sun direction, the starting time was randomly distributed over the full day and one simulation was carried out for each day of the year. The initial conditions with respect to initial orientation and initial angular rate were randomly chosen for each day. The noise characteristics for each sensor is given in Table 2.2.

Sensor	3σ noise	discretization
Magnetometers	1.8 µT	0.01 µT
Sun-sensors	6 °	2.5 °
Gyroscopes	0.05 °/s	0.0725 °/s

Table 2.2: Sensor noise and discretization.

The simulation results are shown in Figure 2.10 and Figure 2.11 where the medians of β, γ, and α_e are shown. The data obtained with the simulation clearly matches the in-orbit data in terms of β and γ. The mean values found are

$$\bar{\beta}_{sim} = 2.16\,^\circ \tag{2.24}$$

and

$$\bar{\gamma}_{sim} = 5.49\,^\circ, \tag{2.25}$$

When comparing these results with the in-orbit measurements given in Table 2.1 the simulation can give valuable insight into the true determination accuracy α_e. The mean angular error of the attitude estimation simulation is

$$\bar{\alpha}_{e,sim} = 2.61\,^\circ \tag{2.26}$$

which is in well accordance with the laboratory pre-flight accuracy assessment. Therefore, it can be concluded that the true in-orbit attitude determination accuracy indeed is also in the order of 2.61 °.

2.3 Summary

A procedure to calibrate a typical miniature satellite attitude sensor suite in-orbit without external reference has been developed. The procedure is applicable to any satellite equipped with magnetometers, sun-sensors, and gyroscopes, and takes into account non-orthogonality of the sensors' axes. This is in particular useful for attitude determination systems equipped with single-axis sensors. The only requirement to apply the procedure is

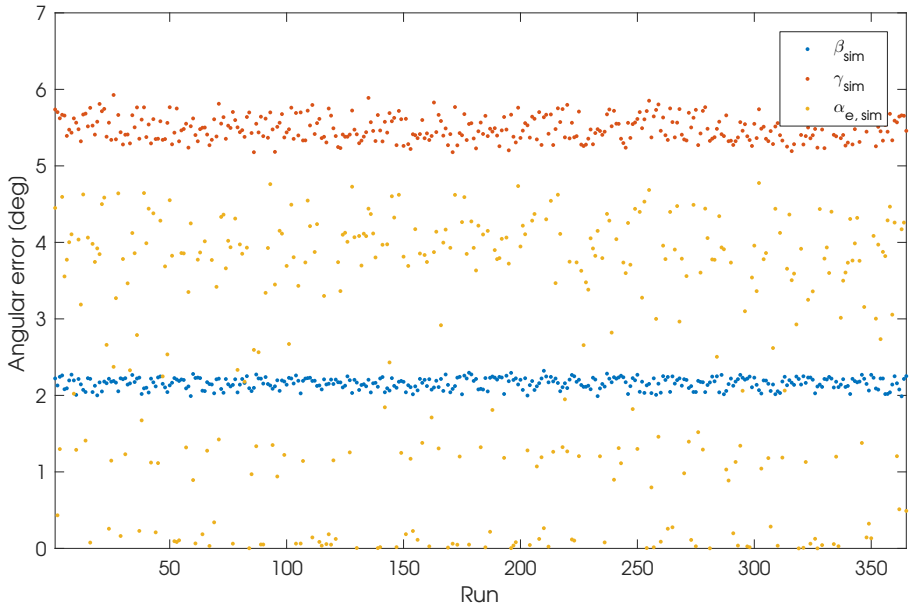

Figure 2.10: Simulation result for attitude determination simulations for one year with each run randomly initiated.

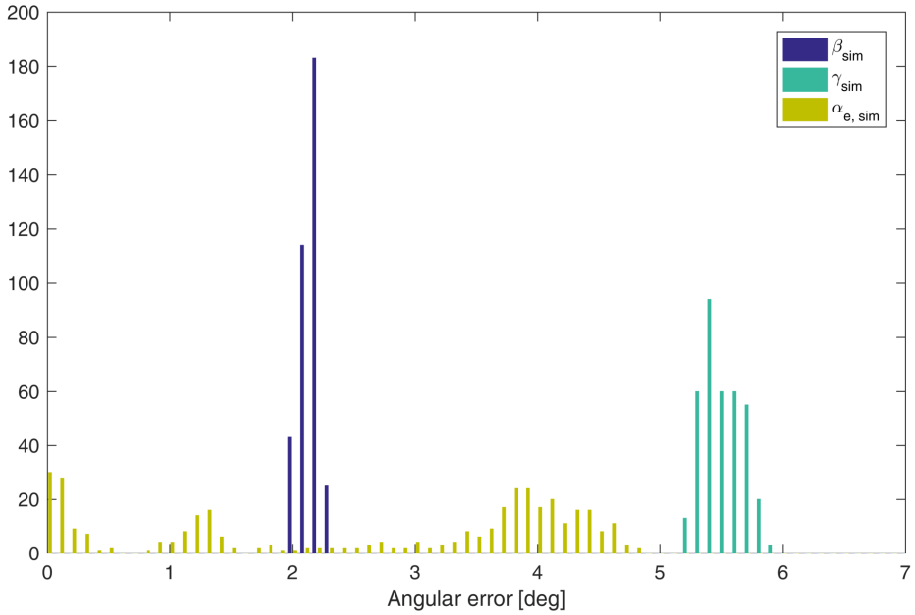

Figure 2.11: Histogram of results of the attitude determination simulations for one year with each run randomly initiated.

that the satellite must not be stabilized in the inertial or orbital frame. It is applicable to any tumbling satellite which usually is the case for miniature satellites after in-orbit insertion.

The procedure was applied to in-orbit data from UWE-3 and a consistent attitude sensor calibration was obtained. Major changes in the magnetometer offsets compared to calibration prior to launch show the susceptibility of highly integrated miniature satellites to even minor changes in their mechanic configuration, and therefore the importance of in-orbit calibration procedures.

Furthermore, an attitude determination verification algorithm has been implemented that does not require an external reference sensor. It evaluates the consistency between raw sensor measurements and the fused attitude estimation solution. Using in-orbit data from the UWE-3 satellite and by comparing the consistency analysis result with the result of a high-fidelity simulation it could be shown that the analysis provides a reliable estimate of the satellite's attitude determination accuracy. For UWE-3 a typical attitude estimation accuracy in the order of 2.6 ° was achieved.

3

Attitude Disturbance Estimation

Attitude disturbances are always of concern for satellite developers. In the case of miniature satellites the correct assessment of disturbance torques is especially important due to their limited control capabilities. The latter are inherently constricted by the satellite's size, power, and mass restrictions, such that unanticipated disturbances can easily exceed the actuator envelopes.

Miniature satellites have the advantage of reduced disturbances related to their spacial extension, such as the solar pressure torque or gravity gradients. Also magnetic disturbances due to large current loops are rare because of, both, the little power generation and consumption of these satellites, and less room for unfortunate routing of loops. However, static magnetic moments can occur independent of the satellite's size and pose the highest risk for large disturbance torques. At the same time residual magnetic moments are very difficult to avoid due to limitations of available and affordable materials, and inherent stray magnetic fields in electric components.

Measuring the residual magnetic dipole moment of a satellite in orbit can increase the attitude pointing accuracy and reveal design flaws to be avoided in future satellites. Therefore, an algorithm to determine the disturbance due to a residual magnetic dipole moment has been developed and applied to three different miniature satellites in orbit. The results show the importance of this analysis in order to optimize attitude control. It is shown that in some cases a critical disturbance strength is reached which highly corrupts the satellite's attitude control system. For the UWE-3 satellite it was possible to perform a long term analysis of the residual dipole moment that shows that it is indeed constant over many years. This concludes that a static magnetization is the cause for the disturbance and a further analysis was able to reveal the most probable cause for it.

The procedure can also be used to determine the exact control moment of a magnetorquer, as shown for the UWE-3 satellite. This may be used to further increase the satellite's

attitude control efficiency.

While the primary concept is based on post-processing of magnetic field sensor and rate gyroscope data also an approach to determine the static residual magnetic dipole on board of the satellite has been implemented. This estimator is simple enough to be implemented on the computational platforms of CubeSats and simulations show that it is able to characterize this disturbance autonomously.

3.1 Attitude Disturbance Torques

There are different external torques acting on the satellite which will be shortly assessed for their worst-case magnitude in the case of a 1U CubeSat in Low Earth Orbit. It can quickly be seen that for this class of satellites only the disturbance torque due to an interaction of an inherent magnetic moment of the satellite with the Earth's magnetic field is of relevance. However, this torque may easily reach a critical magnitude that can put the complete mission's success at risk.

3.1.1 Gravity-Gradient Torque

A gravitational field declines proportional to $1/r^2$ with distance r from its origin and therefore elongated bodies experience slight differences in their attracting forces $\mathbf{F}_i$ on different parts of their body i at distance from the Earth's center $\mathbf{r}_i$ (Wertz, 1978):

$$\mathbf{F}_i = -\frac{GM\mathbf{r}_i m_i}{\left|\mathbf{r}_i^3\right|}, \tag{3.1}$$

with GM being the Earth's gravity constant.

This results in a torque aligning the satellite's minimal principal axis with the local vertical. For a spacecraft at distance R from the Earth's center with principal axes I_1 and I_2 and a maximal deviation of the principal axis from the local vertical θ the gravity gradient torque can be estimated as (Wertz and Larson, 1999)

$$T_{gg} = \frac{3\mu}{2R^3}|I_1 - I_2|\sin(2\theta). \tag{3.2}$$

As can be seen the torque vanishes for symmetric spacecrafts where $I_1 \approx I_2$ which is a valid approximation for 1U CubeSats. With a worst case assumption of $\theta = 45°$ and a maximal difference in principal axes of approximately $1 \cdot 10^{-4}\,\mathrm{kg\,m^2}$ one can derive a

maximum gravity gradient torque acting on the satellite in a 700 km orbit of about

$$T_{gg} \approx 0.17 \cdot 10^{-9} \mathrm{N\,m}. \tag{3.3}$$

3.1.2 Solar Radiation Torque

The solar radiation torque is induced by photons impacting on and being reflected off of certain parts of a spacecraft, such as large solar arrays. Since different parts of spacecrafts in general have different absorption and reflection coefficients the radiation pressure does not homogeneously act on the complete satellite. For instance, solar arrays usually are classified as absorbers while radiators and large parts of the spacecraft body are reflective. Therefore, a torque is generated by a differential radiation force $\mathrm{d}\mathbf{f}_{sp}$ acting on elemental surface areas $\mathrm{d}A$ (Wertz, 1978):

$$\mathrm{d}\mathbf{f}_{sp} = -\frac{F_s}{c} \int \left[(1 - C_s)\,\hat{\mathbf{S}} + 2\left(C_s \cos(\theta) + \frac{1}{3} C_d \right) \hat{\mathbf{N}} \right] \cos(\theta) \mathrm{d}A, \tag{3.4}$$

with the solar constant F_s, speed of light c, the unit vector from the spacecraft to the Sun $\hat{\mathbf{S}}$, the area's normal $\hat{\mathbf{N}}$, and $\theta = \angle(\hat{\mathbf{S}}, \hat{\mathbf{N}})$. The coefficients C_s and C_d describe the area's specular reflection and diffuse reflection, respectively, such that the absorption coefficient is given by $C_a = 1 - C_s - C_d$.

The solar radiation torque $\mathbf{T}_{sp}$ then is given by the integration over all elementary areas at their respective position $\mathbf{R}$ from the spacecraft's center of mass:

$$\mathbf{T}_{sp} = \int \mathbf{R} \times \mathrm{d}\mathbf{f}_{sp} \tag{3.5}$$

Expressed in terms of the center of solar pressure c_{ps}, the center of gravity cg, and the surface area A of the spacecraft the magnitude of the solar radiation torque $T_{sp,max}$ can be written as

$$T_{sp} = \frac{F_s}{c} A\,(1 + q) \cos(i)\,(c_{ps} - cg)\,, \tag{3.6}$$

where q is the reflectance factor (between 0 and 1) and i is the angle of incidence of the Sun. For a 1U CubeSat this torque is negligible as the difference in center of solar pressure and the center of gravity, as well as the overall area of the satellite are diminutive, such that a worst case estimate is obtained by

$$T_{sp,max} = \frac{1367\,\mathrm{W/m^2}}{3 \cdot 10^8\,\mathrm{m/s}} (0.1\,\mathrm{m})^2 \cdot 2 \cdot 0.05\,\mathrm{m} \approx 5 \cdot 10^{-9}\,\mathrm{N\,m} \tag{3.7}$$

3.1.3 Aerodynamic Torque

The residual atmosphere in low Earth orbits excites an aerodynamic torque on satellites due to a difference in the satellite's center of mass and the actual center of pressure. On an elementary area dA, similar to the solar radiation force, a differential aerodynamic force $\mathrm{d}\mathbf{f}_{aero}$ can be computed by

$$\mathrm{d}\mathbf{f}_{aero} = -\frac{1}{2} C_d \rho V^2 \left(\hat{\mathbf{N}} \cdot \hat{\mathbf{V}}\right) \hat{\mathbf{V}} \mathrm{d}A, \tag{3.8}$$

with C_d being the drag coefficient, ρ being the atmospheric density, $\mathbf{V}$ the actual velocity vector, and $\hat{\mathbf{N}}$ the surface normal. Again, the total resulting torque is given by integration over all elementary areas at position $\mathbf{R}$:

$$\mathbf{T}_{aero} = \int \mathbf{R} \times \mathrm{d}\mathbf{f}_{aero} \tag{3.9}$$

Expressed in terms of the center of aerodynamic pressure c_{pa} the magnitude of the aerodynamic torque is given by

$$T_{aero} = \frac{1}{2} C_d A \rho V^2 \left(c_{pa} - cg\right). \tag{3.10}$$

As a worst case estimate C_d can be assumed to be 2.5 and the difference in the center of pressure and center of gravity being 0.05 m. The velocity of a satellite in an orbit of about 700 km altitude is approximately $V = 7.5\,\mathrm{km/s}$ while the residual atmospheric density is in the order of $\rho \approx 1 \cdot 10^{-13}\,\mathrm{kg/m^3}$. Therefore, a worst case estimate of the atmospheric torque acting on a 1U CubeSat is

$$T_{aero,max} \approx \frac{1}{2} \cdot 2.5 \cdot (0.1\,\mathrm{m})^2 \cdot 1 \cdot 10^{-13}\,\mathrm{kg/m^3} \cdot (7.5\,\mathrm{km/s})^2 \cdot 0.05\,\mathrm{m} \approx 3.5 \cdot 10^{-9}\,\mathrm{N\,m}. \tag{3.11}$$

3.1.4 Magnetic Disturbance Torque

A satellite carrying a magnetic moment μ will experience a torque due to the interaction between its residual magnetic field and the Earth's magnetic field $\mathbf{B}$. The torque created by this interaction is given by

$$\mathbf{T}_{mag} = \mu \times \mathbf{B}. \tag{3.12}$$

Magnetic moments can occur due to magnetized materials or current loops. In the latter case, the magnetic moment is created by a current I enclosing an area A with normal vector

$\hat{\mathbf{N}}$ such that

$$\mu_{loop} = IA\hat{\mathbf{N}} \tag{3.13}$$

In order to assess the importance of this disturbance it is assumed that the complete power generated by the solar cells is routed in a single loop of maximal dimensions towards the satellite's batteries. Thus, $A = (0.1\,\mathrm{m})^2$ and $I \approx 2 \cdot 500\,\mathrm{mA} = 1\,\mathrm{A}$ for 2 solar cells being illuminated on one face of the CubeSat. Therefore, the worst case magnetic moment due to current loops is in the order of $\mu_{loop} \approx 10\,\mathrm{mA\,m^2}$, resulting in a torque in the order of

$$T_{mag,curr} \approx 10\,\mathrm{mA\,m^2} \cdot 40\,\mu\mathrm{T} = 0.4 \cdot 10^{-6}\,\mathrm{N\,m}. \tag{3.14}$$

However, as will be shown later using in-orbit data from UWE-3 and other miniature satellites, this effect plays a minor role in the actual case of CubeSats. A much more important factor are materials carrying an intrinsic magnetic field that interacts with the surrounding Earth's magnetic field. Although usually care is taken to avoid any magnetic materials on board of satellites, there are many examples in the field of small satellites where the disturbance due to such a residual magnetic moment has been significant.

Individual satellite components ranging from ICs to structural components and antennas are likely to contribute more or less to the overall magnetic dipole. While modern ICs pose no actual threat in this respect due to their usually small dimensions and scattered placement within the satellite, larger components such as surface mounted coils, batteries, or large DC/DC converters can introduce minor magnetic moments.

Most significant contributions however usually come from extended structural components such as screws and distance holders, or elongated antennas. Depending on their size and level of (unintended) magnetization a residual dipole of several hundred $\mathrm{mA\,m^2}$ can result in a significant disturbance for the satellite's attitude control system.

Schalkowsky and Harris (1969) state that "by means of compensating magnets, achievement of residual moments in the range of 0.050 to 0.10 ampere-meter^2 ($\mathrm{A\,m^2}$) (...) is possible in small, magnetically clean spacecraft in the laboratory". However, a total residual magnetic dipole moment of $100\,\mathrm{mA\,m^2}$ already excites a torque of about

$$T_{mag,tot} \approx 100\,\mathrm{mA\,m^2} \cdot 40\,\mu\mathrm{T} = 4.0 \cdot 10^{-6}\,\mathrm{N\,m} \tag{3.15}$$

which is a significant disturbance for miniature satellites.

The magnetic disturbance torque is therefore the most important disturbance for miniature satellites. An overview over all disturbance torques and their order of magnitudes is given in Table 3.1.

Type	Typical disturbance
Static Magnetic	$4.0 \cdot 10^{-6}\,\mathrm{N\,m}$
Induced Magnetic	$0.4 \cdot 10^{-6}\,\mathrm{N\,m}$
Solar radiation	$5.0 \cdot 10^{-9}\,\mathrm{N\,m}$
Aerodynamic	$3.5 \cdot 10^{-9}\,\mathrm{N\,m}$
Gravity-Gradient	$1.7 \cdot 10^{-10}\,\mathrm{N\,m}$

Table 3.1: Typical contributions of the different disturbance torques on a 1U CubeSat in Low Earth Orbit.

3.2 Residual Magnetic Dipole Moment Estimation

The numeric estimation of the residual magnetic dipole moment is based on in-orbit recordings of the attitude determination system. In particular, it requires sampling of magnetic field and angular rate measurements. Identifying the influence of a magnetic dipole on the satellite's dynamics, an optimization algorithm can be set up that determines the magnetic dipole moment based on the combination of the recorded data.

The attitude dynamics of a rigid body follow the well known Euler equations expressed in body coordinates:

$$\mathbf{T}_{ext} = I\dot{\omega} + \omega \times (I\omega)\,, \tag{3.16}$$

with $\mathbf{T}_{ext}$ being the sum of all external torques and I being the moment of inertia tensor. ω is the angular rate vector of the satellite with respect to the inertial frame and expressed in body coordinates. As shown in chapter 3.1, the magnetic disturbance torque $\mathbf{T}_\mu(t)$ is by far the dominating external influence on the attitude dynamics of a miniature satellite. Therefore, Eq. (3.16) can be rewritten as

$$\mathbf{T}_\mu(t) = \mu(t) \times \mathbf{B}(t) = I\dot{\omega}(t) + \omega(t) \times (I\omega(t))\,, \tag{3.17}$$

where the explicit dependance of all quantities (except for the satellite's inertia I) on time t is shown. Since the numeric differentiation of a noisy sensor requires smoothing filters, care must be taken with respect to the desired signal frequency bandwidth. Therefore, an analytical approximation of the expected oscillation frequency of ω is performed as follows.

3.2.1 Frequency Estimation

The behavior of a magnetic dipole in an external magnetic field is similar to a 3D pendulum under gravitational influence. In order to estimate the expected oscillation frequency of ω the dynamics are simplified to the case of a projection onto the x-y-plane. The pendulum equation for the angle $\alpha(t)$ between the (constant) magnetic field $B(t) = B_0$ and the moving magnetic dipole $\mu(t)$ is given by

$$I\ddot{\alpha} - \mu \times B = I_0\ddot{\alpha} - \mu_0 \begin{bmatrix} \cos(\alpha) \\ \sin(\alpha) \end{bmatrix} \times \begin{bmatrix} B_0 \\ 0 \end{bmatrix} = I_0\ddot{\alpha} + \mu_0 B_0 \sin(\alpha) = 0. \tag{3.18}$$

Using the approximation for small angles $\sin(\alpha) \approx \alpha$ the second order differential equation

$$\ddot{\alpha} + \frac{\mu_0 B_0}{I_0}\alpha = 0 \tag{3.19}$$

with its well known solution

$$\alpha = Ae^{i\omega_\alpha t}, \tag{3.20}$$

and

$$\omega_\alpha = \sqrt{\frac{\mu_0 B_0}{I_0}}, \tag{3.21}$$

can be obtained, with ω_α being the angular frequency of α and also of $\dot{\alpha}$. Translating this into the case of the magnetic dipole moment behaving like a pendulum in the Earth's magnetic field, typical oscillation frequencies on each axis of the satellite's angular rate can be expected. The satellite experiences a mean magnetic field strength in the order of $B_0 \approx 30\,\mu T$ and has a mean moment of inertia about its axis of $I_0 \approx 0.0017\,\mathrm{kg\,m^2}$. A magnetic dipole of $\mu_0 \approx 0.05\,\mathrm{A\,m^2}$ would therefore result in an oscillation frequency

$$f_\alpha = \frac{\omega_\alpha}{2\pi} = \frac{\sqrt{\frac{\mu_0 B_0}{I_0}}}{2\pi} \approx \frac{\sqrt{\frac{0.05\,\mathrm{A\,m^2}\cdot 30\,\mu\mathrm{T}}{0.0017\,\mathrm{kg\,m^2}}}}{2\pi} = 0.0046\,\mathrm{Hz}. \tag{3.22}$$

Shown in Figure 3.1a and Figure 3.1b is the angular rate data of UWE-3 from an on-board recording from November 10$^{\text{th}}$ 2015 and the corresponding frequency analysis (by FFT), respectively. It can be seen that the oscillation frequency of each axis lies within a range between a minimal and maximal frequency. These are obtained by using the minimal and maximal measured magnetic field strength which influences the frequency as stated in Eq. (3.22). It can be seen that the angular rate oscillates with a frequency around 0.005 Hz as estimated in theory.

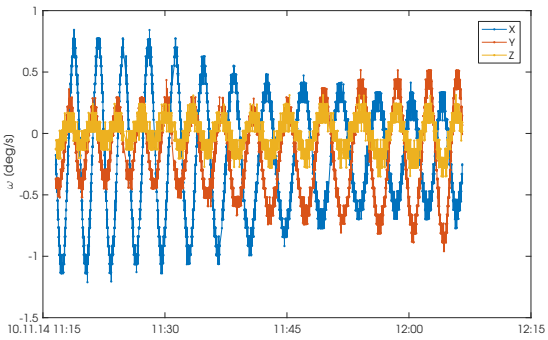

(a) The UWE-3 angular rates as measured on November 10th 2015.

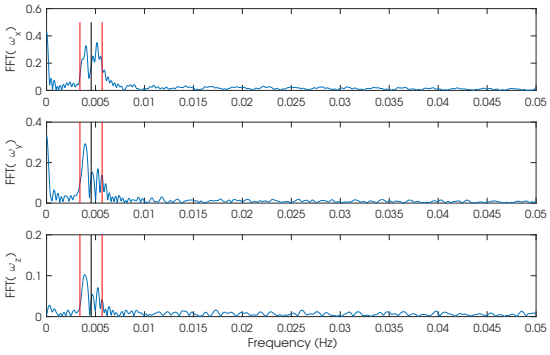

(b) Frequency analysis of the angular rates. The vertical lines indicate minimal, maximal, and mean estimated frequencies.

Figure 3.1: Frequency analysis of the angular rates as recorded on November 10th 2015.

Thus, the smoothing filters are configured such that this frequency is well within the allowed bandwidth. A re-sampling of a 20 second interval corresponding to a maximal bandwidth of 0.025 Hz has been chosen for the following numerical analysis in order to allow a wide range of magnetic dipole moments to be estimated.

3.2.2 Smoothing and Numeric Derivation

Smoothing is done using a local regression algorithm using weighted linear least squares and a 2nd degree polynomial model that assigns lower weight to outliers in the regression. The method assigns zero weight to data outside six mean absolute deviations (MathWorks, 2016) and the data is subsequently re-sampled to exact equidistant time intervals using a spline interpolation algorithm. The result of the smoothing of the gyroscopic data is exemplary shown in Figure 3.2a and Figure 3.2b.

At any re-sampled time instance t_i that the satellite has recorded its current angular rate $\omega(t_i)$ together with the current Earth magnetic field $\mathbf{B}(t_i)$ two of the terms in Eq. (3.17) can be computed if the inertia tensor I and the magnetic dipole moment μ are known. For three consequent recordings t_i the angular acceleration $\dot{\omega}(t_i)$ can be approximated as

$$\frac{\mathrm{d}\omega}{\mathrm{d}t}(t_i) \approx \frac{\omega(t_{i+1}) - \omega(t_{i-1})}{t_{i+1} - t_{i-1}} = \frac{\omega(t_i + \Delta t) - \omega(t_i - \Delta t)}{2\Delta t}, \tag{3.23}$$

where $\Delta t = t_{i+1} - t_{i-1}$ is the (re-)sampling interval.

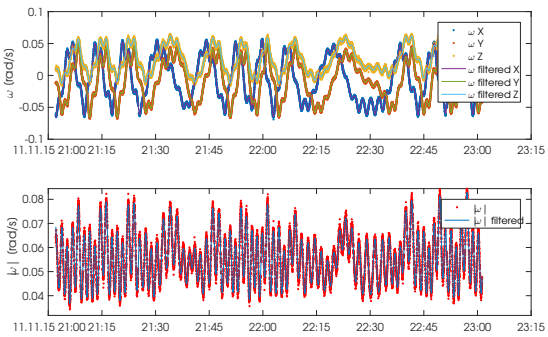

(a) Angular rate over the complete data recording.

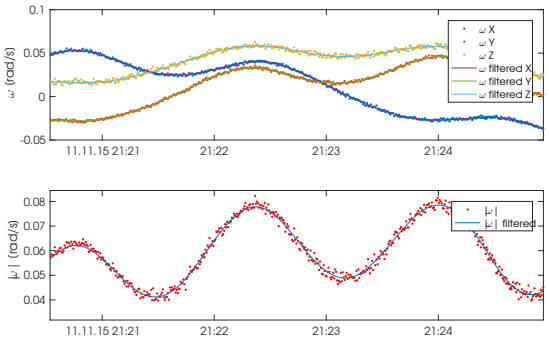

(b) Zoom-in on the filtered dataset. The resampling interval was set to 20 seconds.

Figure 3.2: Angular rate data as sampled by the on-board gyroscopes on November 11th 2015 and subsequent filtering.

3.2.3 Objective Function

In order to find the residual magnetic dipole moment μ best describing the satellite's dynamical behavior as expressed in Eq. (3.17) a quadratic objective function E for the minimization process is defined as

$$E(\mu, I) = \frac{1}{N}\sum_{i}^{N}\sqrt{\left(\mathbf{T}_{\mu}(t_i) - \mathbf{T}_{e}(t_i)\right)^2} \tag{3.24}$$

$$= \frac{1}{N}\sum_{i}^{N}\sqrt{\left(\mu \times \mathbf{B}(t_i) - I\dot{\omega}(t_i) - \omega(t_i) \times I\omega(t_i)\right)^2}. \tag{3.25}$$

The inertia matrix of UWE-3 has been estimated prior to launch using the CAD drawing of the satellite but actual tests to measure the moment inertia were not performed. While for traditional satellites it is a standard procedure to measure the inertia moments, at least on subsystem level, it is of less importance for miniature satellites. Due to their overall small moments of inertia only few test facilities can provide more precise measurements than what can be expected from a detailed CAD drawing. Therefore, nevertheless the inertia matrix can be estimated in different other ways, the procedure presented here includes the precise estimation of the satellite's inertia matrix together with the residual dipole moment.

The trivial solution of this minimization function of $\mu = \mathbf{0}$ and $I = \mathbf{0}_{3\times 3}$ needs to be prohibited by fixing one of the inertia tensor's entries. Thus, the algorithm estimates the magnetic moment as a function of the fixed moment of inertia entry. This however, as will be shown in a later section, is merely a normalization factor that can also be estimated using the controlling magnetic attitude actuators or, as shown in the following section, by using the satellite's reaction wheel. Furthermore, the assumption of at least one well-known

inertia tensor entry is usually true even if it is only deducted from the satellite's CAD design.

The minimization is carried out using the MATLAB `fminsearch` function with 8 independent parameters to be optimized. Those are the three entries of the residual dipole moment vector and 5 independent entries of the inertia tensor (since the inertia tensor is a symmetric matrix).

3.2.4 Normalization

A data set recorded during the reaction wheel checkout of UWE-3 can be used to estimate $I_{3,3}$. Shown in Figure 3.3a is the satellite's rotation rate together with the reaction wheel speed while in Figure 3.3b the angular acceleration about the satellite's Z-axis α_z and angular acceleration of the reaction wheel α_{wheel} are shown.

The reaction wheel is mounted in the satellite's Z-axis such that the dynamic equation reduces to the 3rd component of the satellite's angular rate:

$$\begin{aligned} I_{wheel}\dot{\omega}_{wheel} = {} & I_{1,3}\dot{\omega}_x + I_{2,3}\dot{\omega}_y + I_{3,3}\dot{\omega}_z \\ & + I_{2,1}\omega_x^2 - I_{1,2}\omega_y^2 + \omega_x\omega_y\left(I_{2,2} - I_{1,1}\right) + \omega_z\left(I_{2,3}\omega_x - I_{1,3}\omega_y\right). \end{aligned} \tag{3.26}$$

Since the satellite's attitude determination and control system's coordinate system is linked to the satellite's symmetric geometry, the inertia tensor's off-diagonal entries can be neglected for this analysis, reducing Eq. (3.26) to

$$I_{wheel}\dot{\omega}_{wheel} = I_{3,3}\dot{\omega}_z + \omega_x\omega_y\left(I_{2,2} - I_{1,1}\right). \tag{3.27}$$

The principal axes of inertia of the satellite are similar such that the term $\omega_x\omega_y\left(I_{2,2} - I_{1,1}\right)$ can also be neglected for this estimation. Doing so, the inertia tensor's entry $I_{3,3}$ can be computed for the various data points as shown in Figure 3.4. The numerical estimation of $I_{3,3}$ leads to a value of

$$I_{3,3} = 0.001\,981\,\mathrm{kg\,m^2}. \tag{3.28}$$

This value will be considered as fixed entry in the inertia tensor and all other entries as well as the magnetic dipole are estimated accordingly. Again, this entry however can be considered as normalization factor and is not essential for attitude control because all other involved quantities (i.e. the remaining 5 independent entries of the inertia tensor, the residual dipole moment, and the dipole moment excited by the magnetic torquers) also are multiplied by this factor. Considering $\tilde{x}$ to be the physically true (and unknown) quantity

of x and $I_{3,3}$ has been estimated as approximation such that

$$\tilde{I}_{3,3} = \gamma I_{3,3} \tag{3.29}$$

with γ being an unknown (and not observable) scaling factor. Then, because all other components of I are estimated in relation to $I_{3,3}$, the true inertia tensor $\tilde{I}$ is defined as

$$\tilde{I} = \gamma I, \tag{3.30}$$

and Eq. (3.17) can be re-written as

$$\begin{aligned} \tilde{I}\dot{\omega} + \omega \times \left(\tilde{I}\omega\right) &= \tilde{\mu} \times \mathbf{B} && (3.31)\\ \gamma I\dot{\omega} + \omega \times (\gamma I\omega) &= \tilde{\mu} \times \mathbf{B} && (3.32)\\ \gamma(I\dot{\omega} + \omega \times (I\omega)) &= \tilde{\mu} \times \mathbf{B} && (3.33)\\ \Rightarrow \tilde{\mu} &= \gamma\mu && (3.34) \end{aligned}$$

This has no influence on the attitude control algorithms as long as the magnetic torquer's moment is estimated in-orbit using the same scaling factor or I. This is shown in Chapter 3.3.

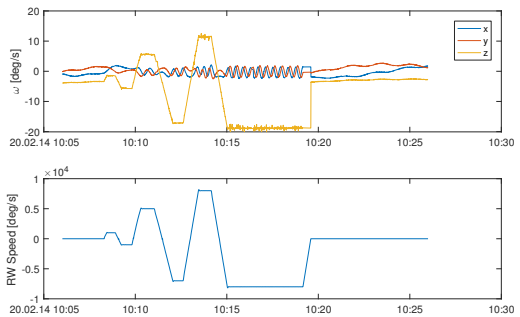

(a) Angular rate data and reaction wheel speed as sampled by the on-board gyroscopes on February 20th 2014 during the reaction wheel checkout procedure.

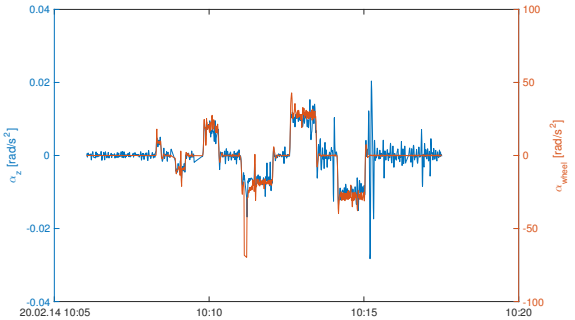

(b) Angular acceleration α_z and reaction wheel acceleration α_{wheel}.

Figure 3.3: Data recording during reaction wheel checkout procedure that is now used to determine $I_{3,3}$.

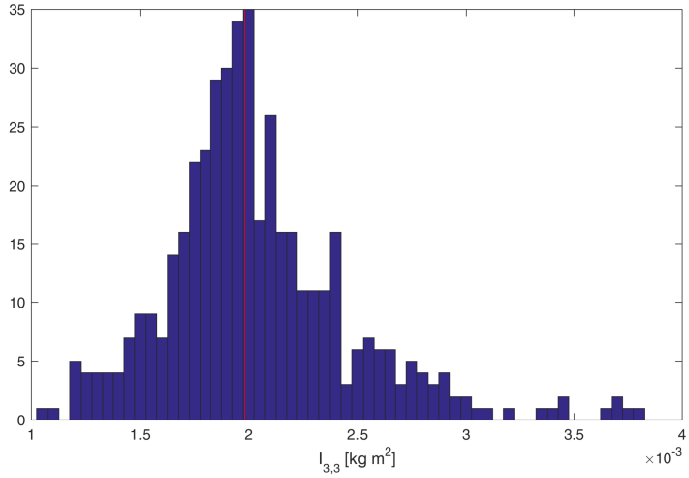

Figure 3.4: Histogram of the $I_{3,3}$ component as computed during the reaction wheel checkout recording. The red line indicates the estimated value of $I_{3,3} = 0.001\,981\,\mathrm{kg\,m^2}$.

3.2.5 Torque Estimation

The resulting torque $\mathbf{T}_e$ acting on the satellite is estimated by

$$\mathbf{T}_e(t_i) = I\dot{\boldsymbol{\omega}}(t_i) + \boldsymbol{\omega}(t_i) \times I\boldsymbol{\omega}(t_i), \tag{3.35}$$

while the torque excited by the residual magnetic moment μ is numerically estimated as

$$\mathbf{T}_\mu(t_i) = \mu \times \mathbf{B}(t_i). \tag{3.36}$$

The result of the optimization algorithm with respect to the fitting of the residual dipole torque to the experienced torque is shown in Figure 3.5 for four recordings throughout the lifetime of UWE-3. Shown are both components of the optimization algorithm $\mathbf{T}_e$ and $\mathbf{T}_\mu$. The good accordance of these estimations also over long term recordings as shown in Figure 3.5b justifies the approach.

There can be found different numeric values for the accordance and therefore also for the successful explanation of the acting disturbance torque. One is the minimized value of E_{min} which gives the average absolute value of the disturbance torque acting on the satellite that cannot be explained through the introduction of a constant magnetic dipole moment. This value for the recording shown in Figure 3.5c is $E_{min} = 3.7266 \cdot 10^{-7}\,\mathrm{N\,m}$ while the mean torque acting on the satellite is $\overline{|\mathbf{T}_e|} = 1.5568 \cdot 10^{-6}\,\mathrm{N\,m}$. This means, that about 76% of the original torque acting on the satellite can be explained by a constant magnetic dipole moment. However, this number includes sensor noise from gyroscopes

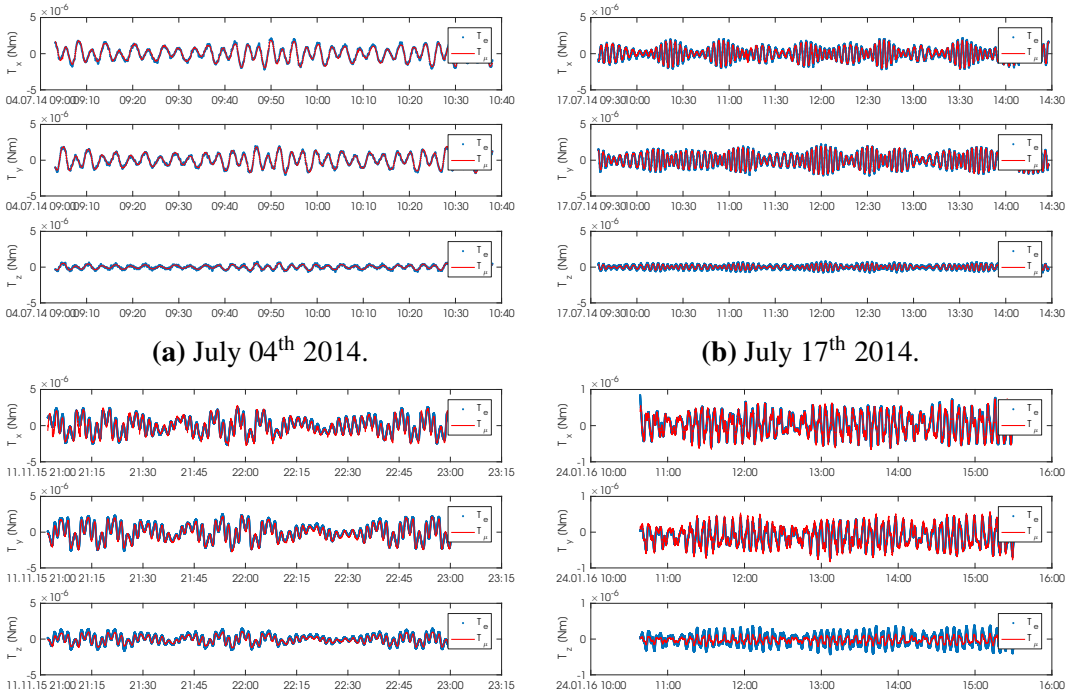

(a) July 04th 2014.

(b) July 17th 2014.

(c) November 11th 2015.

(d) January 24th 2016.

Figure 3.5: The experienced torque $\mathbf{T}_e$ and the torque excited by the residual dipole moment $\mathbf{T}_\mu = \mu \times \mathbf{B}$.

and magnetometers which is propagated to the estimation of the external torque and the magnetic dipole torque through $\omega(t_i)$, $\dot{\omega}(t_i)$, and $\mathbf{B}(t_i)$.

The minimal value of E only gives insight in the absolute value while a differentiated analysis may be advisable for each axis. Therefore, the difference of the external torque and the magnetic dipole torque is calculated for each axis and compared. For the example case shown in Figure 3.5c the remaining unexplained torque component of each axis is shown in Figure 3.6a. The original RMS of the torque acting on the satellite is $[1.124, 1.101, 0.653]\,\mu\mathrm{N\,m}$ for the x-, y-, and z-axis, respectively. The remaining RMS of the signal after subtracting the torque exerted by the found magnetic dipole is $[0.2787, 0.1949, 0.2455]\,\mu\mathrm{N\,m}$. This corresponds to a reduction of the unknown torque of $[75.2, 82.3, 62.4]\%$ in terms of RMS. Again, it should be noted, that this number includes a significant amount of sensor noise that translates into a higher RMS without having a physical meaning.

In order to check the residual torque for systematic behavior the normalized autocorrelation R of the torque is computed and shown in Figure 3.7. It can be seen that the torque acting on the satellite $\mathbf{T}_e$ shows a significant autocorrelation. The residual torque however has a quite small auto-correlation signal, which confirms the hypothesis that it is primarily

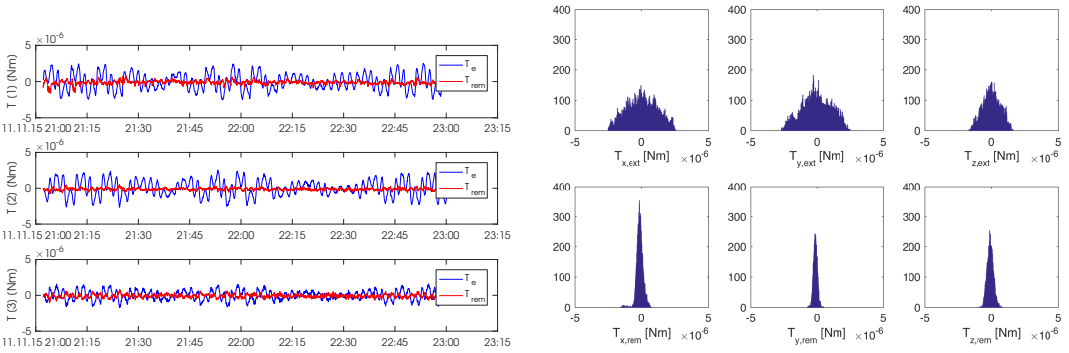

(a) Time series of $\mathbf{T}_e$ and remaining torque $\mathbf{T}_{rem}$.

(b) Histogram of $\mathbf{T}_e$ (top), $\mathbf{T}_{rem}$ (bottom)

Figure 3.6: External torque $\mathbf{T}_e$ and remaining torque $\mathbf{T}_{rem} = \mathbf{T}_e - \mathbf{T}_\mu$ for the recording also shown in Figure 3.5c.

white uncorrelated noise.

Nevertheless, there is a small systematic component persistent in the signal, causing the autocorrelation to have small side lobes and therefore to differ from a delta function at position zero. This component within the unexplained remaining torque can have different sources out of which minor miscalibrations of the sensors are expected to have the largest influence. However, this contribution is comparably small with respect to the dominating influence of the static magnetic dipole.

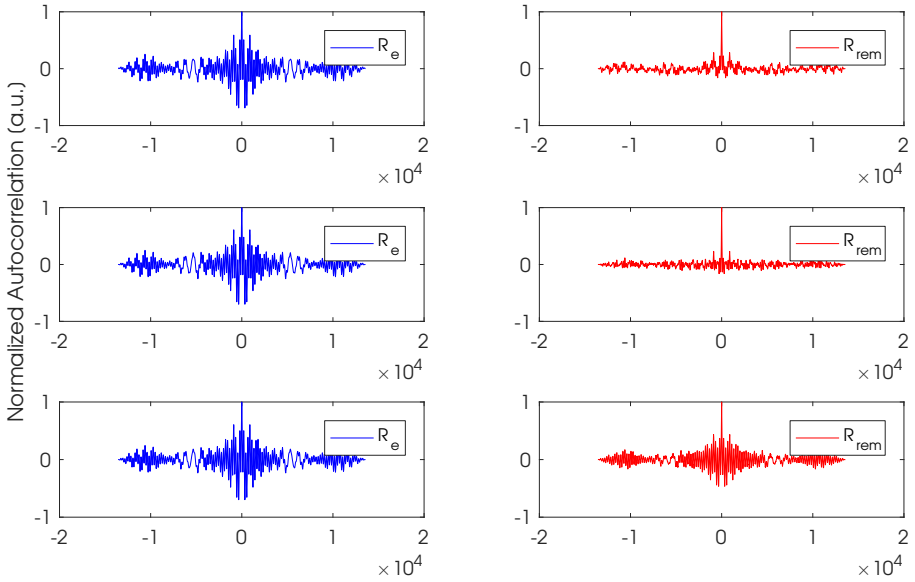

Figure 3.7: Normalized autocorrelation functions of $\mathbf{T}_e$ (left) and $\mathbf{T}_{rem}$ (right) (from top to bottom the individual x-, y-, z-components) for the recording also shown in Figure 3.5c.

3.2.6 Long Term Statistic

The residual magnetic dipole moment was estimated several times throughout the operational lifetime of UWE-3. The first time a data-set was dedicated to the dipole estimation was a recording from June 26$^{\text{th}}$ 2014. The last recording in the scope of this thesis was performed on April 12$^{\text{th}}$ 2016 and a total of 19 data-sets have been taken into account for the data analysis. The magnetic dipole moment estimated by the described analysis over the years is shown in Figure 3.8a together with a histogram of the estimation in Figure 3.8b. The numerical statistics of the residual magnetic dipole moment found over this timescale is given in table Table 3.2. The inertia tensor and magnetic dipole moment found by the long term analysis are

$$I_{est} = \begin{bmatrix} 2.0331 \cdot 10^{-3} & 7.2885 \cdot 10^{-6} & -2.3709 \cdot 10^{-5} \\ 7.2885 \cdot 10^{-6} & 2.0362 \cdot 10^{-3} & 1.3365 \cdot 10^{-6} \\ -2.3709 \cdot 10^{-5} & 1.3365 \cdot 10^{-6} & 1.9809 \cdot 10^{-3} \end{bmatrix} \text{kg m}^2 \tag{3.37}$$

$$\mu_{est} = \begin{bmatrix} 1.3076 \\ 15.9018 \\ -52.1570 \end{bmatrix} \cdot 10^{-3} \text{ A m}^2 \tag{3.38}$$

$$|\mu_{est}| = 54.5429 \text{ mA m}^2. \tag{3.39}$$

	X	Y	Z
Mean [mA m^2]	1.31	15.90	-52.16
Standard Deviation [mA m^2]	2.56	1.96	1.88
Magnitude [mA m^2]		54.5	
Mean Angular Deviation [°]		2.59	
Angle Standard Deviation [°]		1.95	

Table 3.2: Statistics of the residual dipole moment analysis over the operational lifetime of UWE-3.

The dipole estimation yields the same results independent from the satellite's state of charge, orbital-position, illumination, or initial orientation. Its constant direction (in body coordinates) and strength over the long period of time indicate that it is in fact excited by magnetic material inside the satellite. Additional magnetic effects due to charging, solar-array, or subsystem supply currents may be present but play a minor role and are included in the uncertainty estimation.

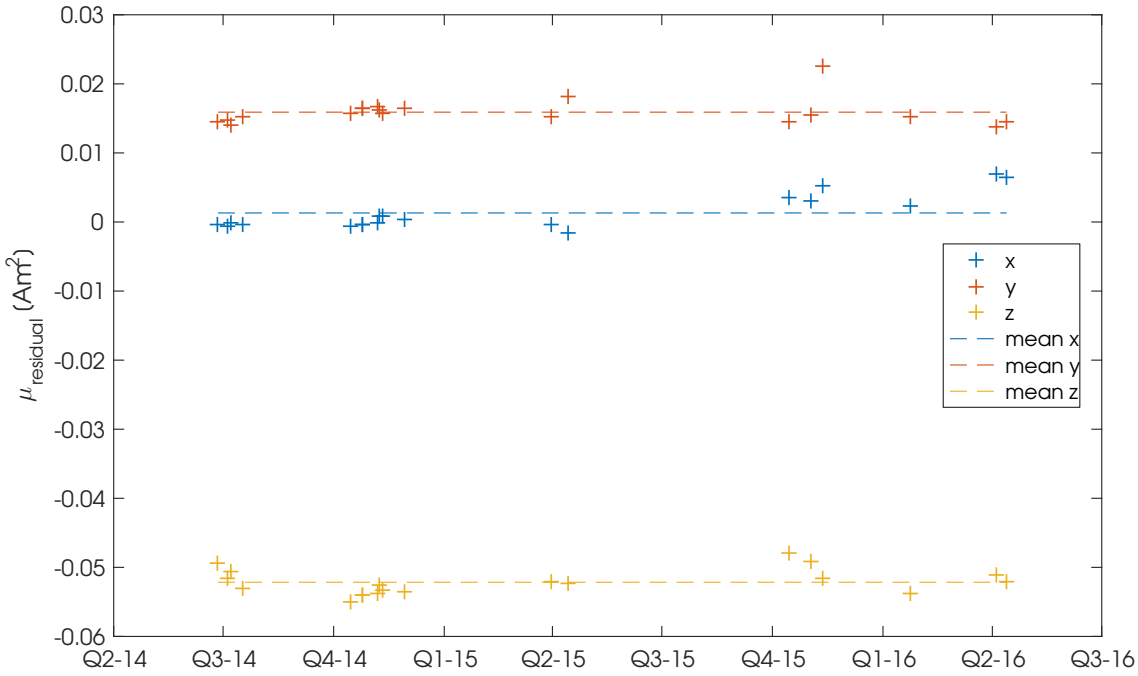

(a)

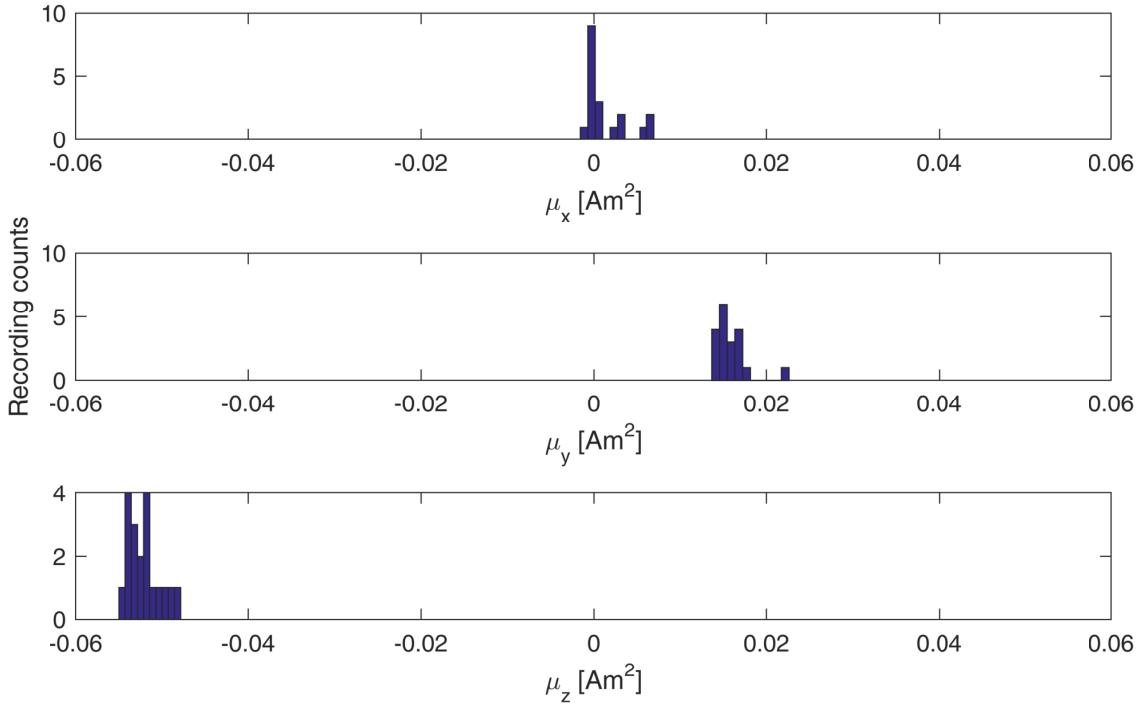

(b)

Figure 3.8: Magnetic dipole estimation throughout the operational lifetime of UWE-3.

3.2.7 Cause of Residual Dipole Moment

The constant nature of the residual dipole motivated the search for its cause in order to avoid magnetic contamination of future UWE satellites.

The dipole mainly lies in the satellite's Z-axis, as shown in Figure 3.9. Large material components that are elongated in this axis are only the satellite's aluminum bars (non-magnetic) and its UHF antennas. The satellite's main screws run along the body X-axis and can therefore be excluded from the analysis. This limits the list of potential causes to internal magnetic fields in the batteries, the reaction wheel (located close to the +Z-Panel on the ADCS board) and the satellite's antennas.

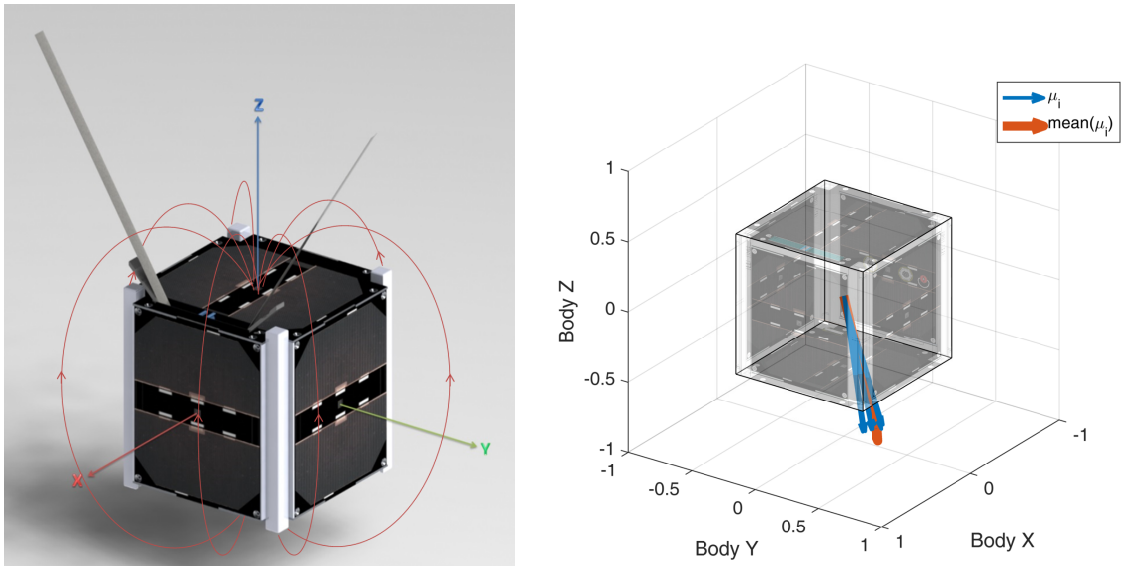

Figure 3.9: Visualization of the magnetic dipole in the satellite's Body reference frame. The antennas have been identified as the most probable cause for the internal dipole moment.

During ground-testing with the engineering model all investigated components have been screened for magnetic active material. The reaction wheel and batteries did not show any reaction to a magnet placed closely to the components and could therefore be eliminated from the list of potential causes. The UHF antennas however could be magnetized and would react to an external magnetic field.

As it is custom in the field of CubeSats the 170 mm UHF antennas have been made from measuring tape made out of stainless steel. This material provides genuine properties in terms of flexibility for stowage during launch, is quite light weight, is not very susceptible to thermal changes, and stays flexible at low and high temperatures. Furthermore, and this may be the main reason why it is so frequently used for nano-satellites, it is very low

cost and easily available. However, it poses a high risk of strong magnetic disturbances on such small satellites and therefore it has been decided to avoid this type of antenna on future UWE satellite. Instead, CuBe will be used as it provides similar positive material characteristics but is not magnetizable at the same time.

The influence of the magnetic dipole on the satellite's attitude control system has been significant and the controllers originally implemented did not perform as expected. As the work to understand the disturbance was ongoing, contact with other CubeSat teams had been established. Notably the team from ESTCube-1 experienced large disturbances on their satellite themselves and we established a cooperation to investigate upon it. The magnetic dipole estimation of other participating CubeSat teams is described in the following section.

3.2.8 Magnetic Dipole Moment Estimation of Other CubeSats

The discovery and precise estimation of the magnetic dipole of UWE-3 was perceived by other CubeSat development teams as well and interest in a similar analysis for their satellites had been expressed by some teams. In particular, the teams from ESTCube-1 and BEESAT were able to provide in-orbit data to estimate their respective residual magnetic dipoles.

3.2.8.1 ESTCube-1

ESTCube-1 was a 1U CubeSat developed by a student team from University of Tartu, Estonia, that was launched into a 670 km sun-synchronous low Earth orbit on May 7$^{\text{th}}$ 2013 aboard the second Vega flight from Kourou. It was funded by the European Space Agency in the scope of the Plan for European Cooperating States (PECS) and was the first Estonian satellite. Its main scientific goal was the active deployment of a tether in order to perform an electric solar wind sail (E-sail) experiment (Latt et al., 2014). The satellite carried a small camera which downlinked its first image already on May 15$^{\text{th}}$ 2013. Early operations of the satellite were used for several software updates of all systems and it was discovered that the pre-launch calibrated attitude sensors needed to be recalibrated in-orbit for which also the camera's images were used. It was found, that the ADCS eventually could estimate the satellite's attitude to better than 1.5° (Slavinskis et al., 2015, 2016).

The attitude control system was designed to support fast spin maneuvers of the satellite, targeting about $360°/\text{s}$. This was needed for the deployment of the tether by centrifugal forces which then should be reeled out by a dedicated drive unit. Furthermore, for the E-sail experiment to be successful and in order to avoid tangling of the reeled out 15 m

tether, the satellite was supposed to align its spin axis with the Earth's polar axis and stabilize it to better than 3°.

Unfortunately, the tether failed to deploy at $50°/s$ rotational speed, presumably due to a malfunction in the reel locking mechanism. The team subsequently tried to spin up the satellite for increased centrifugal forces and achieved a top angular velocity of $841°/s$ (Ehrpais et al., 2016). However, it had to be realized that ESTCube-1 aligns with the Earth's magnetic field and that the required attitude control maneuvers for tether deployment could not be performed as expected. On February 17th 2015 the satellite was officially retired, having completed its scientific mission, and on May 19th 2015 ESTCube-1 stopped operating due to degrading power production of the satellite's solar panels. Nevertheless, "the ESTCube mission can be considered very successful" and it could be shown that "the electron gun of the electric solar wind sail worked, but unfortunately the most important tether could not be deployed" (Mart Noorma, supervisor of the student satellite project, Associate Professor of the Institute of Physics of the University of Tartu and the Head of Department of Space Technology of Tartu Observatory, according to the ESA's website eoPortal (European Space Agency: eoPortal – Sharing Earth Observation Resources, 2017)).

In order to analyze the magnetic dipole of the satellite, the engineering model of ESTCube-1 was investigated thoroughly in a magnetic test facility. It was found that substantial parts of the battery casing and the stack connectors were made of ferromagnetic materials exciting a magnetic moment of about $0.096\,\mathrm{A\,m^2}$ in magnitude. However, the engineering model did not carry the flight model's electron emitter and the side panels' attachment screws were omitted for the test. Furthermore, slightly different materials were used for rods and spacers between the different subsystems. Soft magnetic materials present in the engineering model were not subject to the same treatment as within the flight model, leaving further uncertainties in the trustworthiness of the estimation procedure. The engineering model's residual dipole moment found by this investigation was $[-0.081, -0.035, 0.039]\,\mathrm{A\,m^2}$ (Ehrpais et al., 2016).

Therefore, the ESTCube-1 team decided to supply data for a magnetic dipole estimation as presented in Chapter 3.2. The data was recorded on January 25th 2014 and consisted of magnetic field and gyroscope samples at 2.5 Hz sampling frequency over about 35 min as shown in Figure 3.10.

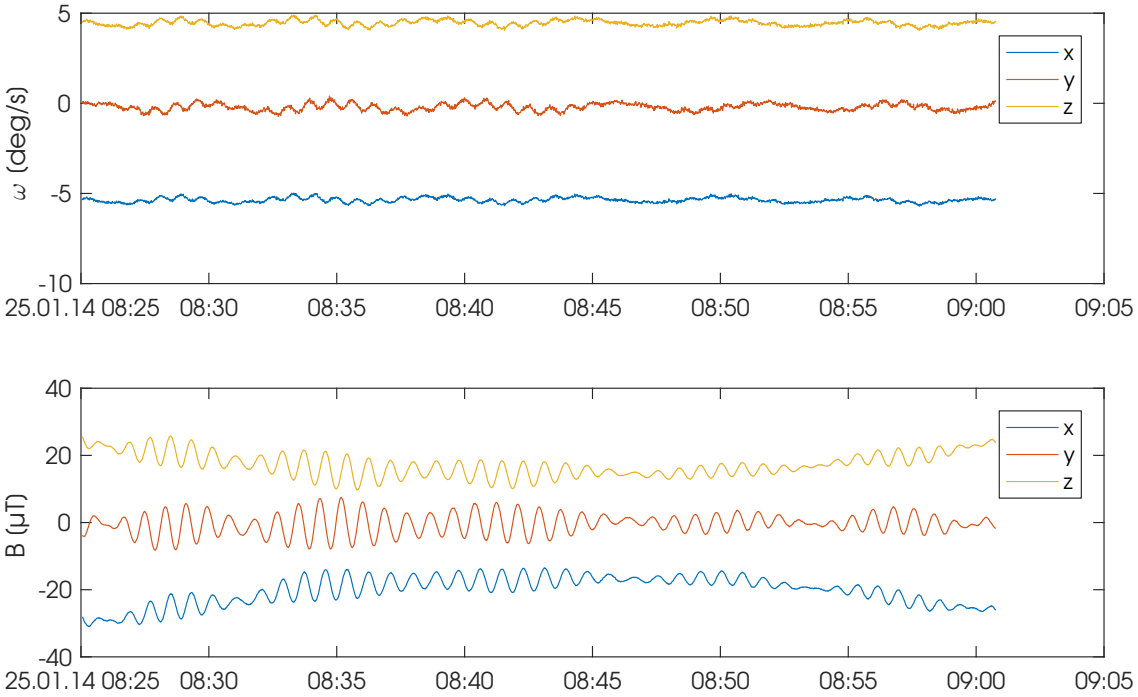

Figure 3.10: Angular rate and magnetic field data as sampled by ESTCube-1 on January 25th 2014.

The inertia matrix was given as

$$I_{ESTCube-1} = \begin{bmatrix} 1.8128 \cdot 10^{-3} & 23.7839 \cdot 10^{-6} & 41.7008 \cdot 10^{-6} \\ 23.7839 \cdot 10^{-6} & 1.9632 \cdot 10^{-3} & 28.7751 \cdot 10^{-6} \\ 41.7008 \cdot 10^{-6} & 28.7751 \cdot 10^{-6} & 1.7960 \cdot 10^{-3} \end{bmatrix} \mathrm{kg\,m^2} \tag{3.40}$$

and the residual magnetic dipole moment found was

$$\mu_{ESTCube-1} = \begin{bmatrix} -98.698 \\ 0.920 \\ 95.293 \end{bmatrix} \cdot 10^{-3}\,\mathrm{A\,m^2} \tag{3.41}$$

corresponding to a magnitude of

$$\left|\mu_{ESTCube-1}\right| = 137.2\,\mathrm{mA\,m^2}. \tag{3.42}$$

The rotation rate was comparably high for this type of analysis with a mean angular rate of $6.98\,^\circ/\mathrm{s}$, but nevertheless about $[48.0, 59.2, 51.6]\%$ of the RMS of the torque acting on the satellite can be explained by the found magnetic moment. Compared to the dipole estimated using the engineering model the satellite has a significantly larger dipole in its

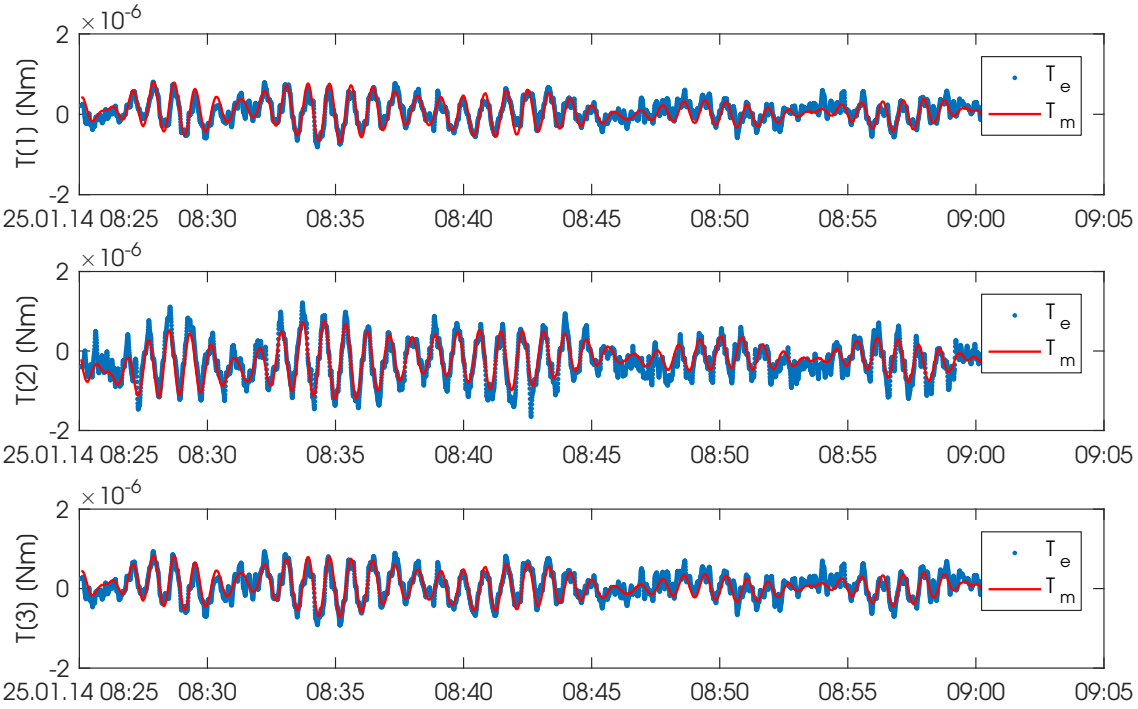

Figure 3.11: Torque analysis of the data sampled by ESTCube-1 on January 25th 2014.

Z-axis and less moment about its Y-axis. The angle between the engineering model's dipole and the one estimated for the flight model is about 28° and the difference in magnitude is 0.041 A m^2.

The dipole lies mainly in the CubeSat's -X– and Z–axis as shown in Figure 3.11. Unfortunately, the main cause of the residual dipole moment remains unresolved.

3.2.8.2 BEESAT-2

BEESAT-2 is the second Berlin Experimental and Educational Satellite developed by the Technical University of Berlin. This 1U-CubeSat has the objective to improve the validation of reaction wheels (RW-1, the same as used on UWE-3) and targets 3-axis stabilization using sun sensors, magnetic field sensors, magnetic coils and reaction wheels (Technical University of Berlin, 2017). It was launched on board a Sojus-2.1a from Baikonur, Russia, on April 19th 2013 together with the bio-satellite Bion-M1 and five other small satellites: AIST 2, BEESAT-3, Dove-2, OSSI 1 and SOMP. Although launched already in 2013, the satellite has just recently reached its full potential of the ADCS and 3-axis attitude control experiments using the reaction wheels started early in 2016.

The experience with UWE-3 motivated the BEESAT-2 team to exchange a data set of angular rate and magnetic field measurements in order to estimate the residual dipole

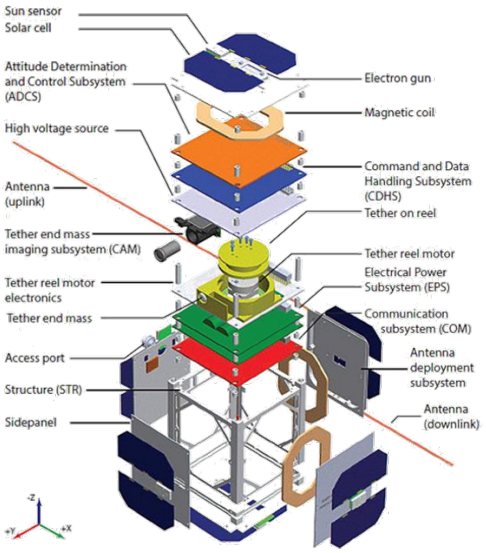

(a) Image credit: University of Tartu. (European Space Agency: eoPortal – Sharing Earth Observation Resources, 2017)

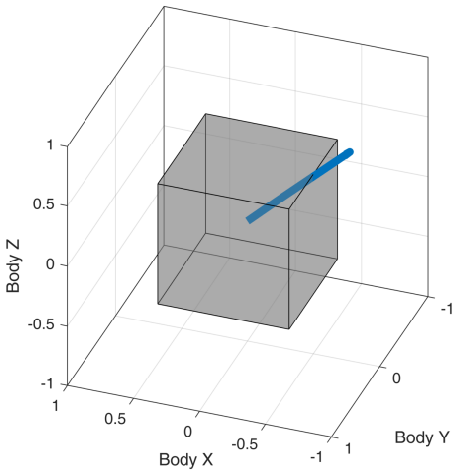

(b) The residual dipole of ESTCube-1 as determined by the dipole estimation lies predominantly in the satellite's -X– and Z–axis.

Figure 3.12: CAD model of ESTCube-1 and estimated magnetic dipole moment. Note, that the satellite structural representations are not aligned in their axis.

of the satellite. Although the satellite's reaction wheels can produce torques an order of magnitude higher ($23 \cdot 10^{-6}\,\mathrm{N\,m}$) than any expected magnetic dipole moment, knowledge of the latter could improve the attitude control performance.

The data set was recorded on November 16$^{\text{th}}$ 2016 specifically for this analysis. The data was re-calibrated as described in Chapter 2.1 of which the outcome is shown in Figure 3.13. The sampling rate of the gyroscopes and magnetometers was set to 1.54 s. The inertia matrix was normalized by the $I_{3,3}$ component given by $I_{3,3} = 2.5484 \cdot 10^{-3}\,\mathrm{kg\,m^2}$ which originates from the satellite's CAD drawing.

The torque acting on the satellite and the torque excited by a constant dipole moment is shown in Figure 3.14. The torques are in the order of 500 nN m and it can be seen that the magnetic dipole torque is the dominating dynamical component. The RMS of $\left(\mathbf{T}_e - \mathbf{T}_\mu\right)$ is $[52.997, 67.915, 59.927]\%$ smaller than the RMS of $\mathbf{T}_e$. The dipole and inertia tensor estimated by this analysis are

$$I_{BEESAT-2} = \begin{bmatrix} 2.4877 \cdot 10^{-3} & -8.0323 \cdot 10^{-6} & 6.6116 \cdot 10^{-5} \\ -8.0323 \cdot 10^{-6} & 2.3417 \cdot 10^{-3} & -6.9341 \cdot 10^{-6} \\ 6.6116 \cdot 10^{-5} & -6.9341 \cdot 10^{-6} & 2.5484 \cdot 10^{-3} \end{bmatrix} \text{kg m}^2 \quad (3.43)$$

$$\mu_{BEESAT-2} = \begin{bmatrix} 18.453 \\ -13.900 \\ 0.410 \end{bmatrix} \cdot 10^{-3} \text{ A m}^2. \quad (3.44)$$

The magnitude of the residual dipole is 23.106 mA m^2.

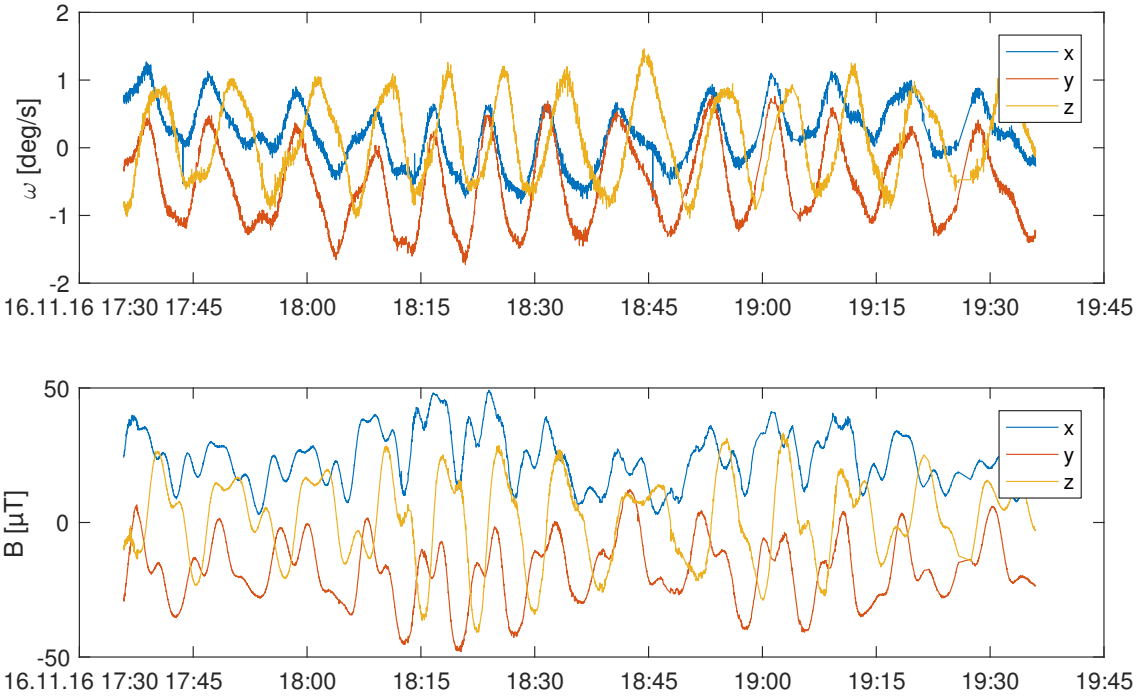

Figure 3.13: Angular rate and magnetic field data as sampled by BEESAT-2 on November 16$^{\text{th}}$ 2016.

3.3 Magnetic Torquer Moment Estimation

Having analyzed the magnitude and direction of the residual magnetic dipole moment of UWE-3 its compensation and impact on the attitude control of the satellite moved into focus. The satellite carries an air coil on each side panel and is able to operate it in '`forward`', '`reverse`', or '`off`'. In theory, the torquers should create a magnetic dipole moment of 0.028 A m^2 which further needed experimental verification. Especially,

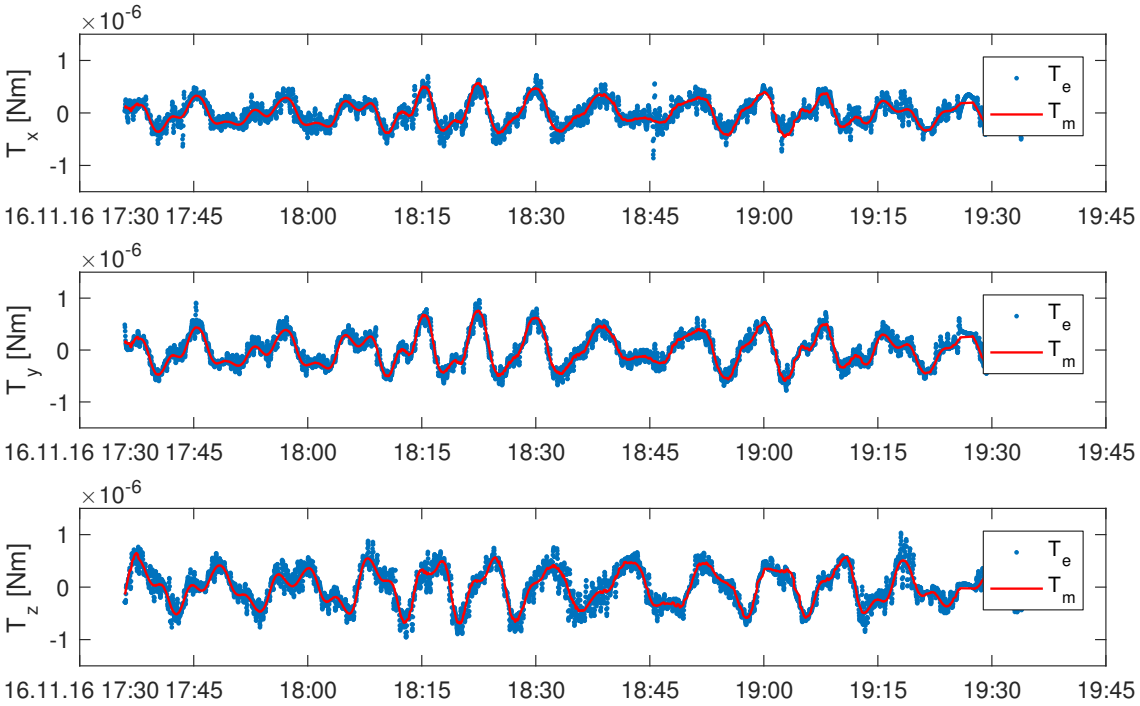

Figure 3.14: Torque acting on BEESAT-2 and the corresponding torque excited by a constant dipole moment.

since the torquers are driven by the unregulated battery voltage which may vary roughly between 3.7 V and 4.2 V, depending on the batteries' state of charge, the torque at a typical battery load needed to be measured. Having two torquers in each axis, the ADCS theoretically is able to produce a magnetic moment of 56 mA m^2 per axis. Keeping in mind that the residual dipole moment has a magnitude of 54.5 mA m^2 and a major component of -52.2 mA m^2 it was unclear if the residual dipole can be compensated completely.

A first verification experiment was performed on November 22$^{\text{nd}}$ 2014 after a mandatory software update of the ADCS. Through the software update the scripting language called *Tinytus* (Dombrovski, 2015) was installed with which scripts could be run on board of the ADCS. The script to estimate the satellite's torquer strength and to prove it can compensate the residual dipole programmed in the first half of a data recording the Z-axis torquers to counteract the residual dipole such that they were continuously switched on in +Z-direction (+Z-torquer '`forward`', -Z-torquer '`reverse`'). Then, the torquers were switched off in order to measure the residual dipole moment for this instance.

The data recorded is shown in Figure 3.15. It can clearly be seen, that the satellite behaves significantly different while the torquers are switched on than when it is only subject to its natural residual dipole. Furthermore, it is easily visible that although care had been taken during the software update to integrate the Tinytus scripting correctly, the

magnetic field strength during torquer activation is significantly higher and varying. This is due to the fact, that at this point of software development only a loose coupling between torquer switching and magnetic field measurements was implemented. This issue was resolved with a later update in 2015.

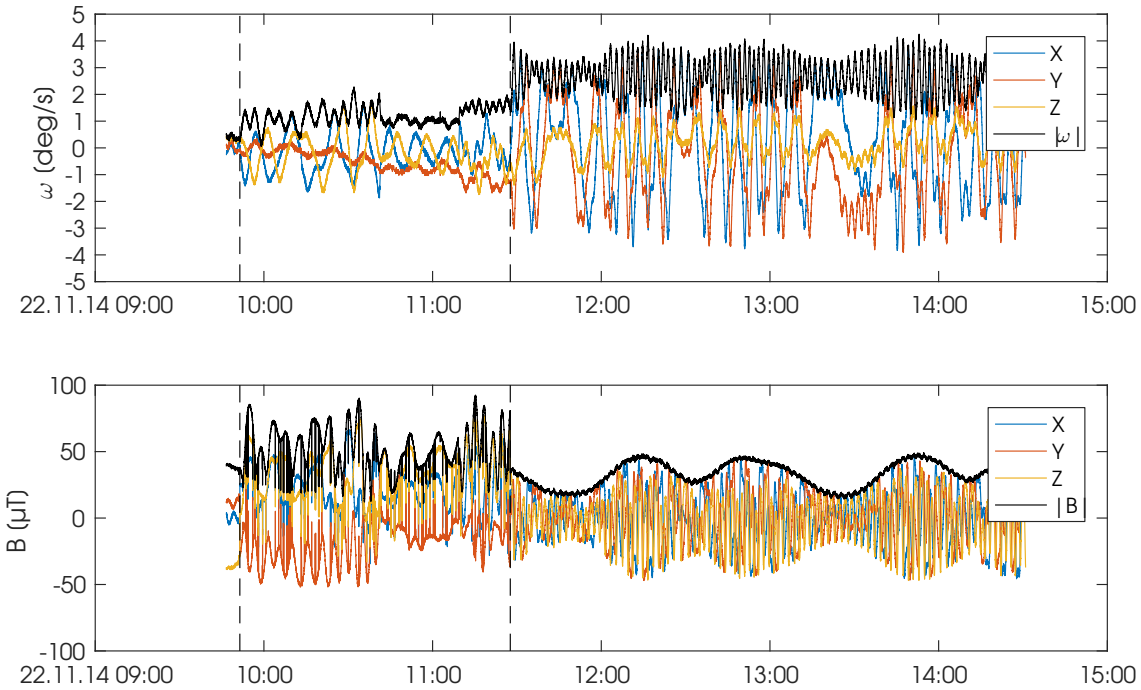

Figure 3.15: Data recorded on November 22nd 2014 in order to estimate the (Z-)torquers' strength.

The magnetic field data needed to be corrected for the contribution of the two torquers in magnitude and direction in order for the analysis to perform correctly. This was done by identifying the offset that is introduced to the magnetometers' measurements by the magnetorquers. It was found to cause an offset of

$$\mathbf{B}_{offset} = \begin{bmatrix} 26.9 & -40.2 & 37.0 \end{bmatrix}^T \mu\text{T}. \tag{3.45}$$

The corrected magnetic field data is shown in Figure 3.16.

The torque analysis is shown in Figure 3.17 and the Z-axis torquers' magnetic dipole moment could successfully be determined as the difference between the dipole acting in

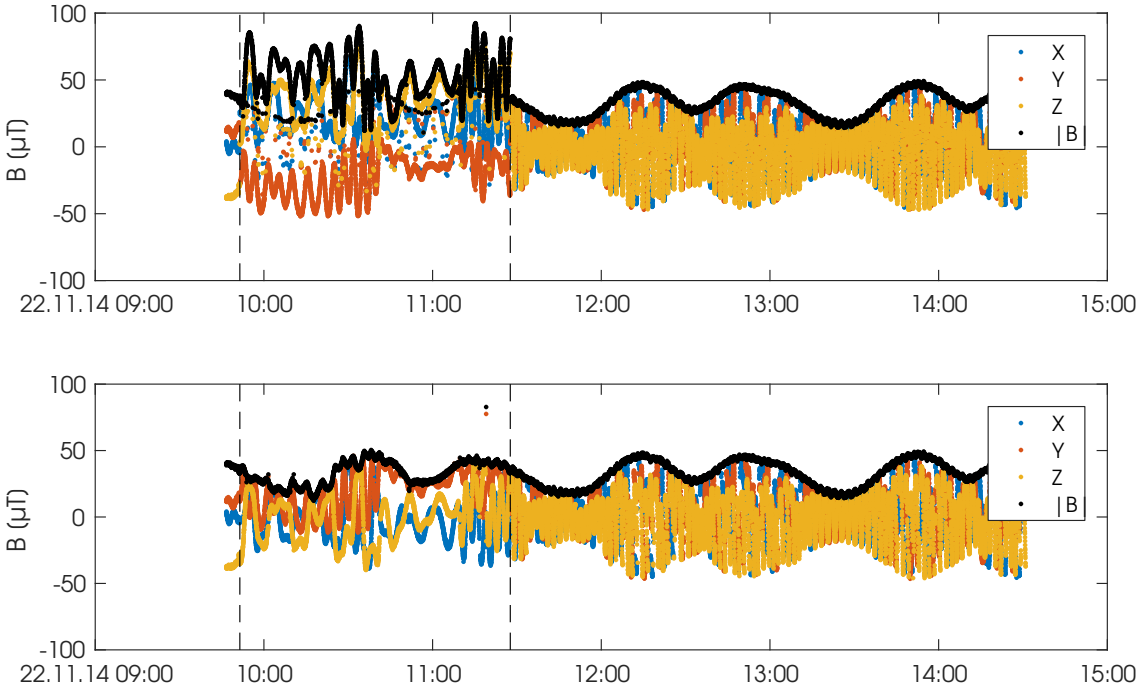

Figure 3.16: Magnetic field data before (top) and after (bottom) offset compensation.

`on` (Figure 3.17a) and `off` (Figure 3.17b) state:

$$\begin{aligned} \mu_{\texttt{off}} &= \begin{bmatrix} -0.83 & 15.70 & -55.26 \end{bmatrix}^T \text{mA m}^2 \\ \mu_{\texttt{on}} &= \begin{bmatrix} -2.91 & 15.31 & 1.70 \end{bmatrix}^T \text{mA m}^2 \\ \mu_{Z-torquers} &= \begin{bmatrix} -2.08 & -0.38 & 56.96 \end{bmatrix}^T \text{mA m}^2 \end{aligned} \tag{3.46}$$

This analysis validates that the torquers create the magnetic dipole intended by their design and that the distortion due to mounting inaccuracies and deflection by magnetic materials is not significant (about 2° from the intended Z-axis). In Figure 3.18 the 3D representation of the results are shown. The magnetic dipole moment excited by the torquers is plotted in blue, the residual dipole moment in black, and the resulting dipole moment when both Z-torquers are switched `on` in red. Furthermore, this analysis shows that the satellite's residual magnetic dipole moment can be completely compensated to zero. However, the excitation of a significant resulting magnetic moment in the positive Z-axis is not possible with UWE-3 which has a high impact on the attitude control of the satellite. This will be the subject of the following chapter.

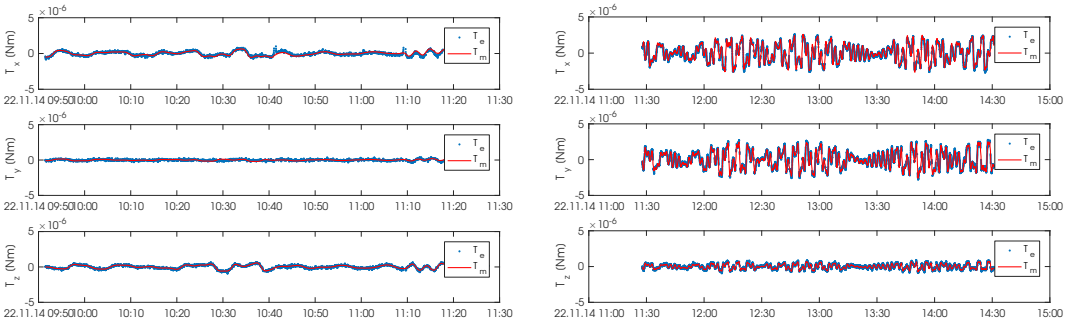

(a) Torquers `on`. **(b)** Torquers `off`.

Figure 3.17: Torque analysis with magnetic torquers `on` and `off` in order to estimate the torquers' magnetic dipole strength.

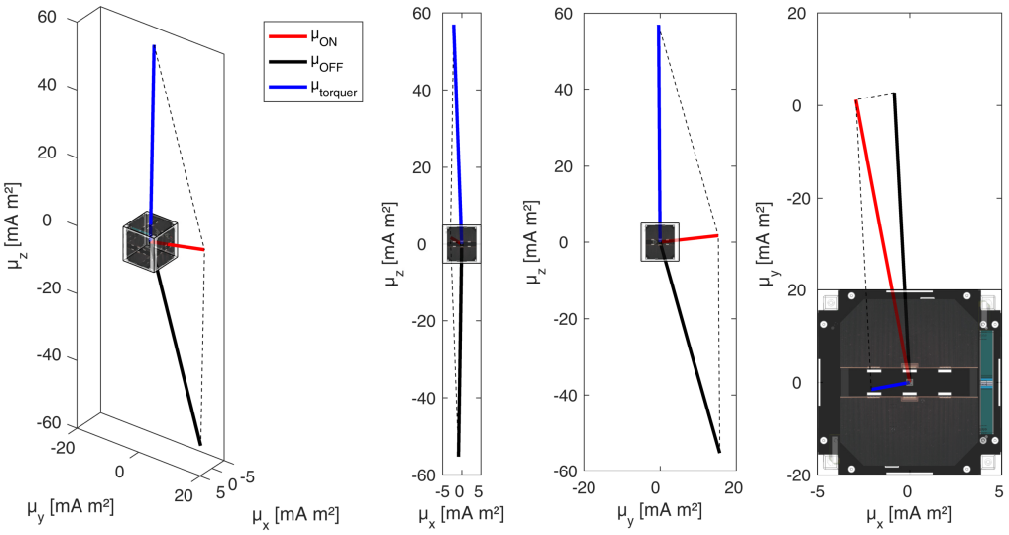

Figure 3.18: Magnetic dipole magnitude and direction of the attitude control magnetorquers.

3.4 On-Board Residual Magnetic Dipole Estimator

The residual dipole estimator calculates the numeric derivative of the on-board measured angular rate of the satellite. Then, it estimates which part of the numeric angular acceleration, including the derivative of the sensors' noise, can be explained by a static residual magnetic dipole moment. Due to the high influence of sensor noise on differential data the estimator has to be very slowly adapting the estimated dipole moment.

In each iteration of the attitude determination loop the algorithm estimates an error in its residual dipole estimation μ_{est} as

$$\Delta\mu_{est} = \frac{1}{|\mathbf{B}|^2}\mathbf{B} \times \left(I\frac{\Delta\omega}{\Delta t} - \mu_{est} \times \mathbf{B} \right), \tag{3.47}$$

where $\Delta\omega$ is the numeric difference between the last measured angular rate and its current value with Δt being the time difference of the two. This incremental correction of the estimated magnetic dipole can then be added to the currently valid estimation value which is available to the satellite's magnetic control algorithms. The evolution of such an estimation process is shown in Figure 3.19 for a simulation with a dipole moment and sensor characteristics of UWE-3.

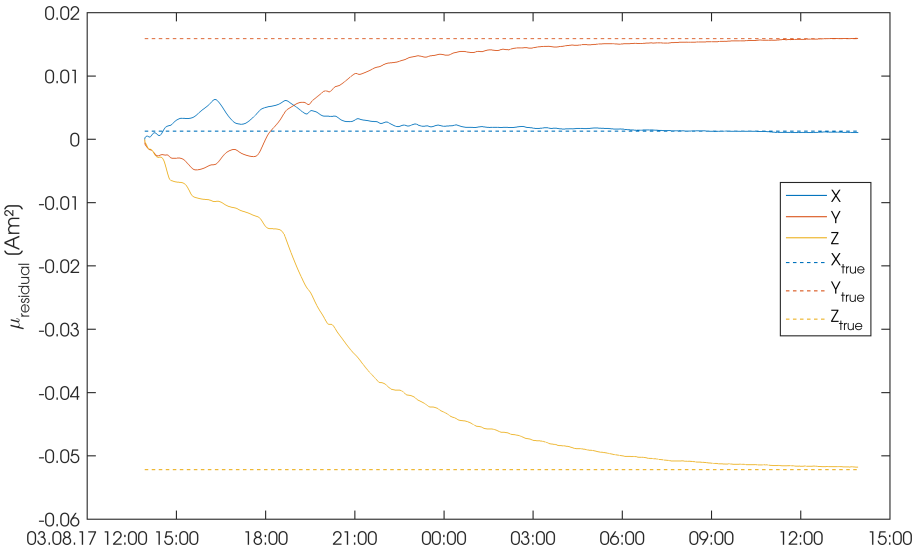

Figure 3.19: Residual magnetic dipole estimation of the hybrid attitude controller for UWE-4 and NetSat.

Clearly visible is the long duration the algorithm needs to adjust the dipole estimation to the correct value due to the low gain factor in order to prevent large deviations due to the differentiation of the sensor noise. At the end of the simulation, after 24 hours, the

algorithm estimates a dipole moment of

$$\mu_{est} = [0.00108,\ 0.01596,\ -0.05174]\,\mathrm{A\,m^2}, \tag{3.48}$$

while the simulated true value was set to

$$\mu_{true} = [0.00131,\ 0.01590,\ -0.05216]\,\mathrm{A\,m^2}. \tag{3.49}$$

The estimated value resembles the true value to $0.3\,\mathrm{mA\,m^2}$ in strength and $0.3\,^\circ$ heading.

Employing the on-board residual dipole estimation will help increase the overall pointing accuracy of the satellite, increase its thrust efficiency, and as such increase the orbit control accuracy for future missions. Of especial importance is such an automatic dipole estimation for multi-satellite missions such as NetSat. The algorithm presented here will be implemented on-board of UWE-4 for the first time and the adjustment of the gain parameters will be performed after having concluded the magnetometer in-orbit calibration.

3.5 Summary

In this chapter a method to estimate the residual magnetic dipole moment of a satellite in orbit has been developed. This analysis plays an important role for miniature satellites since the magnetic disturbance is by far the most significant attitude disturbance for this class of satellites.

The algorithm makes use of recorded magnetic field sensor and rate gyroscope data which is post-processed to determine the influence of a static residual magnetic dipole moment onto the satellite's dynamics. This method has been used to measure the dipole moment of UWE-3 in orbit over a period of almost two years. The results show that this satellite carries an inherent magnetic moment constant in direction and strength. Its magnitude is in the order of $50\,\mathrm{mA\,m^2}$ and presumably is caused by a magnetization of the satellite's antennas.

Furthermore, the procedure was tested on other CubeSats. Two teams, namely ESTCube-1 and BEESAT-2, provided data that was analyzed and their respective residual dipole moments were found. The results make clear that for this class of satellites the magnetic disturbance torque is by far the dominating component of the attitude dynamics. Although the magnitudes differ by a factor of 3:2:1 for ESTCube-1, UWE-3, and BEESAT-2, respectively, the developed algorithm is equally capable of estimating them. Their significance for the satellites' ADCS and their impact on the mission in general has been quite different,

ranging from a severe impact on the scientific/technological mission over a considerable degradation of the ADCS capabilities to a minor disturbance torque to be compensated when known.

The experience with this method allowed to implement an on-board residual magnetic dipole moment estimation that renders future miniature satellites capable of an online estimate of their disturbance. The focus here also is the efficient implementation in order for computational weak low-power micro-processors to run the program. Simulations show the program's capability and precision.

The precise estimation of the magnetic disturbance of a CubeSat imposes relevant changes to the programmed attitude control algorithms. In the following Chapter 4 a new attitude control architecture and algorithms are developed in order to cope with a large magnetic disturbance which was shown with in-orbit magnetic attitude control experiments on board of UWE-3.

4

Magnetic Attitude Control

In the following chapter a flexible attitude control architecture is presented that allows to easily implement a multitude of different attitude control laws and exchange them frequently in orbit. This architecture takes into account the dynamics of a small rigid satellite and is divided into several layers in order to act efficiently on the different time scales involved.

It was first introduced during operations of UWE-3 and specifically incorporates the attitude disturbance due to its magnetic dipole moment. Though its primary usage is for magnetic control the architecture can be used with any attitude control actuator such as reaction wheels, magnetorquers, or attitude control thrusters. The latter approach will be demonstrated in UWE-4 and is further described in Chapter 5.4.

Furthermore, the magnetic attitude control experiments conducted with UWE-3 in orbit are presented in the following chapter. Many publications have been issued throughout the development and experiments that stated the most recent progress in this area. In Bangert et al. (2012) and Reichel et al. (2013) the preparations and laboratory tests of the attitude control system prior to launch haven been presented. Bangert et al. (2014) and Busch et al. (2014b) were the first publications after launch in which the initial detumbling and checkout procedures have been addressed. The new attitude control architecture was first presented in Bangert et al. (2015b). Bangert et al. (2016) summarizes the spin-control experiments and evaluates the results with respect to their application for formation flying miniature satellites.

This chapter is organized as follows: at first, the attitude control architecture and its implementation are addressed in Chapter 4.1. In Chapter 4.2 the experiments carried out with UWE-3 related to detumbling of the satellite, as one of the most crucial procedures for any attitude control system of miniature satellites, are presented. Chapter 4.3 elaborates on attitude control experiments with the goal of spin-stabilization as preparation of thrust

vector control in the context of an orbit controlled satellite further elaborated in Chapter 5.

4.1 Attitude Control Architecture

The development of the UWE-3 attitude control system was mainly carried out in a Master's thesis (Reichel, 2012) that focused on the simulation and implementation of a set of control algorithms. Before the actual control algorithms could be implemented the necessary software infrastructure had to be developed. This comprised the low-level actuator switching, communication between the ADCS and outside panels, coordinate transformations, and plenty of other software fragments that support any attitude control procedure.

Significant progress was made in the field of the subsystems' communication which is fundamental for the execution of the control. Since the attitude determination solution and control algorithms are computed on the ADCS itself but the magnetic actuators are located on the outside panels an efficient communication scheme had to be found to accurately switch the actuators accordingly. For this purpose, a distributed control approach was chosen that out-sources certain control computations to the panels where the actuator switching can then be performed autonomously. For this, the panels were able to propagate the local magnetic field given by a measurement update from the ADCS using the measured angular rate. This approach was chosen to guarantee correct actuator switching even at high angular rates by minimizing the time between control output computation and actuator switching. However, correct timing between measuring the magnetic field and activating the magnetorquers has proven to be difficult, easy to disturb, and less efficient in this approach which is why this procedure was abandoned in a later software update of the ADCS.

The attitude control algorithms were simulated and implemented using hard-coded routines with some tuning parameters. All simulations performed before launch did not anticipate the problem of a large residual magnetic dipole but were rather concerned about large angular rates after deployment. This was due to the experience made by other CubeSat teams such as SwissCube (Noca and Ivanov, 2010) that had problems with a phase shift in the magnetorquer actuation due to a delay between control output computation and actuator switching in the presence of high spin rates after release from the upper stage.

Laboratory tests with any ADCS are very difficult to perform and thus only the most important detumbling algorithm was tested with hardware prior to launch. The tests were performed in a self-build air-bearing testbed with augmented ambient magnetic field. It could be shown that the satellite de-spins significantly faster with active detumbling control

than by natural decay due to the remaining friction.

4.1.1 Modular Generic Control Architecture

Already early in the UWE-3 mission the attitude determination system was characterized and optimized to a certain extent, e.g. an in-orbit calibration of the satellite's sensors was performed as presented in Chapter 2.1. During these experiments it was discovered that the satellite's motion is dominated by the influence of a residual magnetic dipole moment. As it became clear that this moment is static and has not changed significantly during the operational lifetime of UWE-3, new control strategies became the focus of ADCS operations. However, the implemented on-board attitude control software architecture did not support advanced control algorithms and a flexible exchange of parameters or routines. Therefore, a new control software architecture had to be develop in order to enable various attitude control experiments.

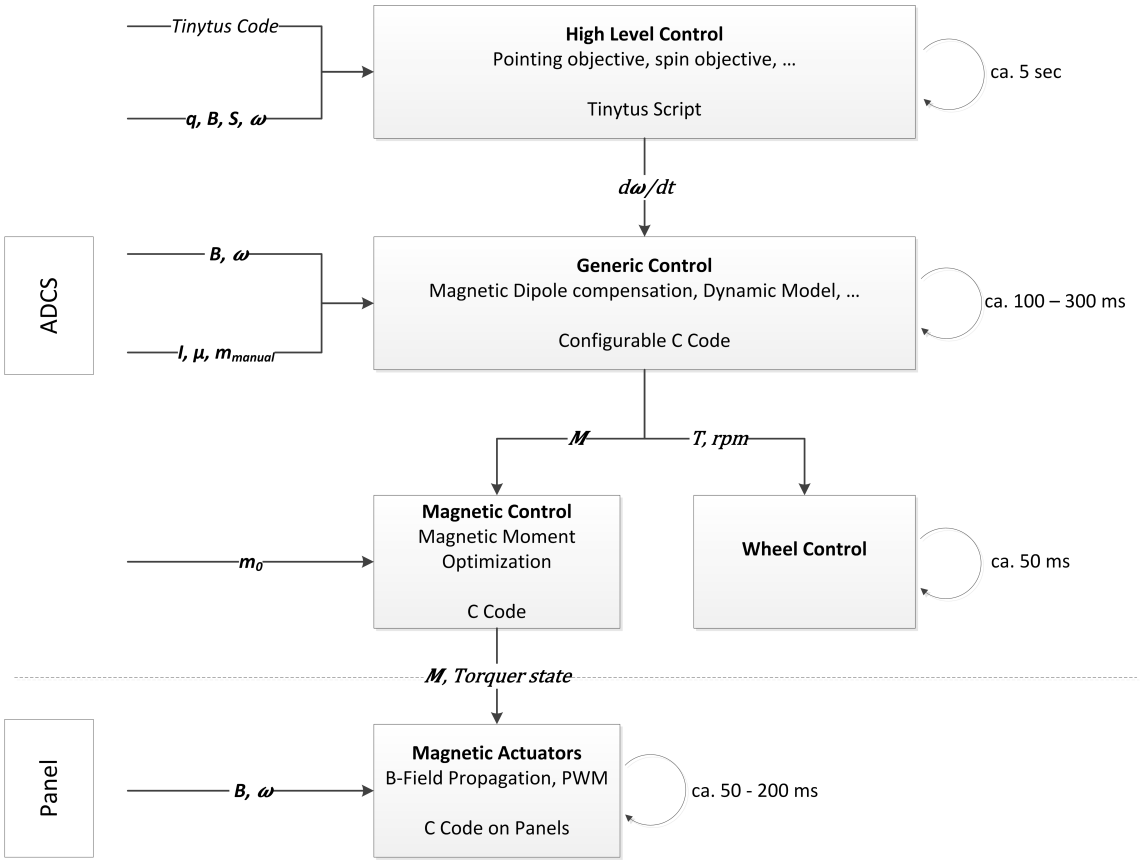

Figure 4.1: Attitude Control architecture on UWE-3 as introduced in Bangert et al. (2015b).

In February 2015, a complete update of the satellite's systems introduced a new control

system architecture on board of the ADCS (Bangert et al., 2015b). It was intended to facilitate experimenting with different control approaches by anticipating the satellite's dynamical behavior and automatically counteracting undesired disturbance torques. Furthermore, it made use of the Tinytus scripting language (Dombrovski, 2015), enabling frequent changes of the control algorithms and routines.

The general setup of the final architecture is shown in Figure 4.1. Attitude control is organized in a multi-layered architecture in order to account for the different time-scales involved in the task. The controller is driven by a high level controller implemented in the scripting language Tinytus, which calculates desired angular accelerations $\dot{\vec{\omega}}$ based on various inputs from the attitude determination system. The high-level controller ensures the accomplishment of a given objective, such as a certain spin-direction or even a desired pointing direction. For this task, Tinytus has access to a variety of ADCS specific library functions such as timing functionalities, basic attitude determination adapters such as reading the current quaternion from the Kalman Filter, sensor sampling and actuator activation functions, and useful mathematical algorithms such as coordinate transformation routines. Using this architecture, plenty of different control logics can be experimented with, such as pointing controllers, spin-stabilized, and spin-pointing algorithms. The uncomplicated exchange and safe execution of the high-level Tinytus controller allows to test even potentially faulty or risky software in orbit and thus accelerate the development process.

Tinytus is an efficient scripting language developed in the context of the UWE-3 mission and currently being further developed in cooperation with the Zentrum für Telematik e.V., Würzburg. The scripts are written in a dedicated Java-based integrated development environment and are subsequently compiled into byte-code that can be uploaded to the satellite's file system. The on-board micro-controllers can load the byte-code into their RAM from where a dedicated interpreter software routine executes the byte-code by translating the instructions into executable machine code. The basic interpreter is with about 350 lines of code very lightweight and available on board of UWE-3 for the processors of the OBDH and ADCS. The compiled script byte-code is usually in the order of several tens to some hundred bytes and can therefore easily be uploaded to the satellite. Using the file system of UWE-3 it is possible to upload a variety of scripts such that even complicated sequences of scripts can be executed.

Another benefit of the Tinytus interpreter is that it can be halted at any time during code execution and resume from the last instruction again. This is important when basic functionalities are to be executed by the system in the background without interference with a certain script currently running. For instance, when using a Tinytus script for

attitude control the ADCS shall perform attitude determination at the same time without it being handled by the Tinytus script. For this purpose, "`yield`" commands can be included in the Tinytus script at which the interpreter halts and the main program of the micro-controller is resumed. At the next call to the interpreter it resumes from where it was halted before.

Tinytus scripts of up to one kilobyte can be uploaded into the satellite's file system and are then transferred to the ADCS' RAM. Each of these steps is ensured using checksums and scripts can only be executed when the checksum matches the according command. The interpreter is configured with a start time, duration, task update period, and maximum number of allowed interpreting steps. The task update period defines at which rate the interpreter is given time to operate. This further facilitates the script implementation, since precisely timed execution does not have to be implemented in Tinytus but is ensured by the surrounding program.

The second stage of the control architecture is a generic controller that has dedicated knowledge about the satellite's dynamics and in particular about its residual dipole moment. Therefore, it computes the required torque to cancel unwanted dynamical behavior in order to achieve the angular acceleration given as input by Tinytus. The generic control law implemented in the second stage of the controller is formulated as

$$\mathbf{T}_c = I\dot{\omega} + \omega \times (I\omega) - \mu \times \mathbf{B} + \mathbf{T}_{manual} + \mathbf{T}_{ECI2body}, \tag{4.1}$$

where $\mathbf{T}_c$ is the derived control torque, I the inertia matrix, ω the angular rate, μ the residual dipole, and $\mathbf{B}$ the magnetic field. All terms are expressed in body coordinates of the satellite, while $\mathbf{T}_{ECI2Body}$ represents a torque expressed in ECI coordinates and subsequently transferred into body coordinates using the actual attitude estimation. $\mathbf{T}_{manual}$ is a manually configurable moment that is applied in each step of the controller, for instance in order to de-saturate reaction wheels.

The derived control torque $\mathbf{T}_c$ is used to calculate the magnetic moment $\mathbf{m}_{ctr}$ to be applied via

$$\mathbf{m}_{ctr} = \frac{1}{\mathbf{B}^2}(\mathbf{B} \times \mathbf{T}_c) + \mathbf{M}_{man}, \tag{4.2}$$

where $\mathbf{M}_{man}$ is a configurable static magnetic moment. The desired magnetic moment then is passed on to the third stage of the controller that can either be executed by the satellite's panels' micro-controllers that have direct control over the magnetorquers or can also be run on the ADCS. In order to better synchronize the magnetic actuators and to facilitate the on-board software usually a desired PWM level is computed by the ADCS and passed on to the panels for activation. In order to allow for accurate magnetometer readings a

single interrupt driven command was implemented that ceases any control activities of the torquers which later can be resumed on another command.

The magnetic moment computed in Eq. (4.2) potentially may saturate the magnetic actuators of the satellite which can result in unintended torques. Therefore, the demanded magnetic moment needs to be scaled to the maximal moment available to the ADCS.

4.1.2 Magnetic Moment Scaling

In order to ensure the correct application of the demanded magnetic moment the desired moment needs to be matched with the available strength of the magnetorquers. There are different ways to apply the scaling of the desired magnetic moment in order to find the output control moment $\mathbf{m}_{ctr}$:

1. Cut-off
2. Normalization
3. Heading-conserving scaling

The simplest and most forward technique to apply the magnetic moment is to cut-off the demanded magnetic moment at a given maximal moment per axis m_0.

$$\mathbf{m}_{\text{cut-off}} = \sum_{i=1}^{3} \operatorname{sgn}\left(\mathbf{m}_{ctr,i}\right) m_0 \mathbf{e}_i, \tag{4.3}$$

where $\mathbf{e}_i$ is the unit vector in the i-th coordinate and $\operatorname{sgn}()$ is the signum function.

If not paired with applying a PWM on the magnetorquer output this technique resembles an axis-wise bang-bang control actuation which results in a maximal applied magnetic moment. However, this output is not necessarily co-aligned with the demanded moment computed by Eq. (4.2). Therefore, any control activity will in general also create a disturbance which in turn decreases the efficiency of the magnetic control and increases the control error.

Normalization of the demanded control moment scales $\mathbf{m}_{ctr}$ to the maximal applicable moment m_0 and applies this moment:

$$\mathbf{m}_{\text{normalization}} = \frac{m_0}{|\mathbf{m}_{ctr}|}\mathbf{m}_{ctr} \tag{4.4}$$

The control moment is therefore always saturated in one axis but remains co-aligned with the demanded control moment $\mathbf{m}_{ctr}$. In cases where only a very small control moment is desired this routine will anyways apply the full strength of the magnetorquers resulting in

an over-actuation. Depending on the update rate of the controller this may increase the control error although magnetic control is a very slow actuation. However, it certainly increases the power consumption of a given attitude controller and decreases its ability to reach a steady state.

The third option is a heading-conserving scaling that conserves the desired magnetic moment strength for small control moments. It is implemented as expressed in Eq. (4.4) but only for control moments that exceed the satellite's available moment of each axis:

$$\mathbf{m}_{\text{hdg}} = \begin{cases} \frac{m_0}{|\mathbf{m}_{ctr}|}\mathbf{m}_{ctr} & \text{if } |\mathbf{m}_{ctr}| > m_0 \\ \mathbf{m}_{ctr} & \text{if } |\mathbf{m}_{ctr}| \leq m_0 \end{cases} \tag{4.5}$$

This routine especially requires PWM-controlled magnetorquer activation but, if properly implemented, achieves a precisely applied magnetic moment and is power efficient. However, the control law must be well designed and proportioned in order to demand a suitable control moment. Vanishing control moments that might be computed by the control law would not be corrected by the moment scaling procedure and, thus, the controller would be rendered inactive.

4.1.3 Residual Magnetic Dipole Compensation

First experiments to show the general health of the new software and that demonstrated the compensation of the satellite's residual moment through PWM controlled magnetorquer activation were performed on November 11$^{\text{th}}$ 2015. The high level controller was set not to interfere with the dipole compensation, thus, outputting a control torque $\mathbf{T}_c = [0,\ 0,\ 0]^T$ and the manual magnetic dipole was set to

$$\mathbf{M}_{man} = [0, -0.014, +0.045]^T \,\text{A}\,\text{m}^2. \tag{4.6}$$

Shown in Figure 4.2 are the torques acting on the satellite, where $\mathbf{T_e}$ is the torque experience by the satellite as derived from the gyroscopes, and $\mathbf{T_m} = \mu \times \mathbf{B}$ is a torque which can be explained by the magnetic interaction of the residual dipole moment μ and the Earth's magnetic field as measured by the satellite. These results have been obtained by applying the magnetic dipole analysis as introduced in Chapter 3.2. The numerical result for the compensation concludes that the residual dipole moment has been compensated to a remaining moment of

$$\mu_{\text{remaining}} = [+0.0010, +0.0018, -0.0044]\,\text{A}\,\text{m}^2. \tag{4.7}$$

This means, that the dipole compensation has successfully reduced the residual dipole moment to 8 % of its original value. It should be noted, that for this experiment the moment scaling routine ”Normalization” was activated such that the absolute norm of $\mathbf{M}_{man}$ was not kept precisely but the magnetic torquers were saturated in the satellite’s Z-axis.

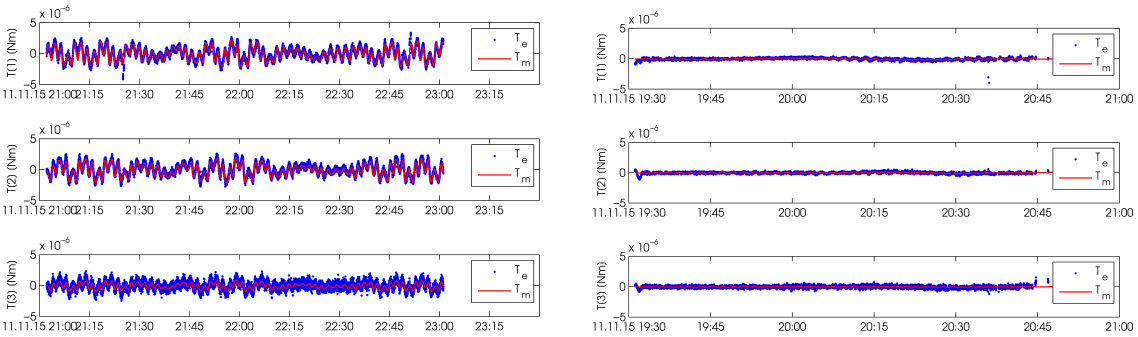

(a) Natural motion. **(b)** Active dipole compensation.

Figure 4.2: The static magnetic dipole compensation experiment performed on November 11$^{\text{th}}$ 2015. The satellite’s dynamical behavior in terms of torques acting on the satellite, where T_e (dotted, blue) is the experienced torque derived from the satellite’s gyroscopes and T_m (line, red) is the torque acting on the satellite due to a residual dipole. (Bangert et al., 2015a)

4.2 Detumbling

The release mechanism for traditional satellites that separates the satellite from the rocket’s upper stage is usually a customized design and ensures the correct separation. These satellites experience relatively small rotation rates after separation which then can be dumped by the attitude control system using reaction wheels or even small attitude control thrusters. However, for miniature satellites the ejection from the upper stage is less well defined as they are usually employing standard CubeSat containers that focus on the safe ejection rather than low initial tumbling of the satellites. Such containers, for UWE-3 it was a 3U ISIPOD from ISIS (ISIS - Innovative Solutions In Space, 2017), can store from single unit CubeSats to up to six units. In the case of the 3U ISIPOD the payload can be fractured, e.g. 2x1.5U, or 1U+2U, or 3x1U. The CubeSats are inserted into the container by which the spring-loading of the pusher plate is activated. The container is closed by the lid and is opened once in orbit by a command signal from the launch vehicle.

The example of SwissCube shows exemplary that CubeSats can experience very high rotation rates after ejection from their deployer. SwissCube was launched on board of a PSLV launcher on September 23$^{\text{rd}}$ 2009. Its health status was soon confirmed to be good

(a) ISIPOD

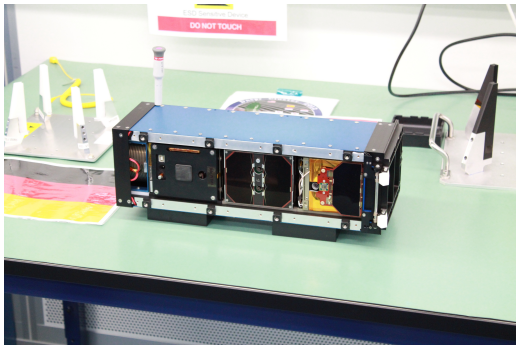

(b) VELOX-P2, UWE-3, and FIRST-MOVE in the 3U deployment container.

Figure 4.3: CubeSat deployment containers.

but it was discovered, that it was rotating at an angular speed of about 320 °/s for which the detumbling algorithm had not been designed (Noca and Ivanov, 2010). Due to the inherent time delay between commanding of a certain magnetic moment and the switching of the magnetorquers there is a certain phase delay between the two. If the satellite's rotation rate exceeds a certain limit, the phase delay can grow larger than 90 ° resulting in the contrary effect than intended. Due to the extraordinary high tumbling rate the SwissCube Team had to wait for the satellite to decrease its rotation rate by natural effects until the controller could be activated in February 2011 (Richard et al., 2011).

This example shows the significance of proper detumbling for small satellites especially from high spin rates. Not only the release from the upper stage bears the risk of high spin rates. In the case of UWE-3, where the attitude control of the satellite was the main technical experiment, high spin rates also occurred due to mistakes in the control algorithms and/or on-board software. When a new control software is tested in orbit rather than an elaborate testbed this is expected to happen. At least one case of such an issue resulted in a very high angular rate of about 108 °/s due to an unfinished execution of the attitude control experiment leaving the on-board controller in a state in which it constantly accelerated the satellite. All spin rates of UWE-3, however, were controlled and dumped within minutes after detumbling activation.

The first attitude control of UWE-3 was already performed on December 17th 2013 in terms of an initial detumbling after the analysis of its natural motion. The detumbling algorithm had been programmed into the ADCS and was tested before launch in the laboratory (Reichel, 2012; Reichel et al., 2013). The detumbling algorithm was implemented in form of a B-dot controller which tries to minimize the rate of change of the measured magnetic field **B**. After several software updates of the ADCS a new attitude control architecture was

implemented that was no further based on the B-dot controller and could also demonstrate its performance. The attitude control experiments with UWE-3 related to detumbling are presented in the following sections.

4.2.1 B-dot

In general, B-Dot control laws command a magnetic moment for each body axis, whose sign is opposite to that of the rate of change of the magnetic field measured in that axis. Thus, the generated torque is decreasing the rotational energy of the system. The most common B-Dot controller is a proportional $\dot{B}$ control law, as described in Flatley et al. (1997), with a magnetic control moment of

$$m_{ctrl} = -K\dot{\mathbf{B}}, \tag{4.8}$$

where K is a positive gain factor and $\dot{\mathbf{B}}$ is the rate of change of the measured magnetic field.

The algorithm implemented on board of UWE-3 made use of the distributed satellite architecture such that the switching of the torquers was not directly commanded by the ADCS but by the panels. For this, the actual measured magnetic field and current angular rate was transmitted to the panels which then propagate the magnetic field and switch their coils accordingly. This has the benefit that less frequent magnetic field measurements need to be taken and a faster switching frequency of the torquers can be achieved. In this respect, for re-synchronization at given intervals the panels switch off the torquers independently such that the ADCS can update the measurements. However, this loosely coupled mechanism was not entirely correctly implemented before launch such that at the beginning only duty cycles of maximal 10% were possible in order to ensure correct measurements of the ADCS. Furthermore, the initial detumbling was heavily disturbed by stalls of the I^2C-bus which occurred during the first weeks of operation. This resulted in an activation of the magnetic torquers of only 7 times one minute during the one orbit (97 minutes) of enabled detumbling mode.

With the first software update of the ADCS these issues were resolved and an undisturbed detumbling from a high spin rate could be demonstrated on July 17$^{\text{th}}$ 2014 (Busch et al., 2014a). The satellite had a very high initial spin rate of almost 80 °/s which enabled to prove several performance characteristics of the ADCS such as attitude determination at high spin rates and detumbling from the same.

The maneuver was commenced at 07:56:54 UTC at an initial tumbling rate of

$$\begin{aligned} \omega &= [71.90, -5.32, -29.21]\,^\circ/\mathrm{s} \\ |\omega| &= 77.78^\circ/\mathrm{s} \end{aligned}$$

and a stable attitude was established in about 40 minutes as can be seen in Figure 4.4. Shown in Figure 4.5 is the corresponding 3-D representation of the rotation rate vector where the precession motion is also clearly visible. This maneuver could prove that the ADCS is capable of slowing down the satellite even at very high spin rates. Furthermore, the algorithm stabilized the satellite with an RMS of $0.7353\,^\circ/\mathrm{s}$ about zero and $[0.3968, 0.4953, 0.3714]\,^\circ/\mathrm{s}$ in x, y, z-components respectively.

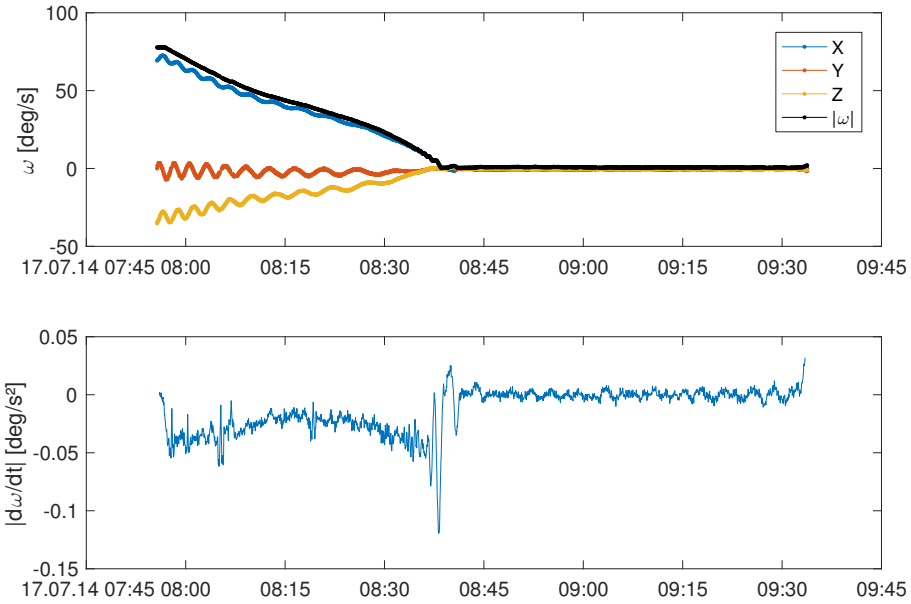

Figure 4.4: Angular rate measurements during detumbling maneuver on 17th 2014 and corresponding angular acceleration.

The magnetorquers decelerate the angular rate with up to $0.05\,^\circ/\mathrm{s}^2$ as shown in Figure 4.4. The angular rate data and the magnetic field measurements can be used to calculate the control torque exerted by the attitude controller. The control torque $\mathbf{T}_c$ then is given as

$$\mathbf{T}_c = I\dot{\omega} + \omega \times (I\omega) - \mu_{residual} \times \mathbf{B}, \tag{4.9}$$

where the influence of the residual magnetic dipole moment is already taken into account. The result of this analysis is shown in Figure 4.6. It is clearly visible that the controller acts on all three axes homogeneously. Once the controller has reached a minimal remaining rotation rate (at around 08:38 UTC, $|\omega| = 0.16\,^\circ/\mathrm{s}$) it continues to counteract the residual

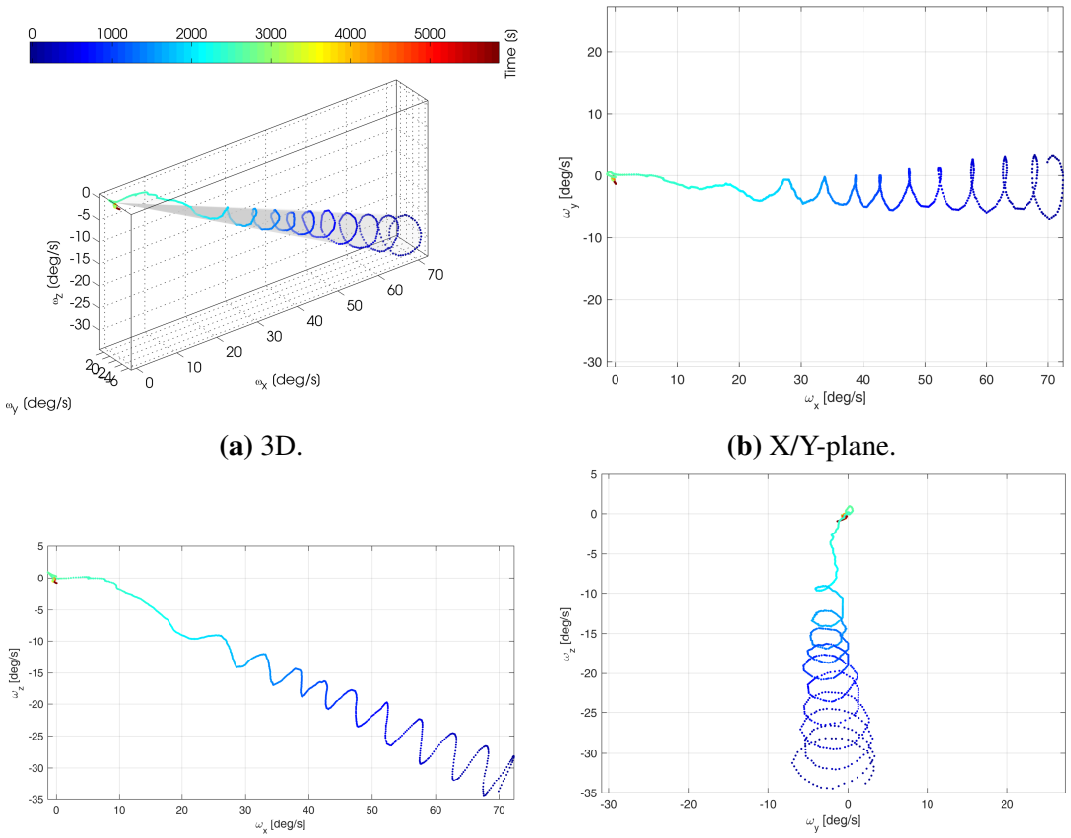

(a) 3D.

(b) X/Y-plane.

(c) X/Z-plane.

(d) Y/Z-plane.

Figure 4.5: Angular rate vector during detumbling maneuver on July 17th 2014.

magnetic moment in order to stabilize the satellite. The controller was switched off at 09:33 UTC which is indicated by the sharp decline of the control torque at the end of the recording.

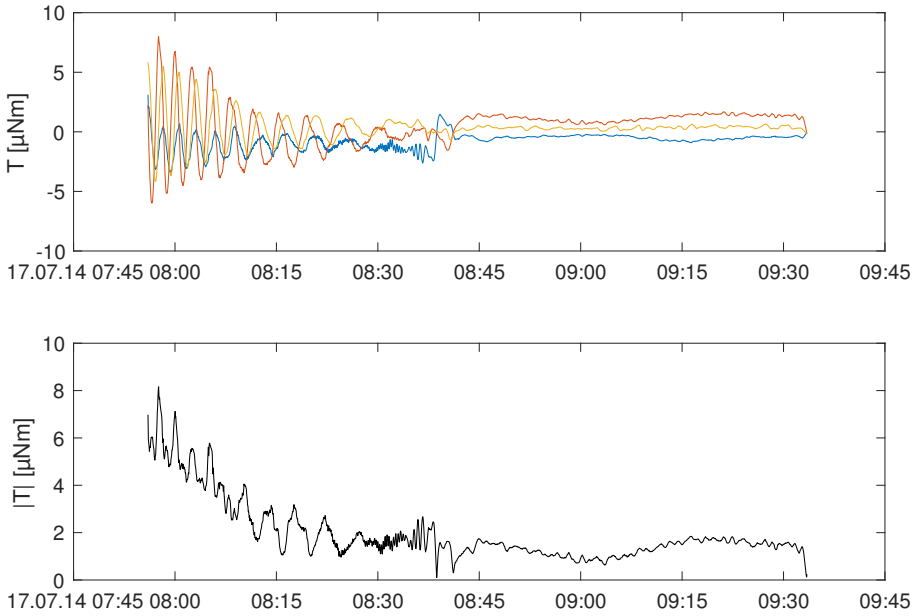

Figure 4.6: Control torque during detumbling maneuver on July 17$^{\text{th}}$ 2014.

4.2.2 Rate Control

With the sequential software updates of the ADCS up to the beginning of 2016 a new attitude control architecture was introduced as described in Chapter 4.1.1 that focuses on the control of the satellite's angular rate. The performance of this controller with respect to detumbling the satellite could be demonstrated during two attitude control maneuver experiments in 2016. The first one, recorded on January 26$^{\text{th}}$ 2016, targeted a complete stabilization of the satellite with the feed-forward residual dipole compensation enabled while the second, recorded on April 19$^{\text{th}}$ 2016, had a spin-axis control as goal.

On January 26$^{\text{th}}$ 2016 the initial angular speed was about 20 $^\circ/$s and could be damped in about 30 minutes as shown in Figure 4.7. However, after a fast angular speed decay to about 2 $^\circ/$s the controller was not able to proceed to decelerate the rotation in the same manner. In fact, the rotation rate about the satellite's Z-axis only slowly decreases further to 1.7 $^\circ/$s within the next two hours.

A look at the magnetic field measurement recording shows that the satellite at that time had aligned its positive Z-axis with the Earth's magnetic field whereas the magnetic field readings about X and Y were close to zero. Two conclusions could be drawn from

that: first, the torquers were able to overcome the residual magnetic dipole even such that they align the satellite with the magnetic field opposite to its natural alignment. The second lesson learned by this experiment was that care has to be taken in order to avoid the alignment of the remaining angular rate vector with the Earth magnetic field. In Figure 4.8 the angle between the angular rate vector and the magnetic field as well as the excited control torque is shown. When this angle approaches zero (i.e. after 20:00 UTC) the controller is unable to create the necessary torque in order to decrease the rate about the Z-axis.

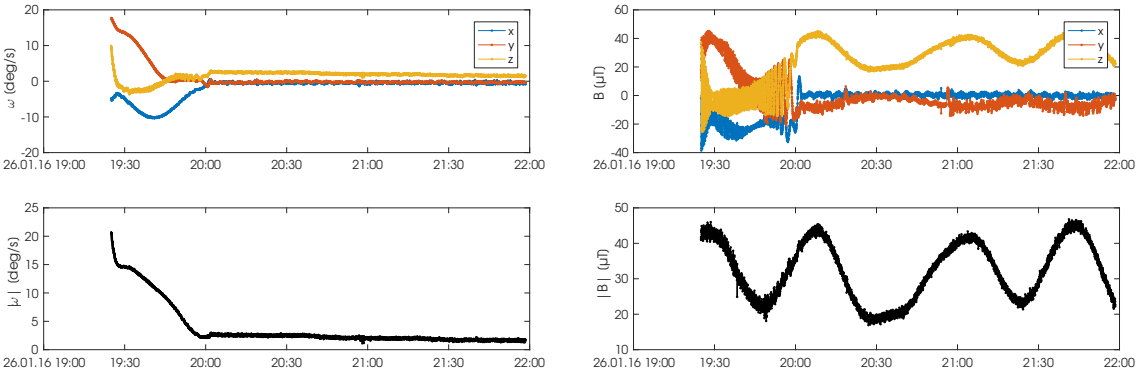

Figure 4.7: Angular rate and magnetic field recording during rate control experiment on January 26th 2016.

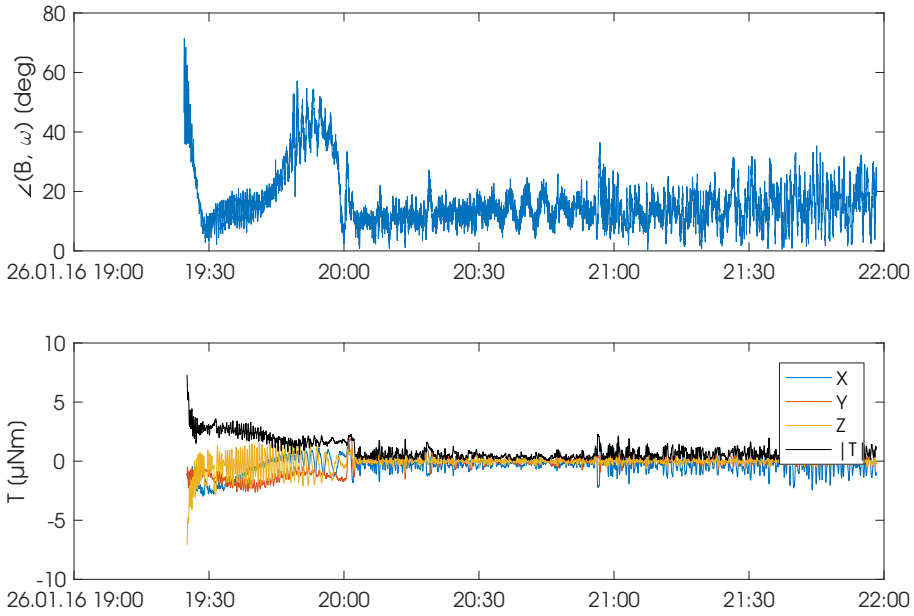

Figure 4.8: Angle between the angular rate vector and the magnetic field, and the excited control torque during rate control experiment on January 26th 2016.

The initial rotation rate of the control experiment on April 19th 2016 was with 108 °/s

the highest angular speed achieved with UWE-3 and could be damped within an hour to the intended spin rate of 15 °/s as shown in Figure 4.9. The set-point of the rate controller was [15, 0, 0]°/s (indicated with dashed lines) which is held after detumbling for several hours. The performance during the spin-axis control is subject in Section 4.3.2.

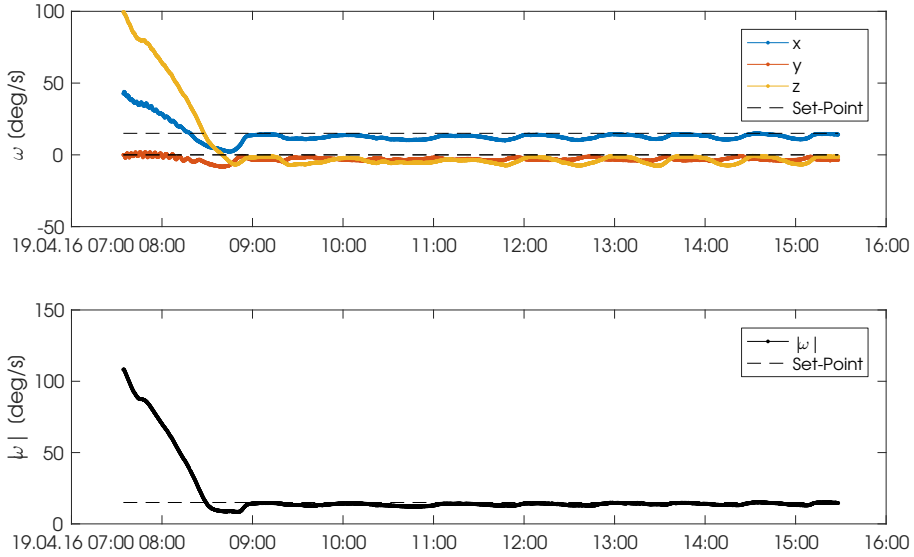

Figure 4.9: Angular rate during a rate control experiment on April 19th 2016.

4.3 Spin-Stabilized Control

Having proven the ability of the attitude control system to damp even very high spin rates of the satellite and after simulations showed that a successful three-axis pointing control with UWE-3 remains improbable due to the satellite's residual magnetic dipole moment, the attitude control goal was shifted towards spin-axis control. This control scheme aims at aligning one satellite body axis with a given vector in inertial space. In order to achieve a stable inertial one-axis pointing the satellite is spun up about this axis and its gyroscopic stiffness makes it less susceptible to external disturbance torques.

The achievement of this goal would mark an important step towards purely magnetically controlled miniature satellites and has special importance for the UWE-4 mission since it would enable orbit control maneuvers at certain points in the orbit where the thrust axis is spin-stabilized and pointed towards the intended inertial/orbit frame direction. Such maneuvers could for instance be used for control of the semi-major axis with the objective to lower the orbit and eventually accelerate de-orbiting of the satellite. One way to do this is to lower the perigee of the orbit in order for the satellite to experience more atmospheric drag at perigee and therefore to de-orbit faster. This would require thrust in anti-in-track

direction at apogee which is previously known to the controller and could therefore already be acquired by an attitude control algorithm that aligns the thrust axis before reaching apogee.

In order to work towards this attitude controller several smaller steps have been taken during active operation of UWE-3. Starting off from a controller that targets a certain spin rate about the satellite's Z-axis the Tinytus architecture was employed to try out other spin-axis control types.

4.3.1 Spin-Z Control

One of the originally implemented controllers of UWE-3 was the so called Spin-Z controller. Its goal is to achieve a stable spin about the satellite's Z-axis while minimizing the angular speed about the other two axes. However, no alignment of the spin axis is part of the control law. The controller directly commands a certain control moment $m_{control}$ that is computed based on the desired spin rate ω_d, the currently measured magnetic field $\mathbf{B}$, and a gain factor K:

$$\mathbf{m} \equiv m_{control} = -K\left(\dot{\mathbf{B}} + \omega_d \times \mathbf{B}\right). \tag{4.10}$$

The first of such control experiments was performed on July 25$^{\text{th}}$ 2014, where no updates of the ADCS software had been uploaded, yet. The experiment was set up to demonstrate spin-up of the satellite's Z-axis to $10\,^\circ/\text{s}$ with the gain set to one. Shown in Figure 4.10 is the angular rate measurements taken by the ADCS during the spin-up. Unfortunately, due to software issues in this early implementation the recording stops after only six minutes. However, the attitude controller had already established the desired spin rate after about 4 minutes. The magnetic spin controller does not take the residual dipole moment into account and its effects can be seen in Figure 4.11. The disturbance torque, reconstructed from the magnetic field measurements, periodically disturbs predominantly the X- and Y-axis which is not fully counteracted by the controller. Therefore, small oscillations of the angular rate can be seen that are directly due to the residual dipole moment.

Due to the erroneous software controlled torquer/measurement sequence in this early phase of operations there are sharp changes in the determined disturbance torque. These are due to magnetic field measurements picking up the magnetic field produced by the magnetorquers.

On July 31$^{\text{st}}$ 2014 the controller was commanded to an angular speed of $\omega_d = -10\,^\circ/\text{s}$ about the Z-axis during the day. Due to the problems with the experiment recording this data could not be sampled during the day. But when the satellite passed over the Würzburg

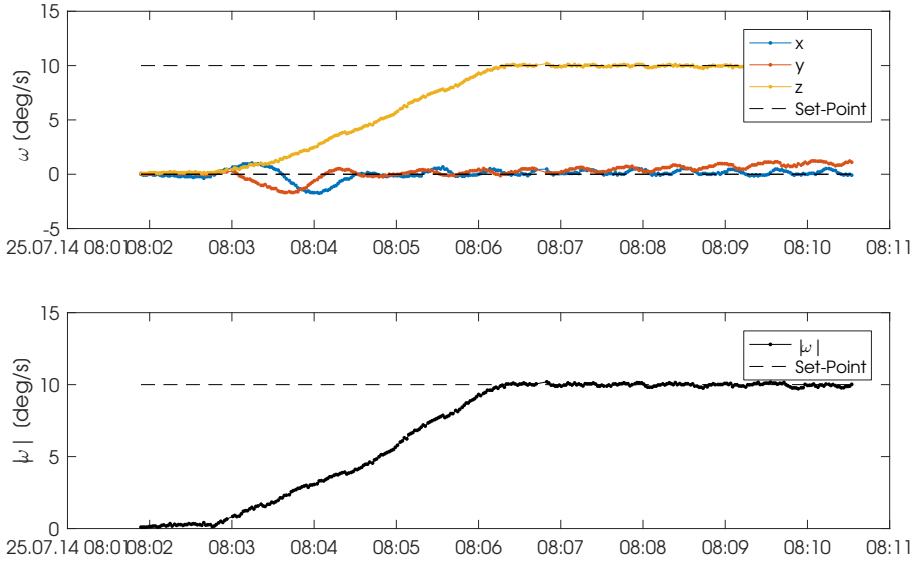

Figure 4.10: Angular rate during Spin-Z control experiment on July 25th 2014. Due to software issues the recording stopped after about six minutes.

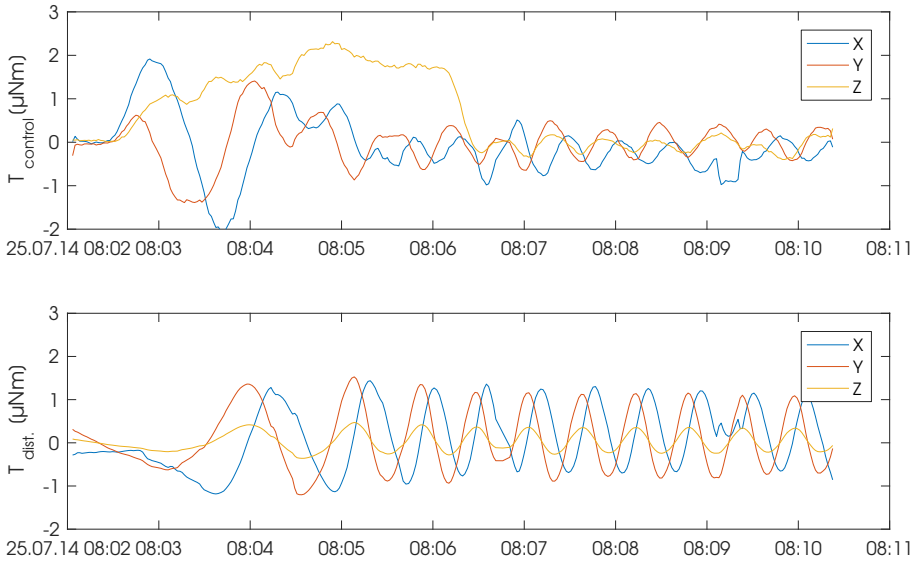

Figure 4.11: Torques acting on the satellite during magnetic spin control. This controller does not take the magnetic disturbance into account.

Groundstation at about 19:45 UTC the telemetry showed that in fact it had precisely acquired the desired spin rate:

```
< 31 Jul 2014 19:48:51 GMT: Measurement
GYRO
Timestamp = 40921135
Angular Rate (x,y,z) [deg/s] = [0.20626,  0,  -9.9924]
Angular Speed = 9.9973 deg/s
Temperatures (x,y,z) [°C] = [-6.82, -8.85, -9.58]
```

It was decided to flip the rotation axis from $-10\,°/s$ to $10\,°/s$ (at 19:52:33 UTC) which was kept active for one orbit at which point (21:24:50 UTC) the spin rate was set to $-5\,°/s$. The angular rate recording is shown in Figure 4.12 where the different controller set-points are indicated by dashed lines. It is clearly visible that the rotation about the satellite's Z-axis is well controlled and within minutes at the intended rate. It is kept at this rate throughout the orbit. However, there are two points in the orbit where the Y-axis rate deviates significantly from its zero-set-point while the angular speed remains constant at $10\,°/s$.

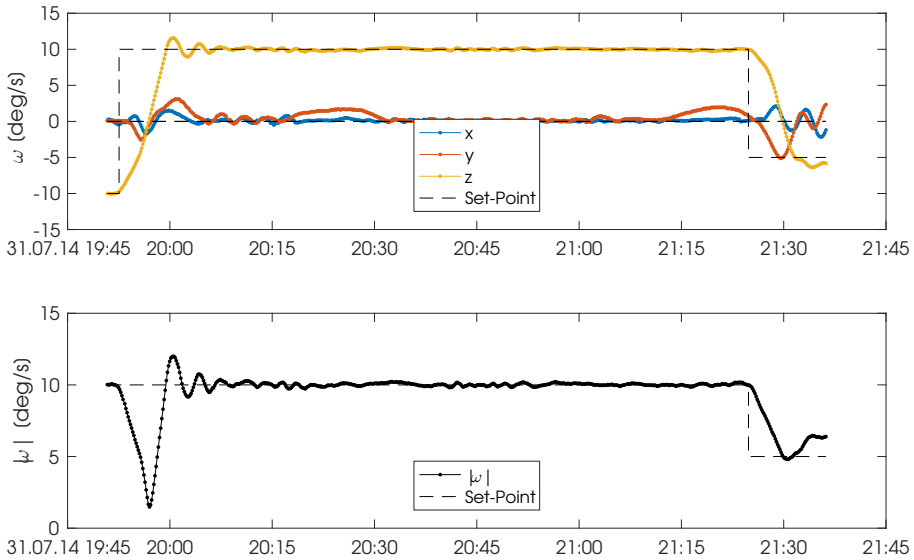

Figure 4.12: Angular rate during Spin-Z control experiment on July 31st 2014. The initial spin rate about the Z-axis was held to $-10\,°/s$ from a previously configured Spin-Z experiment when the controller was re-configured to $10\,°/s$ at 19:52 UTC as indicated by the dashed lines.

This is more clearly shown in Figure 4.13 where the angle between the satellite's body Z-axis and the spin axis is plotted. The dashed lines indicate the start and stop of the $10\,°/s$

experiment run for which the analysis is made. One can see, that the spin axis aligns well with the body Z-axis during most parts of the orbit. However, during two periods (20:15 - 20:30 and 21:10 - 21:25) the rotational speed about the Y-axis increases significantly, moving the spin-axis alignment about 10 ° away from its intended body direction. As seen in Figure 4.12 this does not translate into a change of the overall angular speed of the satellite, which indicates that it is in fact due to an exchange of angular momentum between the two axes.

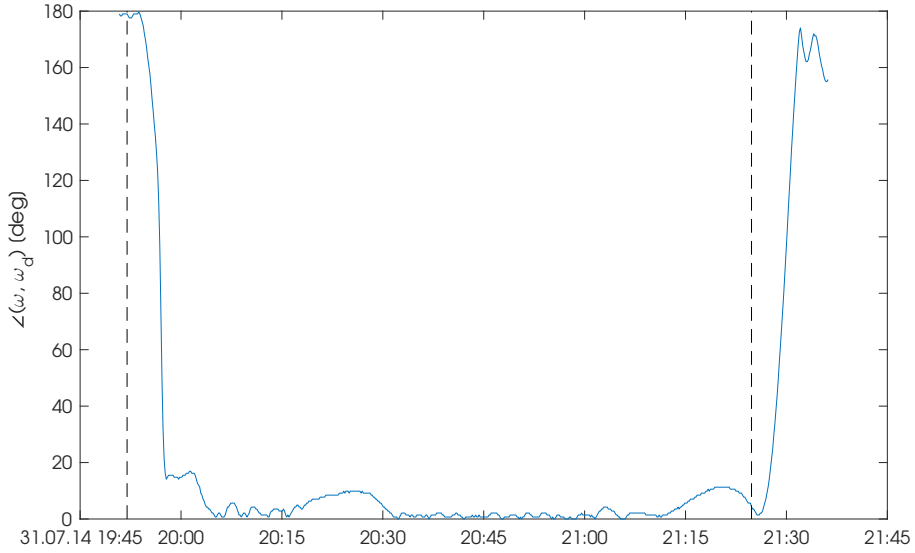

Figure 4.13: Angle between actual spin axis and intended Spin-Z on July 31st 2014. Between the dashed lines the controller was set to 10 °/s and the spin axis is well aligned with the satellite's body Z-axis. However, during two periods (20:15 - 20:30 and 21:10 - 21:25) the angle between the body Z-axis and the actual spin rate increases to about 10 °.

A different experiment recorded on July 29th 2014 shows the deviation of the spin axis from its intended Z-direction even more clearly. The control experiment lasted for about four hours during which the Spin-Z controller was set to 10 °/s. In Figure 4.14a the angular rate is shown while in Figure 4.14b the angle between the actual spin-axis and the body Z-axis is plotted as well as the Z-component of the magnetic field vector measurements. It can be seen that the spin-axis significantly deviates from the Z-axis at points in the orbit where the magnetic field in the Z-direction is very weak. These regions are indicated by red patches and coincide due to the satellite's orientation with regions in the orbit where the overall magnetic field strength is weak.

The analysis of the different torques acting on the satellite during this experiment shows that the precession torque $\mathbf{T}_{prec}$ is in this configuration significantly acting on the Y-axis of

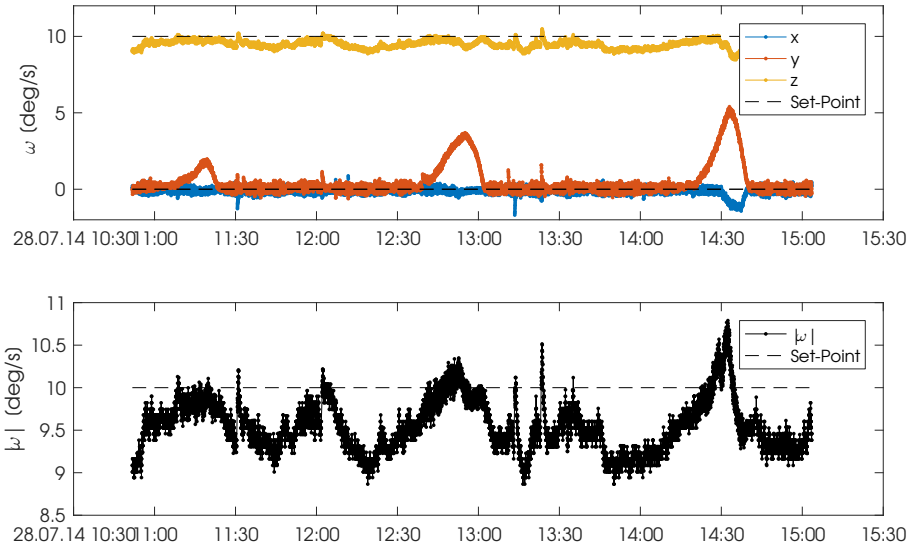

(a) Angular rate.

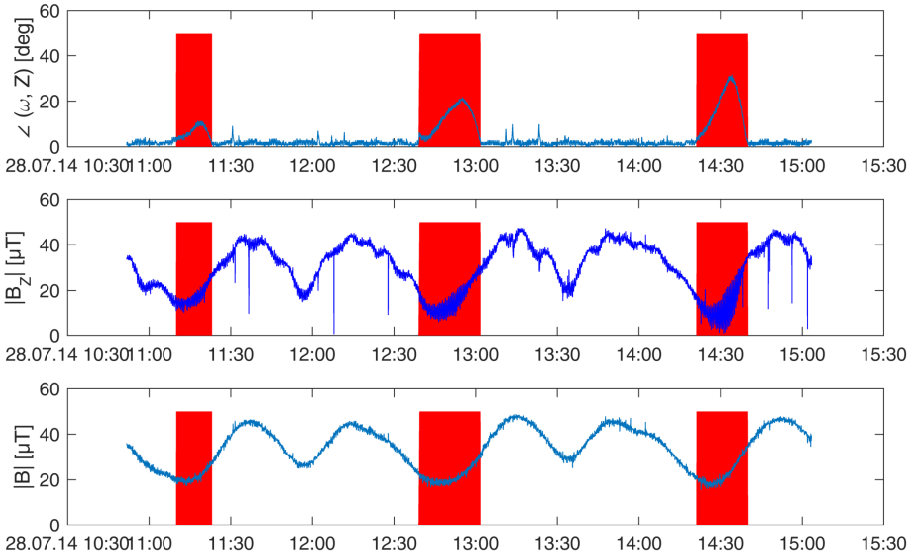

(b) Angle between actual spin axis and body Z-axis as well as the Z-component of the magnetic field vector measurements. The red regions indicate the three occurrences where the spin axis significantly deviates from the body Z-axis.

Figure 4.14: Spin-Z control experiment on July 29th 2014.

the satellite:

$$I\dot{\omega} = \mu \times \mathbf{B} - \mathbf{T}_{prec} + \mathbf{T}_c = \mu \times \mathbf{B} - \underbrace{\omega \times (I\omega)}_{\mathbf{T}_{prec}} + \underbrace{\mathbf{m} \times \mathbf{B}}_{\mathbf{T}_c}. \tag{4.11}$$

The precession torque is shown in Figure 4.15a and it can clearly be seen that due to the inertia tensor and spin axis the main load during steady state is on the Y-axis with a mean torque component of 0.65 µN m. Both X- and Z-axes experience during stable rotation no significant precession torque (0.05 µN m and 0 µN m, respectively). In Figure 4.15b the complete right hand side of Eq. (4.11) is shown. In this plot, the spin-disturbing torques $\mathbf{T}_\mu$ and $\mathbf{T}_{prec}$ are combined and compared to the theoretically maximal control torque that could be excited by the torquers. It becomes visible, that within the red regions the disturbing torque especially in the satellite's Y-axis comes close to the maximal control torque and even exceeds this.

These findings further motivated the implementation of a generic spin-controller that is able to use any arbitrary axis within the satellite as its spin-axis. The necessary software updates of the ADCS were performed only in late 2015 after which the following attitude control experiments became possible.

4.3.2 Spin-Axis Control

Using the newly implemented control architecture as presented in Chapter 4.1.1, the arbitrary spin control law is easily implemented in Tinytus:

$$\dot{\omega}_d = K\left(\omega_d - \omega\right), \tag{4.12}$$

where $\dot{\omega}_d$ is the desired angular acceleration given to the underlying controller, K is the gain, ω_d is the desired angular rate, and ω is the currently measured angular rate.

There have been different control experiments performed with UWE-3 in Spring 2016 which will be analyzed in the following sections.

4.3.2.1 Spin-X Control

The control experiment performed on April 20$^{\text{th}}$ 2016 has already been mentioned before in Chapter 4.2.2. It was following a large angular speed dumping which itself was performed on April 19$^{\text{th}}$ 2016 and is shown in Figure 4.9 where also the immediate spin control about the satellite's body X axis is shown. However, on April 20$^{\text{th}}$ this was further refined and the satellite's angular rate over the course of the 8 hours of recording is shown in Figure 4.16

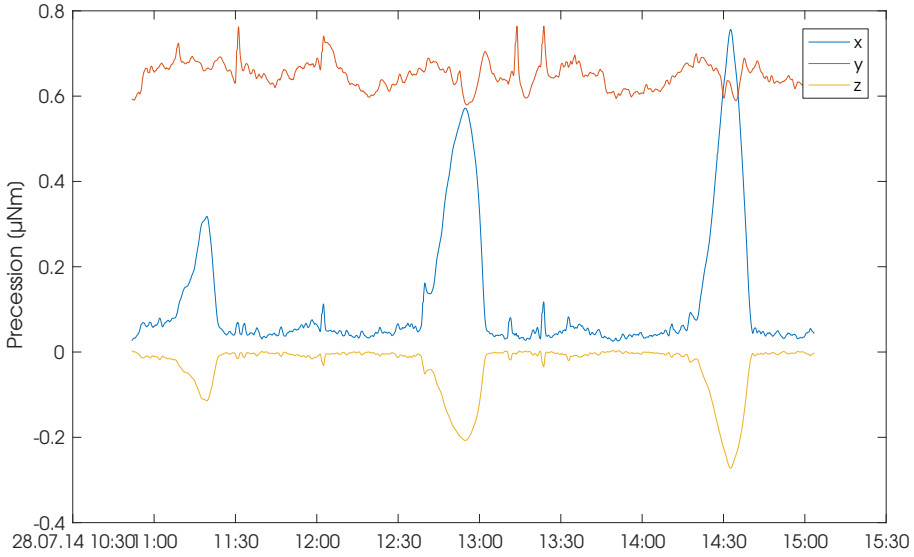

(a) Negative precession torque: $-\omega \times (I\omega)$.

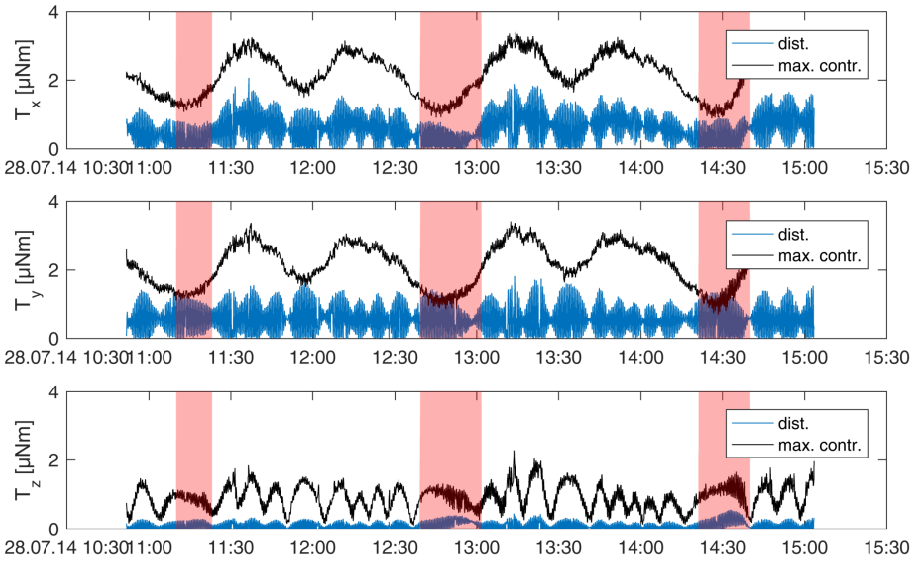

(b) Spin-disturbing torques together with the theoretically max. achievable control torque with the UWE-3 torquers.

Figure 4.15: Torque analysis of the spin-Z control experiment on July 29th 2014.

together with its spin axis off-pointing. The desired spin axis of $\omega_d = [10,\ 0,\ 0]\,^\circ/\mathrm{s}$ was established after about 40 minutes. However, it is obvious that the controller was not able to retain the spin axis correctly but there are two effects visible in the data:

1. a constant offset in the satellite's Y-axis spin rate to about $-1.7\,^\circ/\mathrm{s}$ resulting in an off-pointing of about $9\,^\circ$ during well-controlled periods, and

2. periods of typically about 20 minutes within the orbit, where the spin axis significantly deviates from the desired spin axis but then quickly returns to the set-point.

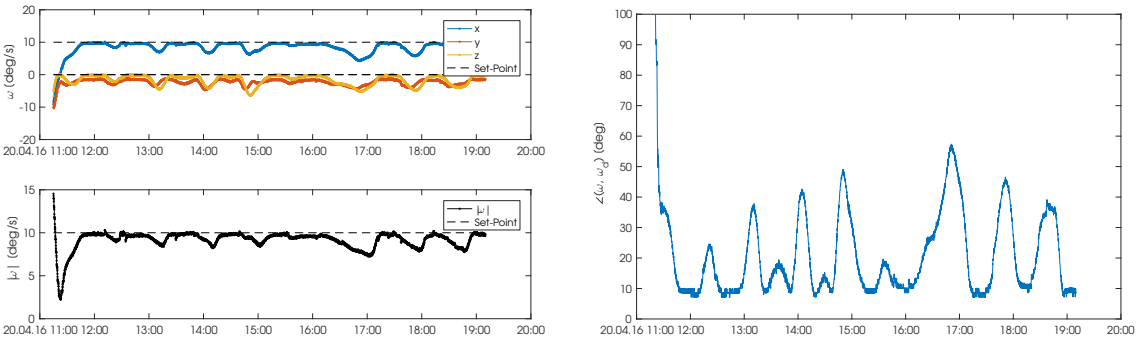

(a) Angular rate. **(b)** Spin-axis pointing.

Figure 4.16: Angular rate data from Spin-X control experiment using Tinytus on April 20th 2016.

In order to analyze the origin of these two observations the on-board calculated control torque $\mathbf{T}_c$ has been recorded and is compared against the actually measured control torque derived from the satellite's gyroscope and magnetometer readings in Figure 4.17a. Generally speaking the measured torque coincides well with the commanded torque proving the correct implementation of the underlying generic control law. Small deviations can be seen in the magnitude of the torque, corresponding to a slightly too high gain factor K. But foremost it can be seen, that during some periods the satellite is subject to torques (especially visible on the body Y-axis) while the controller does not command any torque in this direction. Such an event is clearly visible at time 13:35 UTC and 14:30 UTC but an underlying constant off-pointing of the created torque relative to the commanded torque becomes visible when plotting their angular displacement as shown in Figure 4.17b.

4.3.2.2 Spin-Control About Principle Axis

One of the last in-orbit performed control experiments was a spin-control about the satellite's largest principle axis. The inertia tensor as found in Eq. (3.39) has the diagonal

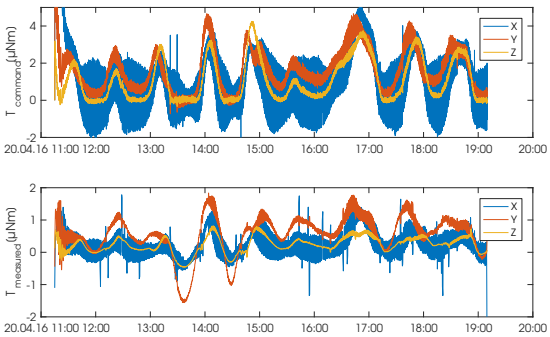

(a) Commanded torque $\mathbf{T}_c$ and the actually measured torque.

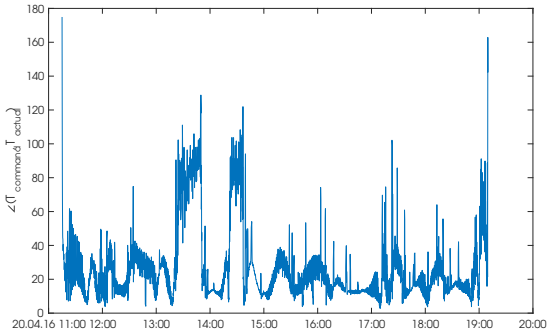

(b) Angular displacement between the commanded torque and the actually measured torque.

Figure 4.17: Torque analysis of the Spin-X control experiment using Tinytus on April 20th 2016.

form

$$I_{diag} = \begin{bmatrix} 1.9715 \cdot 10^{-3} & 0 & 0 \\ 0 & 2.0324 \cdot 10^{-3} & 0 \\ 0 & 0 & 2.0463 \cdot 10^{-3} \end{bmatrix} \mathrm{kg\,m^2} \tag{4.13}$$

with its eigenvectors

$$\mathbf{e}_1 = \begin{bmatrix} 0.36478 \\ -0.06029 \\ 0.92914 \end{bmatrix}, \quad \mathbf{e}_2 = \begin{bmatrix} -0.4831 \\ 0.84081 \\ 0.24422 \end{bmatrix}, \quad \mathbf{e}_3 = \begin{bmatrix} -0.79596 \\ -0.53796 \\ 0.27758 \end{bmatrix}, \tag{4.14}$$

with $\mathbf{e}_3$ being the eigenvector to the largest eigenvalue and about which stability can be achieved.

The axis was chosen to be

$$\omega_d = \begin{bmatrix} -1.624 \\ -1.070 \\ 0.464 \end{bmatrix} {}^\circ/\mathrm{s}. \tag{4.15}$$

corresponding to a rotational speed of $|\omega_d| = 2\,^\circ/\mathrm{s}$. Compared to the moment of inertia given in Eq. (3.37) this axis represents the largest principle axis to about 2.75 ° precision. The controller was active for 8 hours and achieved a mean deviation from the desired spin axis of 1.58 °.

The corresponding angular rate data is shown in Figure 4.18. Shown in Figure 4.19a is

a 3D representation of the measured angular rate and the desired spin axis as well as the measured angular off-pointing of the spin axis. The distribution in Figure 4.19b is centered at 9.23 ° with a standard deviation of 3.98 °. However, the off-pointing distribution includes the gyroscopes' sensor noise and therefore does not represent absolute pointing. Despite the angular displacement, the controller is able to retain the satellite's spin axis very close the the desired spin rates: the mean deviation from the desired spin rate in X, Y, and Z axis is only

$$\overline{(\omega_d - \omega)} = [0.25, \quad 0.15, \quad -0.11]\,°/\mathrm{s}, \tag{4.16}$$

respectively as shown in Figure 4.18b.

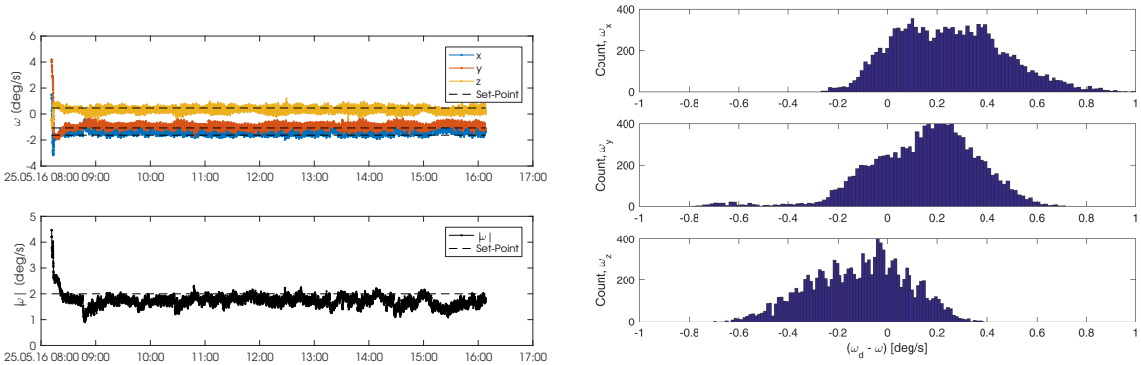

(a) Angular rate. **(b)** Distribution of the angular rate error.

Figure 4.18: Angular rate and rate error during principle axis spin control experiment using Tinytus on May 25th 2016.

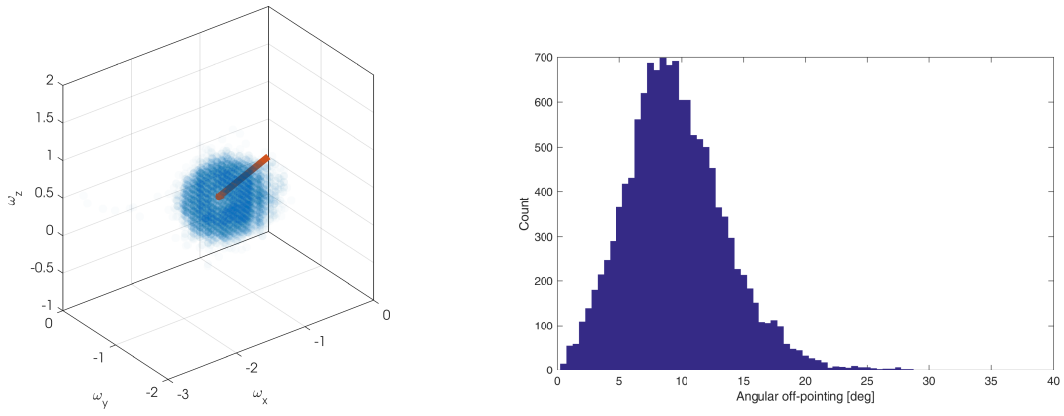

(a) Measured angular rate vectors (blue, transparent) and the desired angular rate vector ω_d. **(b)** Spin-axis off-pointing histogram.

Figure 4.19: Angular rate vector pointing during principle axis spin control experiment using Tinytus on May 25th 2016.

4.4 Summary

This chapter has presented the implementation of a flexible modular attitude control architecture and its application in the UWE-3 mission.

The architecture divides attitude control into different layers, each being optimized for a specific task. The highest level of control, the objective control, is implemented in terms of efficient Tinytus scripts that are easily exchanged in orbit allowing tests of a multitude of control laws. The second level is a generic controller that translates angular acceleration commands issued by the objective controller into a necessary control torque. It takes into account all known influences on the satellite's dynamics and efficiently counteract for instance the residual dipole moment. This is done by computing the disturbance's impact on the satellite's dynamics rather than statically canceling the magnetic moment. Therefore, energy to counteract the residual dipole moment is only required when the latter actually acts as an unwanted disturbance. The last layer drives the attitude control actuators and determines which part of the required control torque can be applied by which actuator. According to this, the control torque is then provided by the set of actuators available to the satellite.

The in-orbit application of this control architecture has been shown with the UWE-3 satellite. The magnetic attitude control experiments presented here focused on detumbling and spin-stabilized control. Detumbling of the satellite was successfully demonstrated several times in orbit. During the experiments a record of decelerating the satellite's angular rates from $108\,^\circ/\mathrm{s}$ to an intended spin rate of $15\,^\circ/\mathrm{s}$ within an hour was achieved.

It was demonstrated to spin the satellite at various spin-rates and through various axes. However, due to the almost homogenous inertia tensor of a 1U CubeSat a clean and stable rotation about a single axis has proven to be difficult. It was shown that at large spin-rates the precession of the satellite's spin-axis cannot be counteracted by the magnetic actuators during certain parts of the orbit at which the magnetic field lies in an unfavorable axis. This has motivated experiments to spin about the principle axis of the satellite which was successfully performed for several orbits and with a mean deviation of less than $0.25\,^\circ/\mathrm{s}$ per axis.

The attitude control experiments with UWE-3 demonstrated the difficulties of magnetic attitude control especially under the influence of a large disturbance torque. However, the focus on axis/spin-pointing controllers also prepared the necessary ground for thrust vector control for future satellite missions. The control architecture and algorithms developed here are being further utilized in the UWE-4 mission which is addressed in the following chapter.

5

Attitude and Orbit Control Using Magnetic and Electric Actuators

Increasing mission requirements for precise attitude pointing have been a major driver towards larger nano-satellite platforms over the recent years. Nevertheless, pico-satellites still promise interesting application potential for a variety of mission concepts and an increase in their performance while adhering to the specific size and power constraints will even broaden their utilization. Precise attitude and orbit control is a key technology still to be incorporated in the pico-satellite class due to its typical size and power constraints. The University Wuerzburg Experimental Satellite 4 (UWE-4) strives to demonstrate a hybrid attitude and orbit control using magnetic torquers and an electric propulsion system in the 1U CubeSat class. Four NanoFEEP thrusters, developed at TU Dresden, are integrated into the corners of the CubeSat in order to provide precise thrust-vector pointing in combination with the magnetic attitude control system. Achievable orbit control capabilities comprise orbit lifetime reduction (de-orbiting), very Low-Earth-Orbit maintenance, and even formation control while providing pointing control for potential future payloads.

UWE-4 will be the first satellite to use the NanoFEEP propulsion system. Thus, the characterization of the thrusters in orbit is the main mission objective. The low thrust levels of the electric propulsion system are difficult to measure precisely via their impact on the actual satellite's orbit. However, the precise estimation of small disturbances, demonstrated with the magnetic dipole moment of UWE-3 in Chapter 3, can be used in order to measure even very low thrust levels in the order of a few μN.

The attitude control architecture introduced in the previous chapter is used to split the control torque between different attitude control actuators. UWE-4 will demonstrate a hybrid attitude and orbit control system based on the control architecture in order to provide precise thrust vector pointing for orbit control maneuvers.

This chapter presents the UWE-4 satellite design related to the integration of the electric propulsion system and the attitude control system and elaborates on the operations concept in order to fulfill the mission objectives. The algorithm to characterize the propulsion system in orbit is presented in Chapter 5.2. The application potential of the propulsion system is presented in Chapter 5.3. The fusion of magnetic attitude control and the electric propulsion system resembles a hybrid attitude and orbit control that is further elaborated on in Chapter 5.4.

5.1 UWE-4: The next University Würzburg Experimental Satellite

The UWE-4 satellite project has been initiated in 2015 and is currently being prepared for launch in 2018. It follows the roadmap towards the formation flight of pico-satellites by providing orbit control capabilities for the first time within the UWE series. The project is funded by the German Aerospace Center DLR and serves both as an educational and technology demonstration mission. The satellite design is heavily based on the precursor UWE-3 and inherits most of its systems while implementing minor improvements upon them.

The technical objective of the UWE-4 mission is the in-orbit demonstration and characterization of an electric propulsion system for 1U CubeSats. For this, the project cooperates with the TU Dresden that develops the NanoFEEP propulsion system (Bock et al., 2014). This system fits the CubeSat's strict requirements in terms of size and power consumption, and has therefore been selected as the UWE-4 technical payload. The propulsion system consists of the thruster heads that are being integrated into the CubeSat rails and the power processing unit (PPU) that is realized as standard subsystem according to the UNISEC Europe standard (Busch, 2015). The primary technical mission objective is to activate the thrusters and to measure their thrust in different operating ranges. Secondary objectives include attitude control using the four thrusters and eventually to perform basic orbit control maneuvers.

5.1.1 Satellite Design

The UWE-4 satellite is based on the architecture introduced in UWE-3 and published by UNISEC Europe. It makes use of a backplane which interconnects all subsystems with a standardized interface and also interfaces the CubeSat's panels. This architecture supports rapid development, test, and integration of new subsystems. It provides several

redundant communication busses (I^2C, UART, and MLVDS) and power busses, dedicated synchronization signals, and complete debug access to each subsystem. The subsystem stack as shown in Figure 5.1 consists of the OBC, the Attitude and Orbit Control System (AOCS), two PPUs, the Electric Power Subsystem (EPS), the UHF Communication System (COM), and the Front Access Board (FAB).

In the following sections the subsystems related to attitude and orbit control are presented in order to provide an overview of the satellite's capabilities.

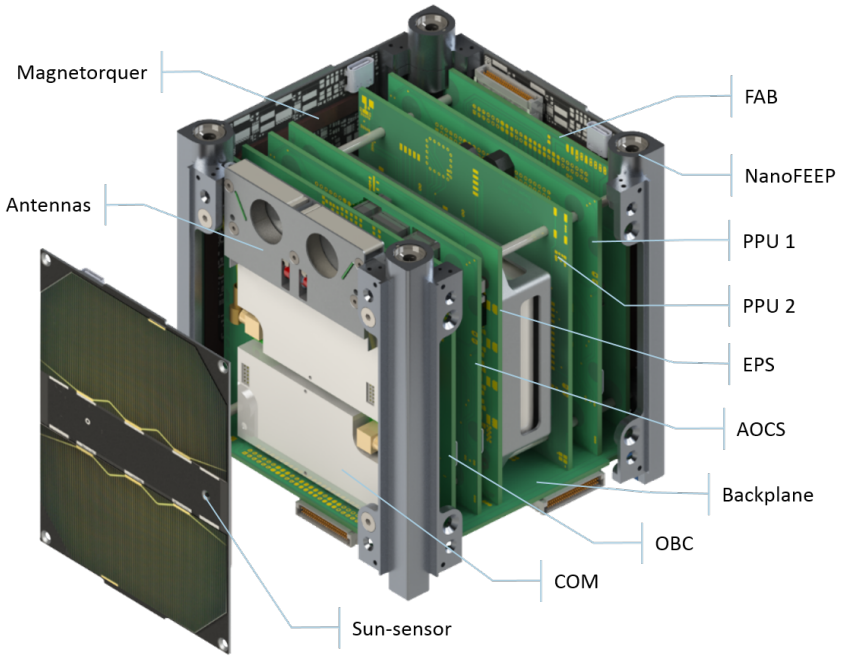

Figure 5.1: Satellite Design of UWE-4.

5.1.1.1 Electric Propulsion System

The electric propulsion system acts as the technical payload of the UWE-4 CubeSat. The NanoFEEP system currently in development at TU Dresden (Bock et al., 2014) was selected for its compatibility with the 1U size and power restrictions.

The NanoFEEP thruster is an electric propulsion system of the field emission electric propulsion (FEEP) type of which the working principle is illustrated in Figure 5.2a and which is further described in Tajmar et al. (2004) and Bock et al. (2015). The propellant of this class of thrusters is a liquid metal that is stored in a small compartment below a sharp needle. The metal usually is liquified by heating the fuel which then flows towards

the tip of the needle driven by capillary forces. A large static voltage between the needle and the extractor electrode creates a strong electric field that reaches its highest field strengths of more than $10^{10}\,\mathrm{V/m}$ directly at the tip of the needle. At these field strengths the metal propellant is ionized and accelerated by the same extractor electrode away from the spacecraft. The ion propellant can reach velocities of more than $100\,\mathrm{km/s}$ rendering this type of propulsion system very fuel efficient. A specific impulse (I_{sp}) of several thousands of seconds can be realized. However, only very small thrust levels on the order of some µN usually are achieved. Before being considered as main propulsion system for miniature spacecraft this class of propulsion systems was selected to be flown on the LISA mission as ultra-fine pointing actuator.

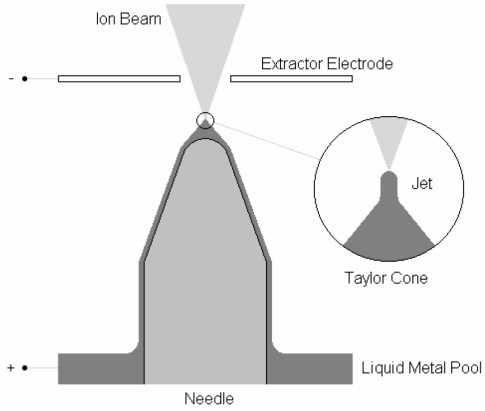

(a) Working principle of a Field Emission Electric Propulsion (FEEP) system, (Tajmar et al., 2004).

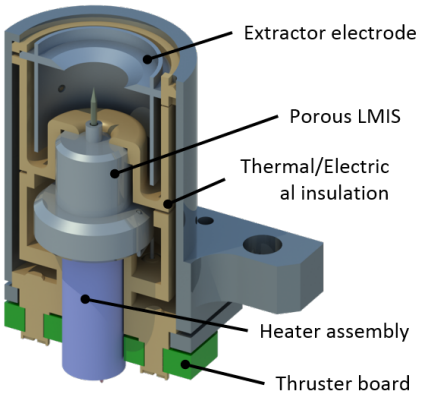

(b) CAD drawing of the NanoFEEP thruster head (Bock et al., 2016).

Figure 5.2: Working principle of a FEEP thruster and CAD model of the NanoFEEP thruster developed at the TU Dresden.

In general, problems with this technology comprise troubles with the high voltage of up to several tens of kV required for the extraction, ionization, and acceleration of the propellant. This voltage can create an electro-magnetic-interference (EMI) and may, if not well contained, lead to arching. However, since usually the extractor electrode is at ground potential while the needle tip is at a high positive potential the thruster heads can be built such that the high potential difference only occurs within the system and is not presented to any surrounding spacecraft components, especially on the outside, such as solar cells or antennas. Other issues usually arise in long term operations with the needle tip that may get congested by the metal propellant and erodes over time. While the needle's tip often can be cleaned by applying an even larger voltage as usual while heating it up, the erosion of the needle slowly increases the necessary operating voltage up to the point where the ionization field strength can no longer be achieved.

The NanoFEEP propulsion system is shown in Figure 5.2b. The thrust is generated through ionization and subsequent acceleration of small amounts of Gallium. The propellant is stored in the thruster heads (0.25 g each) and is heated to a temperature of about 50 °C at which the Gallium is liquid and flows along the porous needle to its tip. An electric voltage of up to 12 kV between the needle and the extractor cathode ionizes and ejects the propellant from the thruster by electrostatic force. The required voltage is generated from the unregulated battery voltage on one of the two PPUs which can provide up to 250 µA of ion current. Each PPU can interface and power two thruster heads and one neutralizer individually. A single thruster can generate continuously a thrust level of up to 8 µN with peaks of up to 20 µN.

Depending on the operation point of the thruster it reaches an I_{sp} between 1000 s and 8000 s. This is due to the fact that at low extractor currents almost all ejected material is ionized and accelerated whereas with higher extractor currents the ionization degree of the extractor jet decreases and the thruster becomes less fuel efficient. It is therefore favorable to operate the thruster at low thrust levels of up to about 5 µN at which the I_{sp} remains above 2000 s as shown in Figure 5.3. This also reduces the long term risk of deposition of unionized metal within the thruster head which may eventually lead to a failure of the thruster.

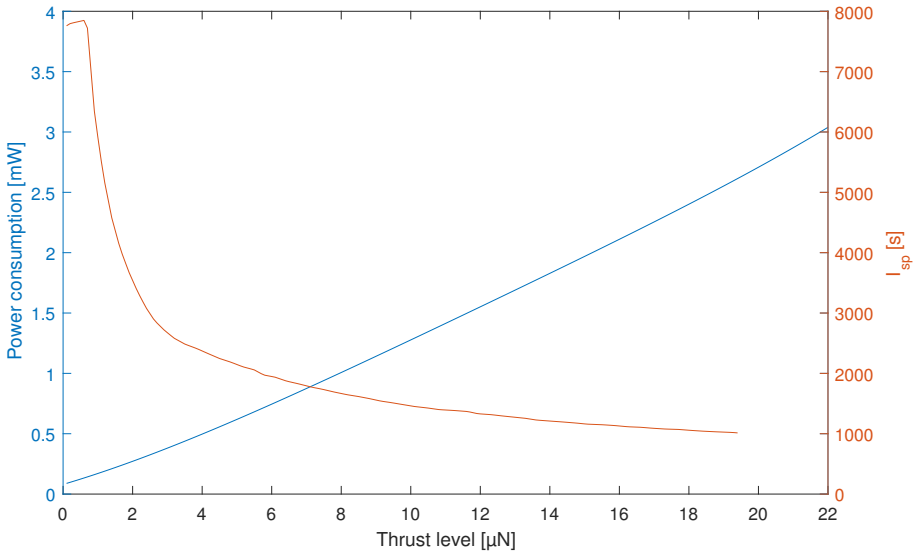

Figure 5.3: Power consumption and specific impulse of the NanoFEEP propulsion system, (Bock, 2016) and (Bock et al., 2016).

The power consumption of the system can be divided into two parts: First, the heating of the propellant to its operating temperature of about 50 °C requires, depending of surrounding satellite temperature, initially between 50 mW and 90 mW. The fuel compartment is

well isolated within the thruster head such that the heat dissipation is minimized and it is anticipated that once the thruster reaches its operating temperature the required heat flow is only minimal. The second part of the system's power consumption is the high voltage generation which is achieved by elaborate electronics including high voltage cascades. An achievable power conversion efficiency of about 65 % is currently anticipated meaning that for a beam power of 100 mW (corresponding to about 1.5 µN) a power consumption of 150 mW, excluding the heating, is expected.

The PPU is capable of producing a voltage operation range of 3 kV-12 kV with its nominal operation at beginning of life well below 5 kV. The typical starting voltage of the NanoFEEP is between 3.3 kV and 4 kV and the higher end of the voltage range is only required for cleaning operations. The ion current can be tuned between 0 µA and 250 µA and is directly translatable into the propulsion system's thrust.

The complete system consists of the thruster heads and two dedicated power processing units. The thruster heads have been integrated into the CubeSat bars as shown in Figure 5.4, while the PPUs are designed as standard subsystems for the UNISEC Europe bus.

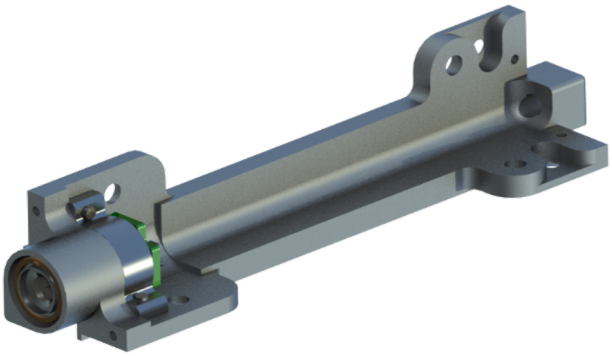

Figure 5.4: Mechanical integration of a NanoFEEP thruster integrated in the UWE-4 rail.

5.1.1.2 Attitude Determination and Control System

The UWE-4 attitude and orbit control system also inherits its basic setup from the UWE-3 ADCS. It is implemented as standard subsystem carrying a low-power micro-controller that fuses sensor data from magnetometers, sun-sensors, and gyroscopes, and computes attitude and orbit control outputs for the satellite's magnetorquer and the propulsion system. The system is shown in Figure 5.5.

The sensor suite is enhanced with respect to the UWE-3 ADCS but the original sensors have been kept as backup. The micro-controller now has access to a primary highly

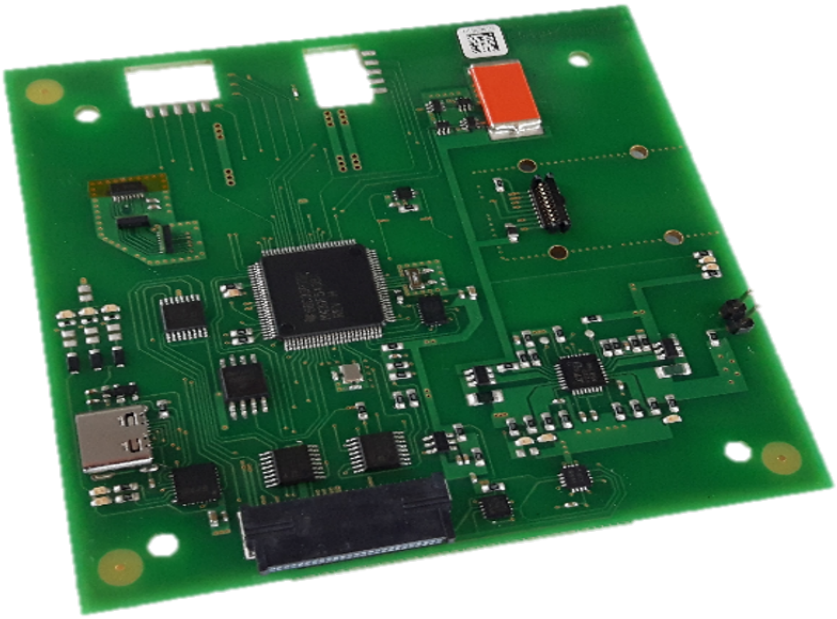

Figure 5.5: The UWE-4 Attitude and Orbit Control System (AOCS).

integrated MEMS 9-axis IMU (each 3-axis magnetometer, gyroscope, and accelerometer) placed on the AOCS board itself as well as a set of secondary magnetometers and high precision gyroscopes. Each CubeSat panel carries a redundant IMU and a high precision sun-sensor. All sensors' data can be injected into the Kalman filter sequentially and independently, such that a coarse attitude determination is also available during eclipse.

The sun-sensors are based on an ultra-low power miniature CMOS camera with a field of view of more than 90 ° at 250x250 pixel resolution and nominal power consumption of only 4.2 mW. An exemplary sun-vector acquisition image is shown in Figure 5.7 in which also the Sun identification result is presented. Preliminary calibration results indicate that a sensor accuracy of better than 0.1 ° is achievable (Bangert et al., 2016) and an accuracy of down to 0.01 ° might be achievable in the future. Shown in Figure 5.6 are the miniature sun-sensors in front of an UWE-3 panel with its digital coarse sun-sensor in the background.

Attitude control is performed with the help of magnetic torquers and the propulsion system. The torquers are placed on each panel (see Figure 5.8) with a total magnetic moment of 0.1 $\mathrm{A\,m^2}$ per axis and are mainly used for angular rate control. The four thrusters are used for precise thrust axis pointing. Although the thrusters can only exert a weak torque of up to 1 µN m each, the limited magnetic controllability of the satellite is completed and simulations presented in Chapter 5.4 show that a thrust vector pointing is feasible.

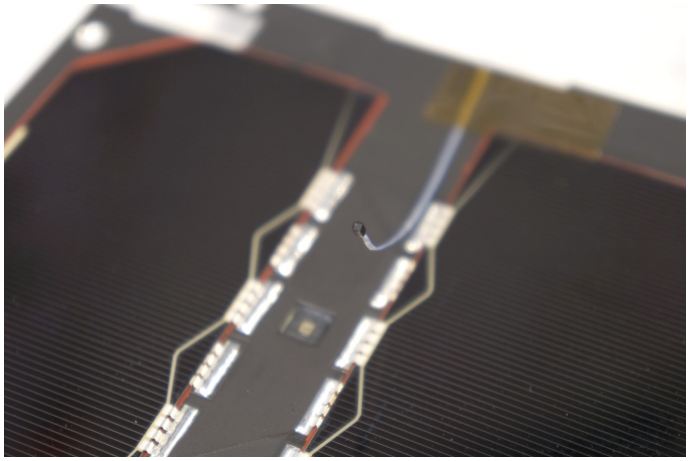

Figure 5.6: The UWE-4 miniature high precision sun-sensors in front of an UWE-3 panel.

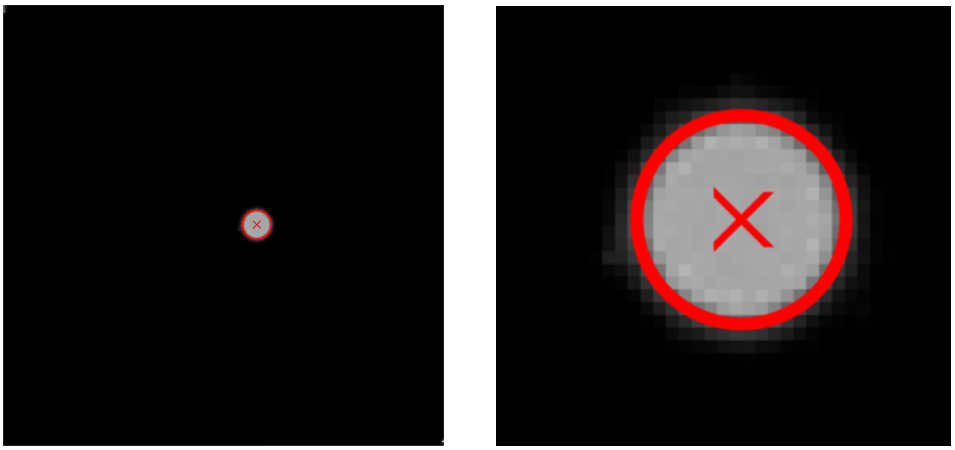

(a) Full view. **(b)** Zoom into Sun region.

Figure 5.7: An image of the Sun taken with the UWE-4 sun-sensor and with indicated sun identification and centroid estimation.

5.1.1.2.1 Magnetic torquer trade-off The magnetorquers have been optimized for the satellite's design with respect to their form, magnetic moment, and power demand. Due to their flat mounting requirement in order to accommodate them on the outside panels of the satellite no magnetic core material could be considered but only air-coils are used. For the optimization process technical data about the different types of self bonding copper wire was considered in the form of the DIN IEC 60317. There, different wire diameters together with their specific resistance and filling factors are given.

The magnetic moment m of an air-coil, or solenoid, is given by

$$m = nIA, \tag{5.1}$$

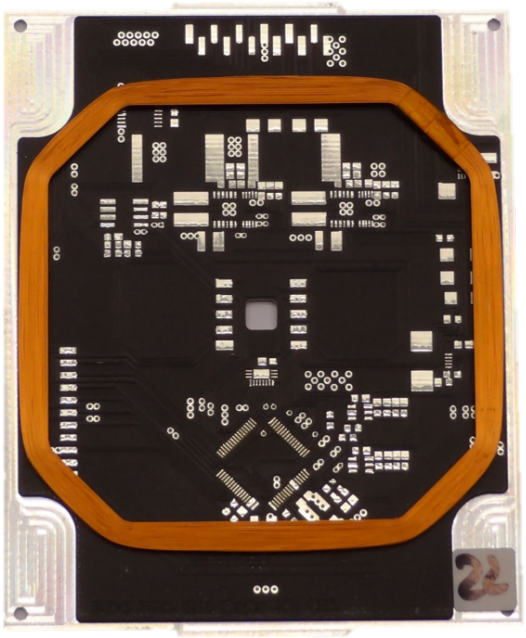

Figure 5.8: The UWE-4 optimized magnetorquers.

where n is the number of (identical) turns, I is the electric current running through the coil, and A is the area enclosed by the solenoid. With Ohm's law the equation can be rewritten as

$$m = \frac{nUA}{R}, \tag{5.2}$$

where R denotes the overall ohmic resistance of the coil and U is the operating voltage. The resistance is divided into the resistance of the coil itself and the resistance of the driving MOSFET electronics R_{DS}. Therefore

$$m = \frac{nUA}{R_\Omega + R_{DS}} \tag{5.3}$$

$$= \frac{nUA}{\lambda ln + R_{DS}} \tag{5.4}$$

with $R_\Omega = \lambda ln$ being the ohmic resistance of the coil. λ is the specific resistance of the coil's wire as given in IEC 60317 and l is the length of one loop. Therefore, for a fixed area the magnetic moment of the coil increases with higher operating voltage and lower specific resistance. On the other hand the required power to operate the coil can be calculated as

$$P = UI \tag{5.5}$$

$$= \frac{U^2}{\lambda ln + R_{DS}}. \tag{5.6}$$

and the power efficiency in terms of magnetic moment per watt is given as

$$\eta = \frac{m}{P} = n\frac{A}{U}. \tag{5.7}$$

The fixed parameters for the torquer design were their geometrical form as shown in Figure 5.9a with a maximized area of $A = 48.39\,\mathrm{cm}^2$ and loop length $l = 25.63\,\mathrm{cm}$ for the given panel design. Furthermore, the torquers are supplied from the satellite's unregulated bus voltage of $U \approx 3.8\,\mathrm{V}$ in order to increase the electrical efficiency by bypassing the power conditioning. The drain/source resistance of the driver MOSFETs is $R_{DS} = 2.5\,\Omega$.

The coil optimization started from the given available space on the panels defining the area but also its maximal height of 1.5 mm. The filling factor in terms of wires/cm^2 for each wire diameter defines the number of layers that can fit in the given space as well as the maximal number of turns n. Figure 5.9b shows the achievable magnetic moment vs. the number of turns for different wire diameters. Clearly visible are the different filling factors that result in a larger number of turns for smaller wire diameters. The magnetic moment increases with an increased wire diameter which is due to the smaller specific resistance of these wires. However, for one chosen wire diameter the number of turns only slightly influences the achievable magnetic moment. This is because in Eq. (5.4) n appears both in the numerator and denominator of the equation.

Figure 5.9c shows the required nominal power for the different wire options. The larger the wire's diameter the larger the power consumption is, therefore, favoring coils with small diameter and thus large λ. Coils with a higher number of turns require less power since n is only in the denominator of Eq. (5.6). Also Figure 5.9d shows that the power efficiency η decreases with larger wire diameters since less turns can be fit into to given available space and Eq. (5.7) is directly proportional to n.

The experience of the residual magnetic dipole moment documented in Chapter 3.2 as well as the findings related to spin control shown in Chapter 4.3 dictate the desired magnetic moment for UWE-4. It was anticipated that for a maximal difference in moments of inertia of $\Delta I = 8 \cdot 10^{-4}\,\mathrm{kg\,m}^2$ and a spin rate of $1\,^\circ/\mathrm{s}$ and $10\,^\circ/\mathrm{s}$ for the two involved axes, respectively, a precession torque of

$$|\omega \times (I\omega)| <= |\omega_1 \omega_2 \Delta I| <= 1\,^\circ/\mathrm{s} \cdot 10\,^\circ/\mathrm{s} \cdot 8 \cdot 10^{-4}\,\mathrm{kg\,m}^2 = 2.4 \cdot 10^{-6}\,\mathrm{N\,m} \tag{5.8}$$

is expected.

A minimal magnetic field strength of $B = 25\,\mu\mathrm{T}$ shall suffice to compensate this preces-

sion torque T_{req}, such that the required magnetic moment m_{req} was estimated to be

$$m_{req} = \frac{T_{req}}{B} = \frac{2.4 \cdot 10^{-6}\,\mathrm{N\,m}}{25\,\mu\mathrm{T}} \approx 0.1\,\mathrm{A\,m^2}. \tag{5.9}$$

This analysis motivated the search for a torquer solution that would produce $0.1\,\mathrm{A\,m^2}$ per axis or $0.05\,\mathrm{A\,m^2}$ per torquer, since there are two torquers mounted in each axis.

The selected configuration is marked in each plot of Figure 5.9 and specified in Table 5.1. The production of the magnetorquer was given to industry and one final product can be seen in Figure 5.8. The torquers fulfill the specifications as expected.

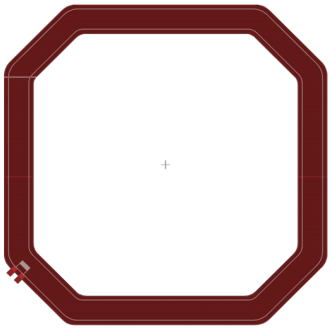

(a) Geometric design of the UWE-4 magnetorquers.

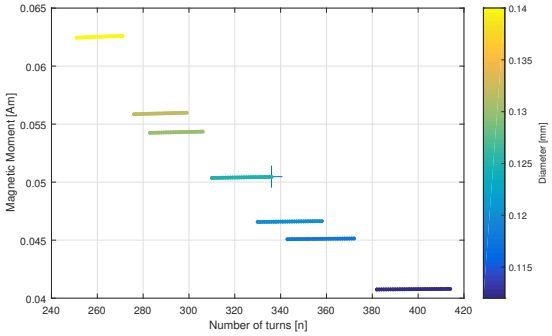

(b) Magnetic moment vs. number of turns vs. diameter.

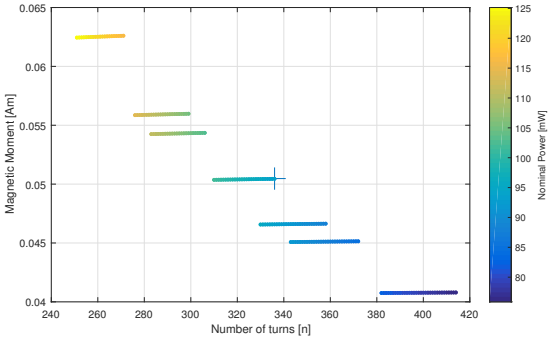

(c) Magnetic moment vs. number of turns vs. nominal power consumption.

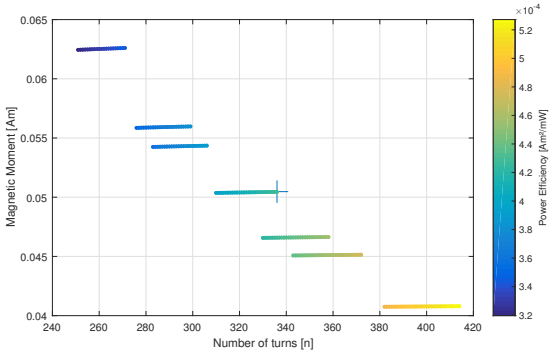

(d) Magnetic moment vs. number of turns vs. power efficiency.

Figure 5.9: Magnetorquer design trade-off.

5.1.2 Attitude Determination Performance

As presented in the previous section the attitude determination system for UWE-4 has been upgraded in order to achieve a higher determination performance at even lower power consumption. The new sensor suite made up of the BMX-055 IMU and the high-precision

Design specifications	Value	
Area	48.39	cm^2
Wire diameter	0.125	mm
Number of turns	336	
Magnetic moment	0.050	$A\,m^2$
Width	5.0	mm
Mass	10.3	g
Resistance	122.47	Ω
Current	31.02	mA
Nominal Power	93.5	mW
Power efficiency	4.28	$A\,m^2/mW$

Table 5.1: Design specifications of the UWE-4 magnetorquers.

sun-sensors are paired with an optimized Kalman filter. An extensive analysis carried out during the sensor selection process in 2016 (Aicher, 2016) showed a relatively small influence of the gyroscope due to thermal drifts (max. $0.3\,^\circ/s$ over a temperature range of about $50\,^\circ C$). Therefore, the gain parameters that control the Kalman filter's bias adjustment have been decreased relative to the ones used in UWE-3, resulting in a more stable performance especially during eclipse.

The simulations to estimate the projected attitude determination accuracy of UWE-4 have been carried out with sensor models developed based on the sensor performance tests. The attitude determination is evaluated in two scenarios that occur over the lifetime of the satellite in orbit. The first scenario analyzes the initial attitude determination when no previous knowledge is available to the AOCS and concludes with a steady state attitude determination performance in the absence of control. In the second scenario the magnetic torquers are activated for attitude control in terms of rate dumping and active residual dipole compensation.

In order to evaluate the attitude determination accuracy the RMS of the estimation error is computed. However, due to the fundamental difference between the eclipse and illuminated part of the satellite's orbit the analysis can be carried out for these two parts individually. Furthermore, the sensor readings' are evaluated similar to the attitude estimation consistency analysis presented in Chapter 2.2.1.

5.1.2.1 Initial Attitude Estimation

The on-board AOCS software is initialized with the default quaternion $q_{in} = [0,\ 0,\ 0,\ 1]$ and a covariance of $\mathbf{p} = \left[10^{-3},\ 0,\ 0\right]$. The simulation is initialized with a random quaternion

$q_0 = [-0.3302, -0.2737, 0.6816, -0.5929]$ and a random angular rate with norm of $2\,^\circ/\mathrm{s}$. The initial estimation error is more than $106\,^\circ$ which is decreased to an error of less than $1\,^\circ$ within the first half (sun-lit) part of the initial orbit. The initial estimation error is shown in Figure 5.10 where the yellow and black highlighted areas correspond to periods in sunlight and eclipse, respectively.

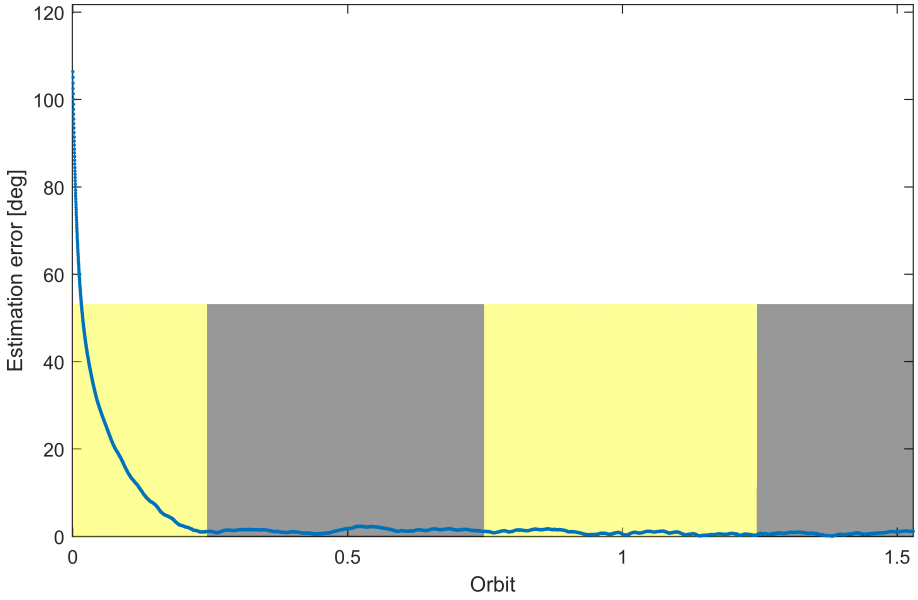

Figure 5.10: Attitude determination error angle after default initialization.

Steady state is achieved after about one orbit after which the estimation error does not exceed $1.5\,^\circ$ anymore. After three orbits, the estimation error remains well smaller than $1\,^\circ$ as shown in Figure 5.11.

After three orbits the attitude determination system reaches steady state. Here, the total RMS of the absolute estimation error is $0.42\,^\circ$, being $0.39\,^\circ$ and $0.45\,^\circ$ during the sunlit and eclipse part of the orbits, respectively. The histogram of the distribution is shown in Figure 5.12. In terms of sensor consistency analysis, according to Chapter 2.2.1, the magnetic field sensors achieve a median accuracy of $0.56\,^\circ$ with an RMS of $0.67\,^\circ$ during steady state. The sun-sensors achieve a median accuracy of $0.28\,^\circ$ with an RMS of $0.34\,^\circ$ during steady state. The histograms of the angular error of the 'measured' vectors with respect to the current attitude determination solution are shown in Figure 5.13.

This scenario demonstrates the good capability of the UWE-4 AOCS to converge towards the correct attitude estimation within the course of one orbit and continues to increase the estimation accuracy over next orbits. Even during eclipse periods the estimation performance remains high due to the decreased gain factors for thermal bias corrections.

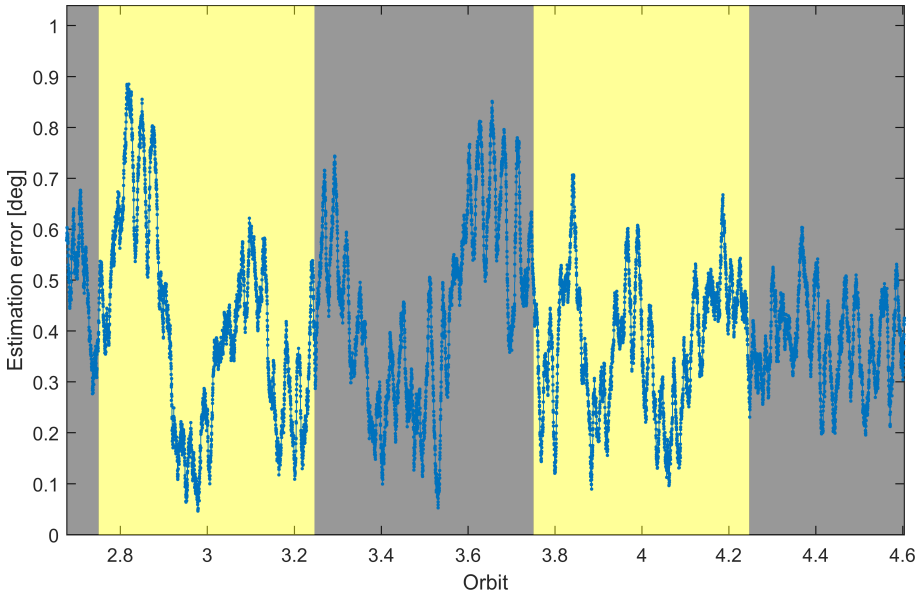

Figure 5.11: Attitude determination error angle after three orbits during the initialization scenario.

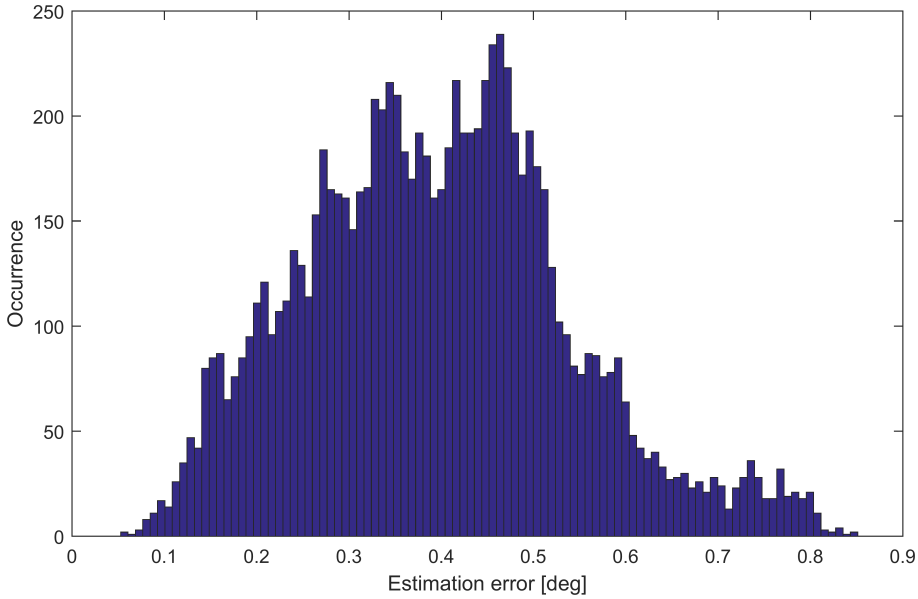

Figure 5.12: Histogram of the absolute determination error angle after three orbits during the initialization scenario.

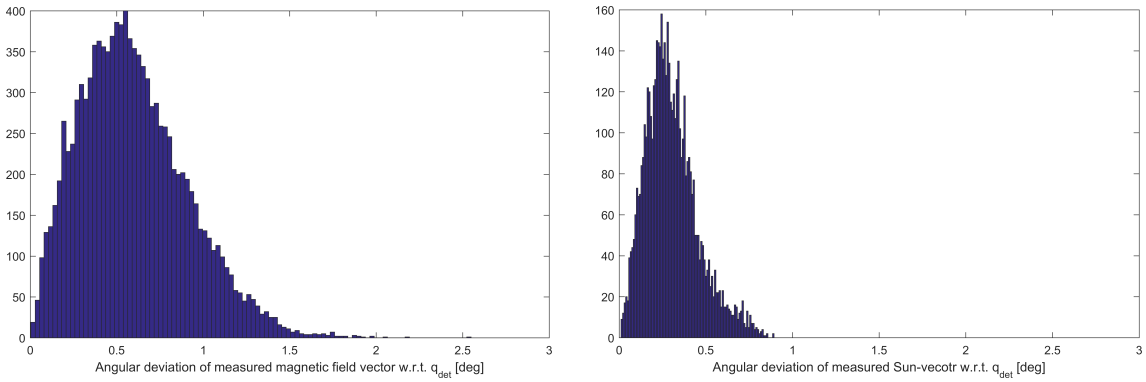

(a) Magnetic field vector. **(b)** Sun-vector.

Figure 5.13: Angular deviation of measured vectors w.r.t. the current attitude determination solution (compare to Figure 2.7 and Figure 2.8 in Chapter 2.2.2).

5.1.2.2 Attitude Determination during Attitude Control

In this scenario the satellite has a mean angular rate of 0.442 °/s and the system has perfect initial attitude knowledge. The attitude control system is commanded to reduce the angular rate only using the magnetic torquers and to cancel the torque due to an estimated dipole moment. The angular rate over the scenario time is shown in Figure 5.14. It is slowly decaying similar to the experiments performed with UWE-3 in orbit and presented in Chapter 4.2.2.

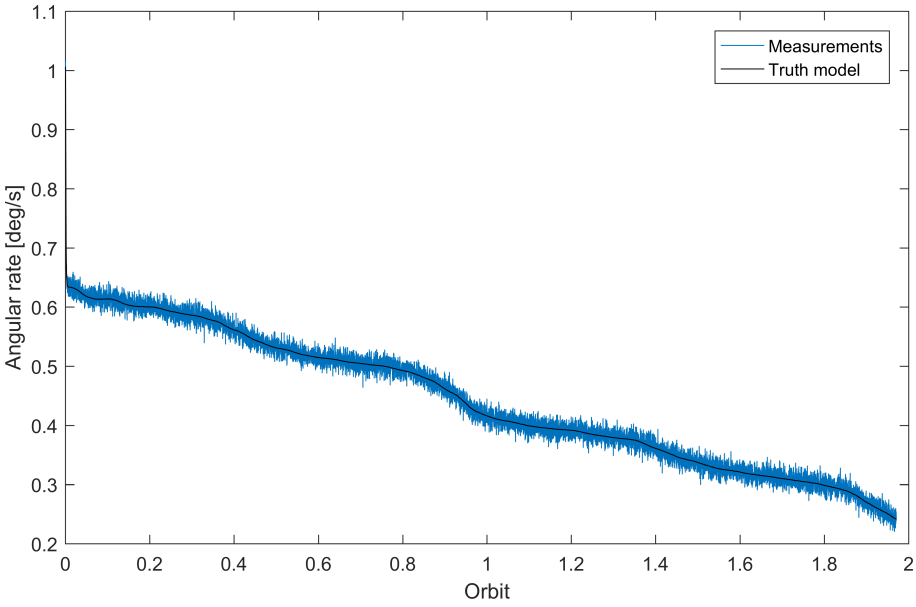

Figure 5.14: Angular rate during attitude determination performance scenario with magnetic control.

The performance of the attitude determination is even increased with respect to the

uncontrolled scenario of before. The absolute estimation has an RMS of 0.34 ° (0.32 ° during Sun, 0.36 ° during eclipse). The increased accuracy is due to the cancellation of a large portion of the residual magnetic dipole such that the satellite's dynamics resemble much better a rigid body without perturbations which are the attitude dynamics considered in the Kalman filter.

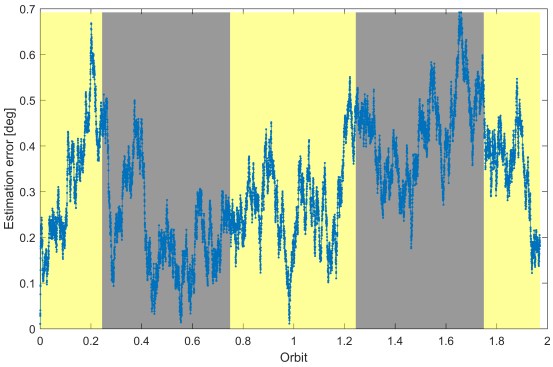

(a) Absolute attitude estimation error in sun (yellow) and eclipse (dark).

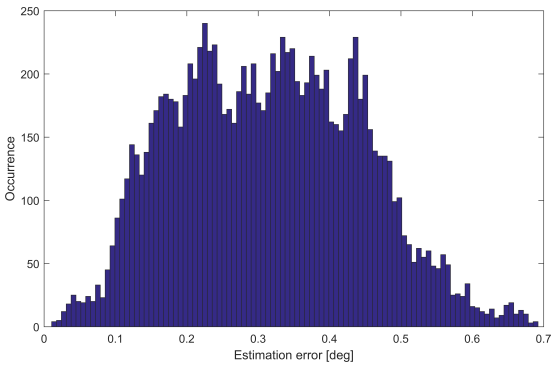

(b) Histogram of the absolute determination error angle.

Figure 5.15: Absolute attitude estimation error during UWE-4 attitude determination performance scenario with magnetic control.

When performing the consistency analysis in this scenario the deviation of the measured magnetic field shows a median of 0.44 ° (RMS 0.57 °) and the sun-vector a median of 0.24 ° (RMS 0.27 °).

5.1.3 Mission Operations Concept

The mission operation concept for UWE-4 focuses on the technical mission objective of demonstrating and characterizing the electric propulsion system in space. The secondary mission objective of performing orbit control maneuvers will only commence after that and requires significantly larger time scales of operations.

The first phase of operations (LEOP - Launch and Early Orbit Phase) will verify the correct behavior of the satellite bus just after launch. This comprises the establishment of two-way communication, the verification of a positive power budget, and monitoring of the satellite's temperatures, especially the batteries' temperatures. Since most recent launch campaigns have been cluster launches of sometimes even more than one hundred satellites (Rotteveel and Bonnema, 2017) the correct identification and target assignment may take up to two weeks. UWE-3 was only assigned the correct TLE by NORAD on December 4th 2013, thirteen days after launch, until which correct groundstation pointing was difficult and manual TLE adjustments were necessary (Busch et al., 2014b). The

positive power budget and temperatures will be verified mainly passively by analyzing the satellite's periodic health beacons.

Having established stable communication and with a safe satellite state the satellite's commissioning phase will begin. The ADCS will be switched on and the satellite's natural motion will be monitored as also done with UWE-3. During this second phase important information about the satellite will be gained such as initial tumbling rate, typical attitude disturbance torques, sensor miscalibrations, and sensor performance. The data gained throughout this shall be used for on-orbit calibration of the attitude determination sensors with the algorithms developed within this work and explained in Chapter 2.1. Then, the satellite will be initially detumbled followed by an attitude determination consistency analysis similar to Chapter 2.2.1. Finally, the magnetic torquers will be characterized in a procedure analogue to Chapter 3.3, which shall mark the end of this commissioning phase after which the satellite is ready for payload operations.

The first payload operations will target the payload's passive health status such as PPU temperatures and foremost the fuel compartments' temperatures. A dedicated payload beacon shall be activated that comprises this information and can therefore passively be gathered by supporting radio amateurs around the world. The fuel compartment temperatures are of most crucial importance since the propellant requires to be at about 50 °C for correct thruster operations. Heating tests to see how it reacts to active heating shall be carried out and the required power to achieve the operating temperature shall be measured. This preparation phase is a prerequisite for payload characterization in the next phase.

The goal of the characterization of the propulsion system in orbit is to measure the thrust level at different extractor voltages, the required power consumption for a given thrust, and to monitor any influences on the satellite's avionics during operations. Since the electric propulsion system produces very small thrust levels in the µN range its precise characterization is difficult to achieve via an orbit determination process. However, even very small torques on the satellite are measurable by the attitude determination system as shown during the UWE-3 mission. The residual magnetic dipole moment was estimated by analysis of the passively acting magnetic disturbance on the satellite's dynamics in Chapter 3.2. The measured torque levels range between 0.1 µN and 5 µN and vary according to the satellite's motion with respect to the Earth's magnetic field. The electric propulsion system of UWE-4, however, can generate a torque that is time invariant in body coordinates and is consequently even better to distinguish from noise and other perturbations. Therefore, a similar algorithm as used in UWE-3 for the residual magnetic dipole estimation will be used in UWE-4 for precise thrust estimation of each thruster.

This procedure is further described in the following Chapter 5.2.

When all four thruster heads and connected high voltage cascades have been characterized and are well functioning the secondary mission objective of orbit control maneuvers shall be put into focus. This eventually not only requires long term operations of the propulsion system but more importantly precise attitude control for thrust vector pointing. The hybrid attitude control employs the magnetic torquers as primary actuators and adds torques with the help of the propulsion system if necessary. The thrusters complete the limited magnetic controllability of the satellite and support attitude control with torques of up to 1 µN m each. The attitude control algorithms and simulations are presented in Chapter 5.4 where their application within the formation flying NetSat mission is explained.

5.2 Thrust Estimation Algorithm

The thrust levels provided by the NanoFEEP propulsion system require very enduring operations in order to estimate their impact on the satellite's orbit. Thus, a precise characterization through orbital changes is not feasible with such a system. However, due to their placement the thrusters create a significant torque which is measurable with the on-board attitude determination system.

The algorithm to determine the residual magnetic dipole moment of UWE-3 as described in Chapter 3.2 was based on the analysis of the natural motion of the satellite making use of an elaborated filtering technique of the satellite's on-board attitude sensor suite. Especially the rate gyroscopes play an important role in estimating acting torques and the magnetometers were used in order to determine the magnetic disturbance. As shown for instance in Figure 3.5 the algorithm is capable of determining torque levels well below 1 µN m already with the sensor suite used in UWE-3.

The torque created by the electric propulsion system $\mathbf{T}_\varepsilon$ in UWE-4 can be calculated as

$$\mathbf{T}_\varepsilon = \sum_{i=1}^{4} \mathbf{r}_i \times \mathbf{F}_i \tag{5.10}$$

with $\mathbf{r}_i$ being the thrusters' position with respect to the center of mass and $\mathbf{F}_i$ is the thrust created by each thruster i. The position of the thruster heads is approximately 5 cm away from the center of mass in each direction. For instance, the torque created by the thruster at position $\mathbf{r}_i = [5,\ 5,\ 5]^T$ cm at a thrust of $\mathbf{F} = [0,\ 0,\ -2]^T$ µN is $\mathbf{T}_\varepsilon = [-0.1,\ 0.1,\ 0]^T$ µN m. The torque for each thruster ranges between 7 nN m at $F = 0.1\,\mu$N and 1.41 µN m at $F = 20\,\mu$N.

In order to measure the thrust created by each thruster at a given extractor voltage level the satellite will record all available gyroscopes and magnetic field sensors over the activation time at the highest possible rate. The data will then be downlinked to ground where it will be analyzed. The algorithm presented in Chapter 3.2 is slightly adjusted to include $\mathbf{T}_\varepsilon$. The thruster position is well known prior to launch and determined very precisely due to the exact position of the thrusters' needle. The thrust direction is given by the thrusters' mounting direction and aligned with the negative Z axis. The complete optimization equation for a single thruster activation can therefore be written as

$$E(\mu, I, F) = \frac{1}{N}\sum_i^N \sqrt{\left(\mathbf{T}_\varepsilon(t_i) + \mathbf{T}_\mu(t_i) - \mathbf{T}_e(t_i)\right)^2} \tag{5.11}$$

$$= \frac{1}{N}\sum_i^N \sqrt{\left(\mathbf{r}\times\mathbf{F} + \mu\times\mathbf{B}(t_i) - I\dot{\omega}(t_i) - \omega(t_i)\times I\omega(t_i)\right)^2} \tag{5.12}$$

$$= \frac{1}{N}\sum_i^N \sqrt{\left(\mathbf{r}\times(-F\mathbf{e}_3) + \mu\times\mathbf{B}(t_i) - I\dot{\omega}(t_i) - \omega(t_i)\times I\omega(t_i)\right)^2}, \tag{5.13}$$

where $\mathbf{e}_3$ denotes the third unit vector in body coordinates (Z-vector). In Eq. (5.13) the main distinction between the torque created by the thrusters $\mathbf{T}_\varepsilon$ and other torques, such as the magnetic disturbance $\mathbf{T}_\mu$, can be seen: $\mathbf{T}_\varepsilon$ is constant over time in body coordinates for a given thrust level F while $\mathbf{T}_\mu$ changes direction depending on the actual Earth's magnetic field direction. This distinction will be most helpful in the determination process of the thrust level where it will be visible as constant angular acceleration about the axis $\mathbf{r}\times(-\mathbf{e}_3)$.

Despite this major distinction and the explicit algebraic derivation the determination process faces numerical issues that require further analysis. The very low torque levels that shall be measured for precise thrust estimation also at the lower end of the NanoFEEP thrust range demand precise measurements of the satellite's angular rate. Considering a similar moment of inertia of UWE-4 with respect to UWE-3, for instance a torque of $F = 0.1\,\mu\mathrm{N\,m}$ corresponds to an angular acceleration of only $\dot{\omega} = [-0.1414,\ 0.1412,\ -0.0018]\cdot 10^{-3}\,^\circ/\mathrm{s}$. In order to reach an angular rate of $0.0038\,^\circ/\mathrm{s}$, which corresponds to the sensitivity of the UWE-4 gyroscopes, the thruster needs to be activated at least 27 s. The gyroscopes' typical noise level of $0.1\,^\circ/\mathrm{s}$, according to their data sheet, is only reached after more than 700 s. However, UWE-4 will carry in total eight 3-axis gyroscopes which all will be recorded during the thrust estimation process in order to gain a higher precision through sensor fusion on ground.

The pre-flight analysis documented in the following section determines the required

specifications, such as thruster activation time, for the thrust estimation to be successful by making use of the attitude dynamics simulation as introduced in Chapter 5.1.2. For this, the UWE-4 sensor specifications have been included in the simulation.

5.2.1 Numeric Simulation

The thrust estimation simulation builds on the verified environment developed during in-orbit operations of UWE-3. It contains the dynamics of a rigid body, all available reference models such as the IGRF and sun-vector model, an SGP-4 propagator and detailed models of the satellite's sensors. The magnetic disturbance torque is included as well as the attitude determination and control on-board software. For the simulations carried out in this chapter, the thrusters were included into the simulation as well.

The thrust estimation algorithm as introduced in the previous Chapter 5.2 includes the estimation of the satellite's residual dipole moment, the true inertia tensor (with a fixed entry as explained in Chapter 3.2.4) and the thrust as excited by a single thruster head at a known fixed position.

The simulation settings were chosen to reflect a detumbled satellite with an initial random tumbling rate of $\omega_{init} = [-0.53,\ -0.82,\ 0.22]\,^\circ/\mathrm{s}$, according to the mission operation concept. The residual magnetic dipole of UWE-4 is considered to be much smaller than of UWE-3 and was set to $\mu_{res} = [9.11,\ -1.52,\ -8.22]\,\mathrm{mA\,m^2}$ with a total value of $12.36\,\mathrm{mA\,m^2}$.

The simulation date was fixed to January 1$^{\mathrm{st}}$ 2017 and the orbit was chosen to be the UWE-3 orbit. The simulation duration was altered between one minute and 45 minutes and different thrust levels were simulated, from 0.1 µN to 20 µN. Data points have been recorded for every second, resembling a realistic sampling and especially storage rate of the satellite in orbit.

A typical result is shown in Figure 5.16 where the absolute thrust estimation error in µN and the relative thrust estimation error in percent is plotted versus the true thrust level for a thrust duration of 30 minutes. It can be seen, that the thrust estimation algorithm can estimate already very small thrust levels of 0.1 µN with an accuracy of better than 10%. The absolute estimation error increases with the true thrust level while the relative error stays below 2%. At this maneuver duration, all estimation accuracies above a true thrust level of 1 µN are better than 1%.

In Figure 5.17 the complete results are shown for all different thrust levels as well as thrust activation durations. It is apparent that the thrust estimation becomes more reliable with increasing activation time and larger thrust level. On the other side, the satellite gains

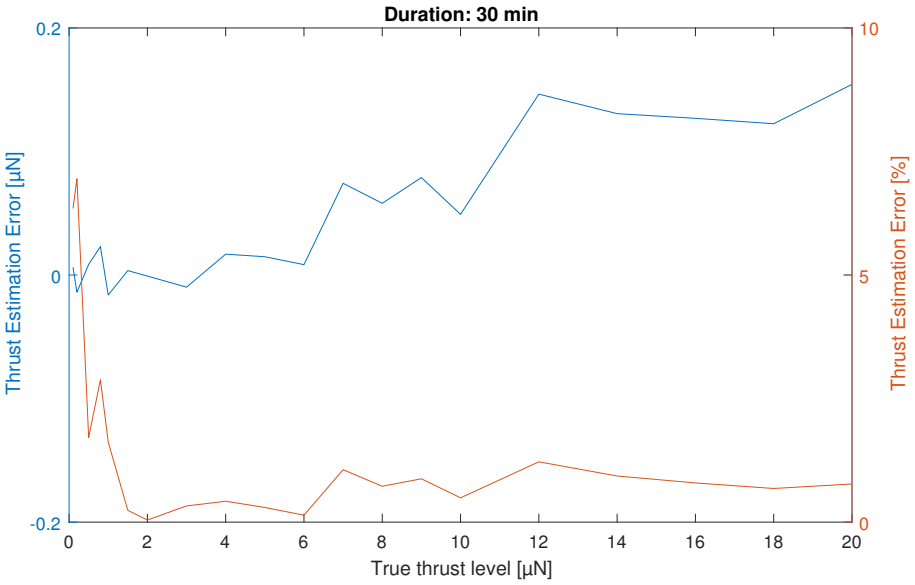

Figure 5.16: Thrust estimation accuracy at a duration of 30 minutes.

a significant rotation speed, especially for characterization at higher thrust levels. High rotation speeds lower the thrust estimation accuracy due to larger effects of the uneven (and partly unknown) inertia tensor and less data points per full rotation which are important for the residual magnetic dipole estimation. This effect is further shown in Figure 5.18 where the estimation error is plotted vs. the maneuver duration for a thrust level of 12 µN. A clear minimum is visible at a maneuver duration of 10 - 20 minutes, which is also apparent in Figure 5.17a.

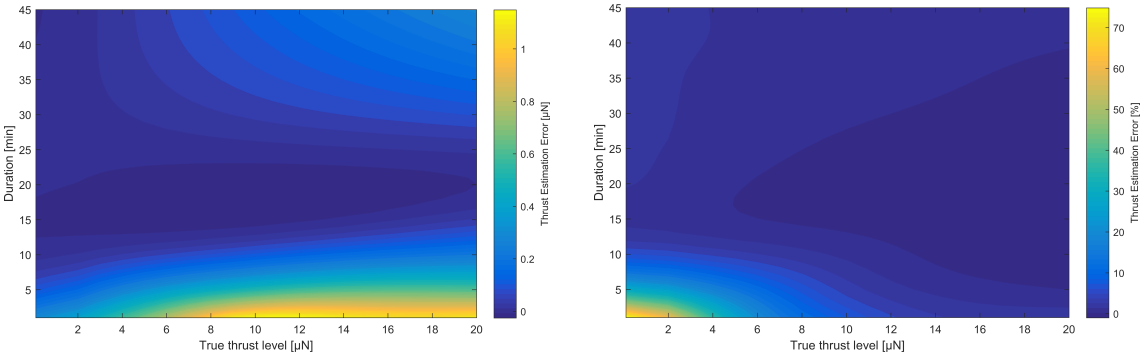

(a) Absolute thrust estimation accuracy. **(b)** Relative thrust estimation accuracy.

Figure 5.17: Numeric simulation of the UWE-4 thrust estimation algorithm.

Furthermore, the longer the thrust estimation maneuver lasts, the more power and fuel are consumed. The required energy for a 10 minute characterization maneuver at e.g. 12 µN can be estimated to be 68 mA h (assuming a battery voltage of 3.8 V) and

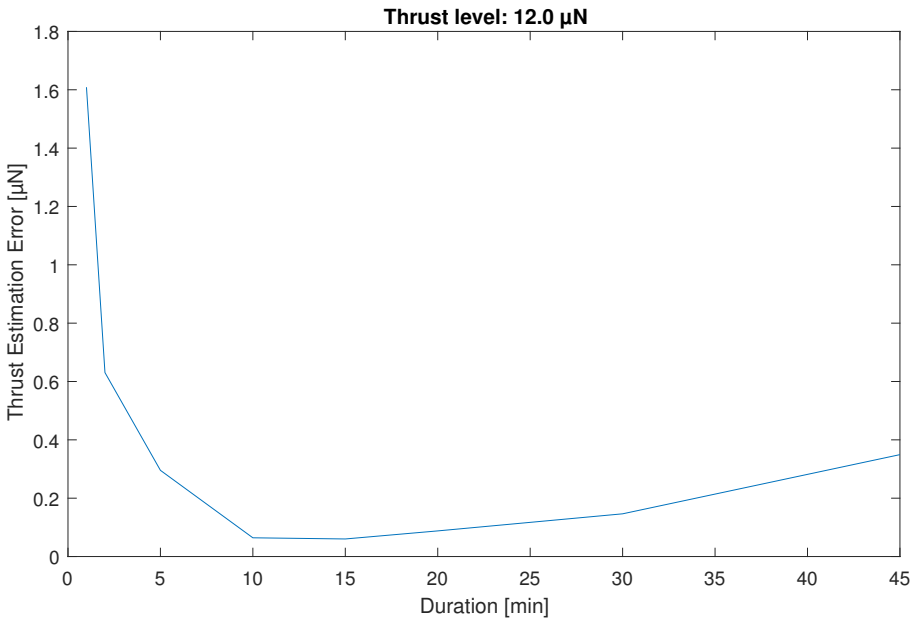

Figure 5.18: Thrust estimation accuracy for different durations at 12 µN thrust level.

the consumed fuel is 5.4 mg. The complete propellant and energy consumption for the different thrust levels is shown in Figure 5.19. If the characterization procedure is carried out with 10 minutes maneuvers over the complete thrust range as presented here, the total fuel consumption would be 62 mg or 24.7% of the entire fuel of one thruster head. The required energy for the complete characterization amounts to 0.80 A h or 30% of one of the satellite's batteries.

Therefore, in order to keep fuel and power consumption during the characterization low, the satellite's dynamics should be well known and understood beforehand. Thus, as anticipated in Chapter 5.1.3 it is important to analyze the satellite's natural motion first in order to estimate any disturbance torques. However, an absolute knowledge of all relevant dynamic aspects of the satellite can usually not be obtained and there will be more uncertainties when analyzing the in-orbit data of UWE-4 (Kramer et al., 2017).

This analysis serves as mission preparation and in its development already all necessary ground analysis programs have been implemented. Therefore, UWE-4 can quickly commence with the in-orbit characterization of the NanoFEEP thrusters when in orbit. The analysis algorithm is a modified version of the algorithm used with UWE-3 to estimate the residual magnetic dipole and is therefore a direct derivative of Chapter 3.

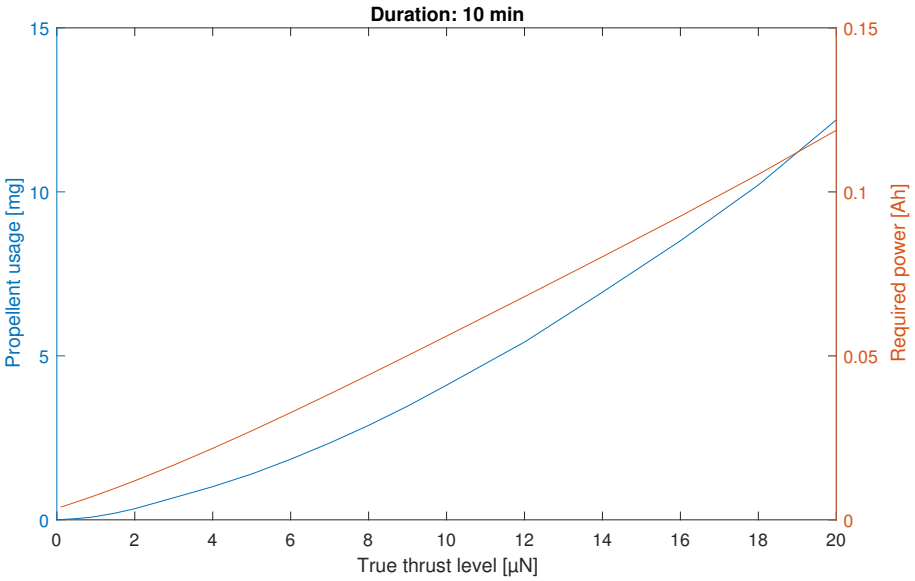

Figure 5.19: Propellant and power usage for a 10 minutes characterization maneuver at different thrust levels (battery voltage: 3.8 V).

5.3 Orbit Control Capabilities

The integration of the NanoFEEP propulsion system into UWE-4 shows that future miniature satellites' orbits may no longer be uncontrolled. The orbit control capabilities of a miniature satellite carrying an electric propulsion system similar to the NanoFEEP system are addressed in the following.

5.3.1 Δv Assessment

The maximal total change of a satellite's velocity, Δv, is a key parameter for any given propulsion system. It can be computed using the applied force F, the satellite's mass m, and the maximal operation time t_{op} such that

$$\Delta \mathrm{v} = \frac{F}{m} t_{\mathrm{op}}. \tag{5.14}$$

For the NanoFEEP electric propulsion system the thrust level F is directly linked to the propulsion system's specific impulse $\mathrm{I_{sp}}$ as shown in Figure 5.3. The maximal operation time, only considering fuel consumption, is dependent on the efficiency of the propulsion system, i.e. the $\mathrm{I_{sp}}$, which is the highest at lower thrust levels. t_{op} can be computed as

$$t_{\mathrm{op}} = \frac{\mathrm{I_{sp}}\, m_{\mathrm{prop}}}{F}, \tag{5.15}$$

where m_{prop} is the total propellant mass (0.25 g in the case of the NanoFEEP system), and F is the thrust level it is operating at. The maximal operating time as a function of the total thrust level (i.e. four NanoFEEP thrusters together) is shown in Figure 5.20. It can be seen that operation times of greater than 1000 h are possible with the little amount of fuel provided.

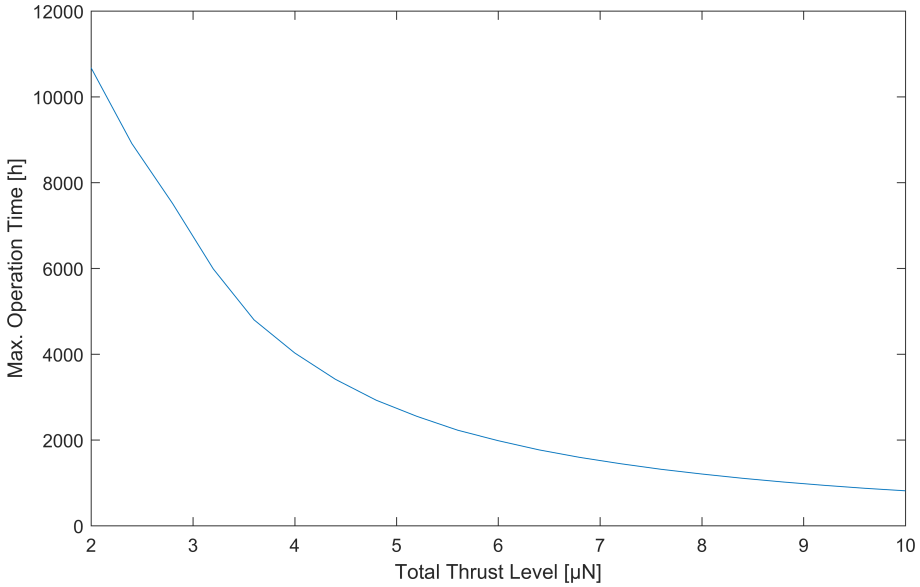

Figure 5.20: Maximal operating time vs. total thrust of four NanoFEEP thrusters.

The Δv provided to a range of CubeSats with masses between 1.0 kg and 2.5 kg is then computed for the different total thrust levels and presented in Figure 5.21. For a 1U CubeSat of 1 kg mass a maximum Δv of more than 75 m/s can be achieved with the presented NanoFEEP propulsion system while it still provides more than 30 m/s to a 2U CubeSat of 2.5 kg.

The limiting factor for using electric propulsion in a miniature satellite, despite the challenges concerning its integration, is the satellite's available power. For a 1U CubeSat typically a power budget of about 1.2 W is available to the satellite's bus and its additional systems. Assuming a bus power consumption of about 600 mW, similar to the UWE-3 power consumption when attitude control is active, the propulsion system may consume no more than 600 mW continuously. In order to estimate the most efficient operation point of the propulsion system for continuous orbit control the total power consumption vs. the total thrust level is plotted in Figure 5.22.

It can be seen that a total thrust of more than 3.2 µN continuously would consume more than 600 mW of power and is therefore not considerable as long term operation point. At this thrust level the propulsion system provides about 52 m/s of Δv to a 1U CubeSat

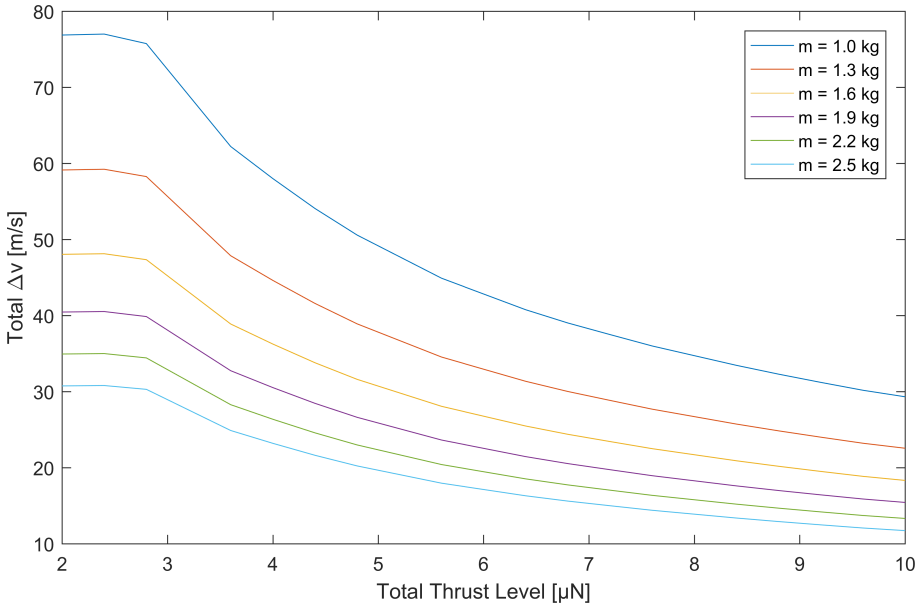

Figure 5.21: Total Δv provided to a range of CubeSats with different masses by four NanoFEEP thrusters.

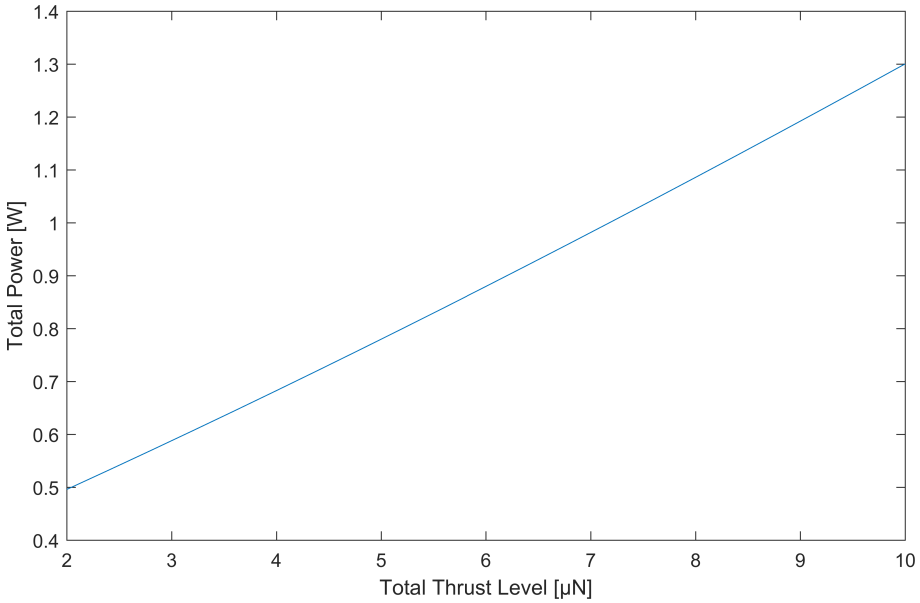

Figure 5.22: Total power consumption of four NanoFEEP thrusters vs. their total thrust level.

of 1.3 kg mass which is considered as the nominal scenario in the following application assessments.

5.3.2 De-Orbiting

The satellite population of the lower Earth orbits will continue to increase over the next decades, especially taking into account upcoming mega-constellations such as OneWeb or the SpaceX satellite constellation, which will make proper disposal of the satellites even more important than it is today. Any satellite brought in orbit by a European country has to obey to the ESA Space Debris Mitigation Requirements which state the limit of 25 years for the presence of debris in LEO that needs to be proven before launch through Orbit propagation analysis (e.g. using the ESA Tool DRAMA). However, this limit is widely considered to be too little restraining to avoid a dangerous over-population of these important orbits.

Therefore, any shortening of the satellite's remaining lifetime can help to avoid a large debris build up in LEO. While primary payloads of launch vehicles usually carry a propulsion system capable to dispose the satellites at their end-of-life according to the requirements, ride-share payloads often are not equipped with such systems. Depending on the primary payload's desired orbit the secondary satellites sometimes face a long natural decay of their orbits.

The DRAMA (Debris Risk Assessment and Mitigation Analysis) tool provided by ESA supports satellite mission designers in adhering to the international disposal requirements. The OSCAR (Orbital Spacecraft Active Removal) tool within DRAMA can be used to analyze different disposal strategies and assesses if the chosen strategy is compliant with the ESA Space Debris Mitigation Requirements.

Using the DRAMA tool the natural orbital lifetime of a 1U CubeSat has been determined for different initial orbit altitudes. January 1st 2018 was chosen as hypothetical launch date and the satellite was simulated to have a mass of 1.3 kg and a cross-section area of 0.017 m^2. Figure 5.23 shows the natural lifetime for a typical range of orbit altitudes with an indication of the 25 years lifetime requirement. The orbit's geometry was chosen to be circular and with an inclination of 98 ° such that it resembles a near sun-synchronous orbit.

It can be seen that orbits below ca 630 km altitude are naturally compliant with the ESA regulations.

Employing a standard low-thrust orbit change analysis (e.g. presented by Martinez-Sanchez and Lozano (2015)) it is possible to calculate the final orbit radius r of a circular

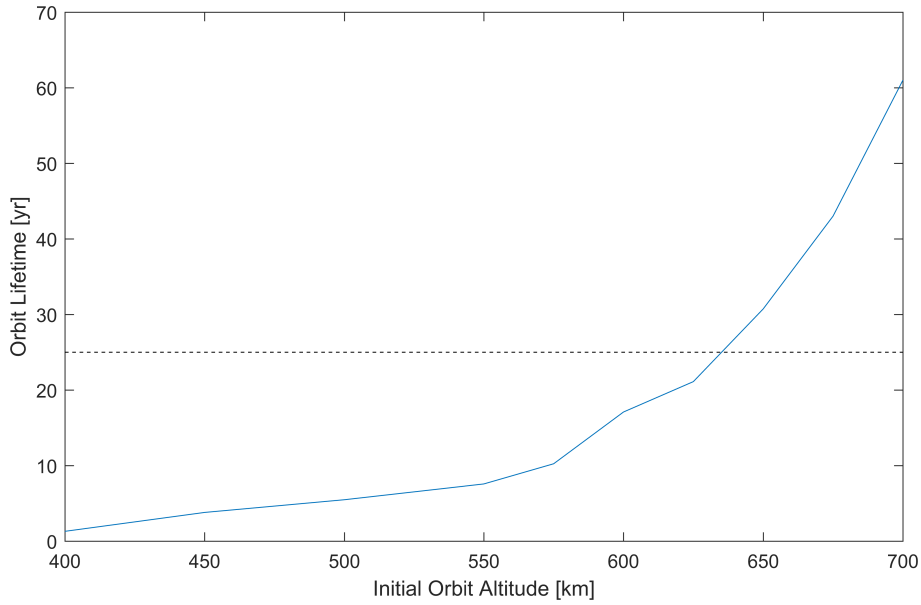

Figure 5.23: Natural orbit lifetime of a 1U CubeSat with 1.3 kg mass and 0.017 m^2 cross-section area. The dashed line indicates the max. 25 years orbit lifetime as required by the Space Debris Mitigation Requirements.

orbit after applying thrust in in-track or anti-in-track direction for a given time t:

$$r \approx \frac{r_0}{(1 - a_\theta t / v_0)^2}, \tag{5.16}$$

with r_0 being the initial orbit radius, a_θ being the acceleration in velocity direction, and $v_0 = \sqrt{\frac{\mu}{r_0}}$ being the initial orbital velocity. Furthermore, for a given orbital change between r_0 and r the required Δv can be computed as

$$\Delta v = a_\theta t_{\text{op}} \approx \sqrt{\frac{\mu}{r_0}} - \sqrt{\frac{\mu}{r}}. \tag{5.17}$$

Assuming a maximum continuous thrust of 0.8 µN per thruster (as dictated by their total power consumption of ca. 600 mW as shown in Figure 5.22) and a total operation time of about 6000 h until the 0.25 g of Gallium propellant are completely used up, one can compute the final altitude the system is capable of powering the satellite down to. The remaining lifetime of this orbit can be compared with the initial natural orbit lifetime as shown in Figure 5.23 to obtain an orbit lifetime reduction by using the electric propulsion system which is shown in Figure 5.24.

The lifetime of initially higher orbits can significantly be lowered with a reduction of more than 40 years in the case of a 700 km orbit. Obviously, the higher the initial orbit the more efficient the propulsion system can be used in order to reduce the remaining lifetime.

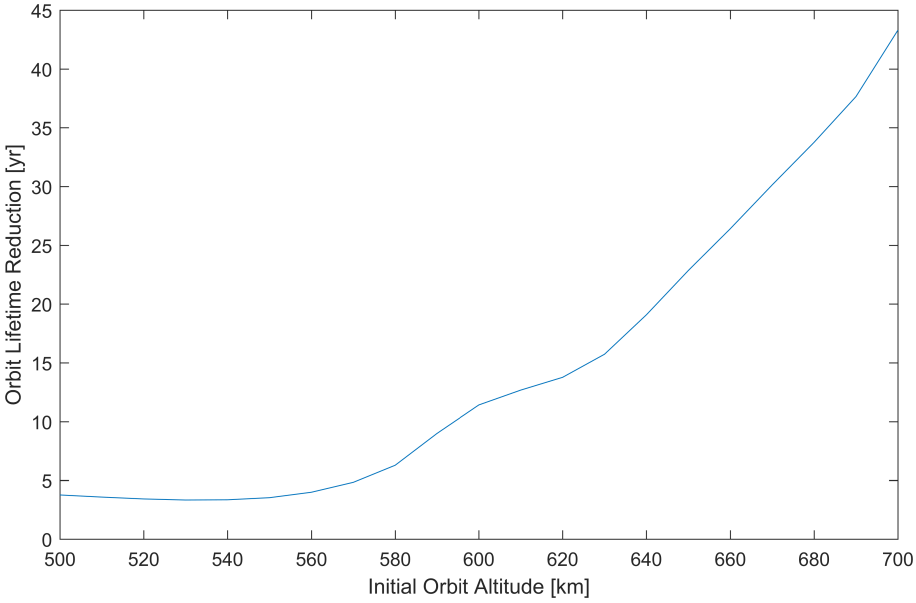

Figure 5.24: Orbit lifetime reduction of a 1U CubeSat using the NanoFEEP propulsion system.

However, also for lower orbits in the order of 550 km the propulsion system can be used to de-orbit the spacecraft much faster and therefore contribute to a sustainable and safe usage of the LEO environment.

5.3.3 Orbit Maintenance

An active orbit maintenance approach of very low Earth orbits is also feasible with the chosen electric propulsion system. In this scenario the satellite is released at altitudes below 450 km, for instance from the International Space Station ISS at currently 410 km altitude, and uses the propulsion system in order to maintain its orbital lifetime. The benefit of this approach is that once the satellite concludes its mission or experiences a major malfunction its remaining orbital lifetime is in the order of months and as such it does not contribute to the problem of space debris.

In order to assess the maximal orbit maintenance lifetime the atmospheric drag and thus the atmospheric density has to be estimated. The density varies according to the Sun's solar cycles and many different models exist that produce slightly different atmospheric density predictions for orbital altitudes. The one used in this analysis is the NRLMSISE-00 Atmosphere Model maintained by the US Naval Research Laboratory (Picone et al., 2002) which is an empirical model based on actual satellite drag data. Figure 5.25a shows the atmospheric density as predicted by the model for an altitude between 300 km and 450 km for an artificial launch date January 1st 2017. The atmospheric drag acting on the satellite's

orbit can be computed similar to Eq. (3.8) as

$$F_{drag} = \frac{1}{2} C_d \rho A V^2, \tag{5.18}$$

where C_d is the drag coefficient (typically $C_d = 2.2$ for orbital satellites), ρ being the atmospheric density, V the orbital velocity for a given orbit altitude, and A the cross-sectional area of the satellite. Choosing $A = \sqrt{3} * 0.1^2 \mathrm{m}^2 = 0.017\,32\,\mathrm{m}^2$ produces a worst case estimate for the aerodynamic force acting on a 1U CubeSat's orbit as shown in Figure 5.25b. The drag force varies between 0.1 µN and 9 µN depending on the satellite's altitude.

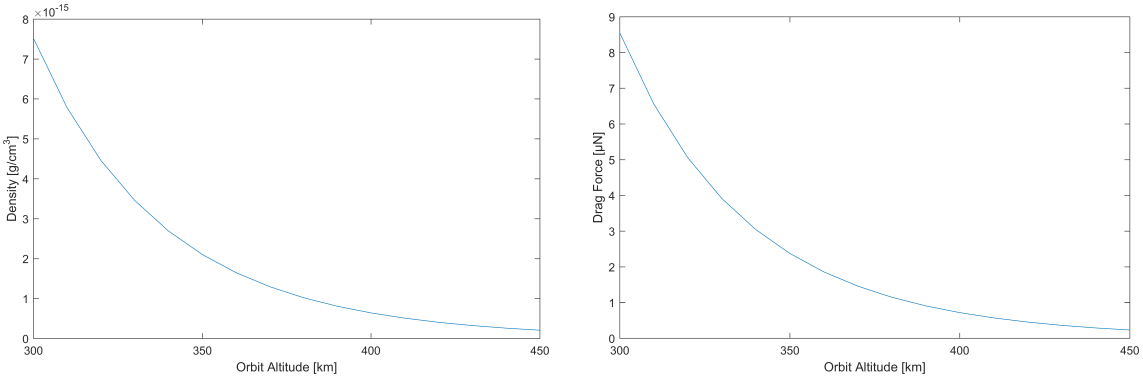

(a) Atmospheric density. **(b)** Atmospheric drag force for a 1U CubeSat.

Figure 5.25: The NRLMSISE-00 Atmosphere Model for altitudes between 300 km and 450 km for Jan 1st 2017 (Picone et al., 2002).

This means that a constant drag compensation is possible with the NanoFEEP propulsion system. The maximum orbit maintenance lifetime is computed considering complete fuel availability and is shown in Figure 5.26.

It can be seen that an orbit maintenance at altitudes below 320 km is only possible for some days up to roughly a year at 340 km. At altitudes above 400 km this highly increases up to more than 5 years due to the higher efficiency of the propulsion system at lower thrusts. In this analysis a cut-off at a minimum thrust of 0.1 µN has been implemented below which no continuous operation is feasible nor efficient taking into account the propellant consumption for attitude control. Separate orbit maintenance maneuver sequences however remain possible and would enable maintenance lifetimes of much longer than 7 years.

Therefore, the approach to launch CubeSats into very low Earth orbits and then maintaining their orbit using the propulsion system is very much valid. It would eliminate the risk for space debris build-up while still allowing mission durations of several years. Furthermore, a multitude of cost-efficient launch options become available due to the

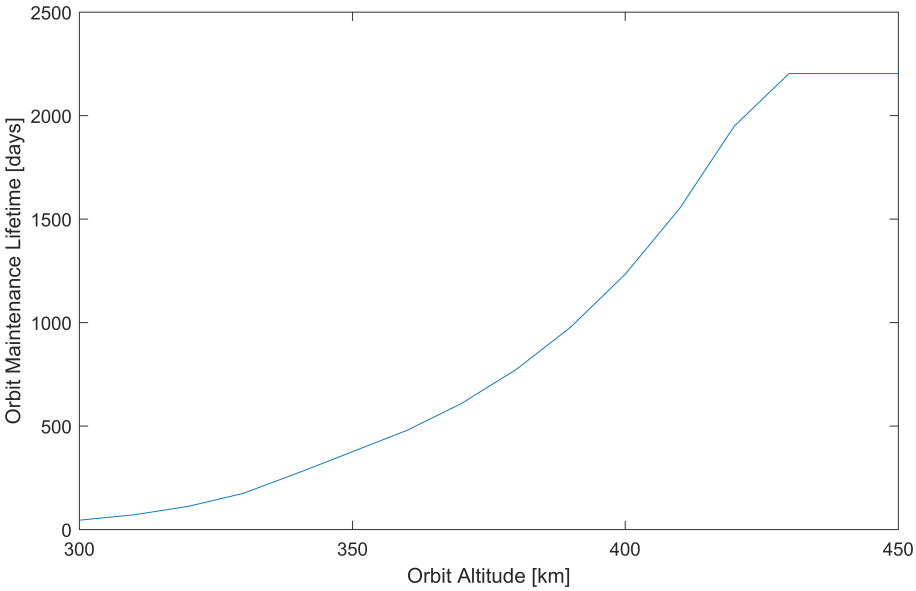

Figure 5.26: Orbit maintenance lifetime for a 1U CubeSat using the NanoFEEP propulsion system at altitudes between 300 km and 450 km.

frequent launches to the International Space Station. The drawback of this approach is the higher nominal power consumption of the spacecraft in order to achieve orbit maintenance and the increased mission risk due to its dependency on the propulsion system. A failure of the latter may shorten the remaining orbital lifetime and thus put a mission's success at risk.

Qualifying the NanoFEEP propulsion system in orbit will help to assess and increase its reliability in order for future missions to integrate it as orbit maintenance device rather than using it as de-orbiting system.

5.4 Hybrid Attitude and Orbit Control

The attitude and orbit control of UWE-4 will make use of the satellite's electric propulsion system. For attitude control, primarily the magnetorquers will be used in order to achieve an energy saving nominal operation of the satellites. During orbit control maneuvers, however, the thrusters are activated and compliment the magnetic attitude control in order to achieve precise thrust vector pointing independent from the actual ambient magnetic field. Attitude control, therefore, is achieved through a hybrid control of the satellite's magnetorquers and its electric propulsion system. For this, the modular generic attitude control architecture introduced in Chapter 4.1 has been adjusted to incorporate the electric actuators.

5.4.1 Thrust Vector Pointing Controller

The hybrid attitude control has the major objective to point the thrust vector of the satellite into a given direction with minimal actuation of the thrusters in order to save energy and fuel. Therefore, the controller maximizes the use of the magnetorquers and only adds a required minimum of torque by activating the thrusters. In its current implementation, the controller accepts target thrust vectors in ECI or LVLH coordinate systems, but future implementations of the same kind may also accept vectors in ECEF coordinates in order to support pointing control of a camera for instance.

Furthermore, the controller automatically interpolates between two given target thrust vectors This is necessary because the formation control algorithms optimize the maneuvers for a whole orbit and output thrust vectors at equidistant time intervals of typically five minutes. Depending on the satellite's orbital position the target thrust vector may vary over the duration of one maneuver. By interpolating between two consequent target thrust vectors the controller assures smooth transition between the discrete target vectors given by the formation controller.

The controller distinguishes between periods at which a total thrust is required (calculated and given by the formation controller) and pre-orbit-maneuver activities that are required to turn the thrust vector in the target direction. During the pure attitude maneuvers the thrust of each thruster is limited to a parameter called F_{attctr} while during orbit control maneuvers the thrusters are each limited to the parameter F_{orbctr}. For the following simulations $F_{attctr} = 0.8\,\mu\text{N}$ and $F_{orbctr} = 2.5\,\mu\text{N}$ have been chosen.

In its first step, the hybrid attitude controller calculates the required rotation α in order to align the satellite's body thrust vector $\mathbf{F}_{thr}$ with the target vector given in ECI coordinates $\mathbf{F}_{target}$ (for LVLH or other target vectors they have to be transformed into ECI first). This rotation is defined by

$$\mathbf{r} = \mathbf{F}_{thr} \times (q * \mathbf{F}_{target}), \tag{5.19}$$

where $q*$ denotes the transformation from ECI into body coordinates using the current attitude estimation. The required angular change θ can be calculated as

$$\theta = \arcsin\left(\frac{\mathbf{r}}{|\mathbf{F}_{thr}|\,|q * \mathbf{F}_{target}|}\right). \tag{5.20}$$

From this, an error quaternion can be defined as

$$q_e = \begin{bmatrix} \frac{\mathbf{r}}{|\mathbf{r}|}\sin(\theta/2) \\ \cos(\theta/2)) \end{bmatrix} \tag{5.21}$$

and a desired angular acceleration can be derived as

$$\dot{\omega}_{des} = -k_d \omega + k_q \begin{bmatrix} q_e(1) \\ q_e(2) \\ q_e(3) \end{bmatrix} q_e(4) \tag{5.22}$$

with a differential gain parameter k_d and a gain parameter for the error quaternion q_e. For the following simulations $k_d = 0.02$ and $k_q = 0.1$ were set.

This desired angular acceleration is then input to the generic attitude controller implemented in UWE-3 and described in Chapter 4.1. It outputs the desired magnetic control moment $\mathbf{m}_{des,ctr}$ and the desired control torque $\mathbf{T}_{des,ctr}$. After normalization of $\mathbf{m}_{des,ctr}$ to the actually available control moment strength (max. moment of the magnetorquers), $\mathbf{m}_{ctr}$, a control torque produced by the torquers and the residual magnetic dipole (μ_{est}) can be computed and the missing difference to the desired total control moment can be computed:

$$\Delta \mathbf{T}_{ctr} = \mathbf{T}_{des,ctr} - (\mathbf{m}_{ctr} + \mu_{est}) \times \mathbf{B} \tag{5.23}$$

The missing control torque needs to be achieved with the thrusters. Their torque is depending on their individual location in the satellite's body with respect to the center of mass of the satellite $r_{cm,thruster,i}$. Without loss of generality the thrusters' positions were assumed to be at the +Z corners of a 10 cm cube generating a torque matrix given by

$$A = \begin{bmatrix} 1 & 1 & -1 & -1 \\ -1 & 1 & 1 & -1 \\ 0 & 0 & 0 & 0 \end{bmatrix} r_{cm,thruster} \tag{5.24}$$

that transforms a given thruster activation setting for the four thrusters into a resulting torque. In reverse, the pseudo-inverse of A multiplied by the desired torque gives the required activation pattern for the thrusters. This needs to be filtered for "negative" activation values, for which an equivalent action of the opposite thruster needs to be applied.

Then, the computed thrust levels need to be restricted to F_{attctr} or F_{orbctr} which is done in a scale-down process. I.e., if there is a single value exceeding the limit then all thrust levels are equally reduced such that the maximal value meets the limit. This way the produced torque direction is not changed in the process but only its total value. Furthermore, the controller checks for a minimal thrust level (typically set to 0.1 µN) below which the thrust level is considered to be zero. This resembles the thrusters' minimal ignition voltage at

which already a small current is flowing and thus a small thrust is generated.

During orbit control maneuvers the total thrust for all four thrusters is computed and homogeneously increased for the case that the formation control input requires higher thrust. However, this is only applied if the current thrust vector is within a certain angular cone with opening angle β from the desired thrust vector. The thrust level that is applied in the ideal direction can be computed as

$$F_{ideal} = \mathbf{F}_{thr} \frac{\mathbf{F}_{target}}{|\mathbf{F}_{target}|} \tag{5.25}$$

$$= |\mathbf{F}_{thr}| \cos(\beta), \quad \text{with} \tag{5.26}$$

$$\beta = \angle(\mathbf{F}_{thr}, \mathbf{F}_{target}) \tag{5.27}$$

A typical value for this angular cone is $\beta = 10\,^{\circ}$, at which the attitude controller delivers the thrust level with 98.5 % accuracy. Simulations where the thrust level is adjusted with a weighting factor of $\cos(\beta)$ have also been carried out but were discarded due to the fact that the controller then constantly underperforms in terms of its output thrust level. A gain factor of $1/\cos(\beta)$ that automatically increases the output thrust to meet the ideal thrust level has also been studied but poses the risk of large off-pointing thrust vectors and therefore large disturbances to the formation control algorithm. Furthermore, the fuel and power consumption is highly increased in this case which is critical for the satellite's mission operation.

The hybrid attitude and orbit controller ensures the correct pointing of the satellite's thrust axis and also adjusts the thrust level demand for each thruster to meet the requirements from the formation controller. It optimizes the use of the satellite's magnetorquers for attitude control and adds torque from the thrusters only if required. During orbit control maneuvers the controller ensures that the correct thrust level is applied and utilizes the thrusters at the same time for attitude control torques.

In the following chapter simulations for two different formation control scenarios are described and the controller's performance evaluated.

5.4.2 Simulation

The simulation was carried out for two different formation control scenarios, each lasting for 24 hours:

1. A change of an Along-Track-Formation (ATF) about 1000 m in distance.
2. A formation transformation from ATF into a Cartwheel-Helix (CWH) formation with 500 m separation.

Scenario 1 only requires in-plane correction maneuvers and can in general be regarded as the simplest formation change maneuver while Scenario 2 can be regarded as one of the most complex formation change maneuvers and requires out-of-plane thrust vectors.

The simulations include attitude disturbances due to a residual magnetic dipole moment and a very small component that resembles weak magnetic interaction with the Earth's magnetic field. The sensors' and actuators' characteristics are those of the UWE-4 ADCS suite, the thrusters are simulated according to the NanoFEEP characteristics. Initialization comprises an initial random tumbling rate of about $2\,^{\circ}/\mathrm{s}$ and an initial random attitude. The attitude determination however is given prior knowledge of its initial attitude and residual dipole in order to avoid the initial estimation process and focus on attitude control.

5.4.2.0.1 ATF-1000 The ATF-1000 formation control scenario simulates the re-positioning of a single satellite in an Along-Track-Formation about 1000 m within the orbit plane. To do so, the satellite thrusts opposite to its velocity direction in order to change its relative semi-major axis with respect to the leader's orbit. After drifting and small correction maneuvers, the satellite increases its velocity again and synchronizes it with the leader's orbital velocity. Therefore, except for minor corrections, the satellite performs this maneuver entirely within its orbit plane.

The simulation carried out lasts for 24 hours and the formation controller demands a total Δv of $0.045\,959\,\mathrm{m/s}$ during a total of 24 orbit control maneuvers within about 15 orbit revolutions. The total maneuvering time is 23 400 s or 6.5 h which is 27 % of the scenario time. The maneuvers each have a duration between only 5 min and 50 min and the desired thrust level is between 0.5 µN and 8.9 µN. This is shown in Figure 5.27 where the thrust profile is presented over the scenario time. The thrust vector here is given in LVLH coordinates.

In Figure 5.28 the controller's thrust output is shown with the desired thrust level as colored reference area. It can be seen that the attitude and orbit controller is capable to provide the correct thrust level during the majority of the maneuvers. In fact, the Δv delivered over the complete scenario is $0.048\,52\,\mathrm{m/s}$ which is a little higher than the desired total Δv. The difference is due to the utilization of the thrusters for attitude control just before an orbit maneuver. A single maneuver is shown in Figure 5.29 in more detail where also the 5 min period before the actual orbit control maneuver is clearly visible during which the thrusters are already used for correct thrust vector pointing. Also visible is the interpolation between consequent thrust demands of the formation controller in order to avoid a discrete mismatch between two given target vectors.

The delivered orbit control Δv, i.e. the amount of acceleration that is in the target LVLH

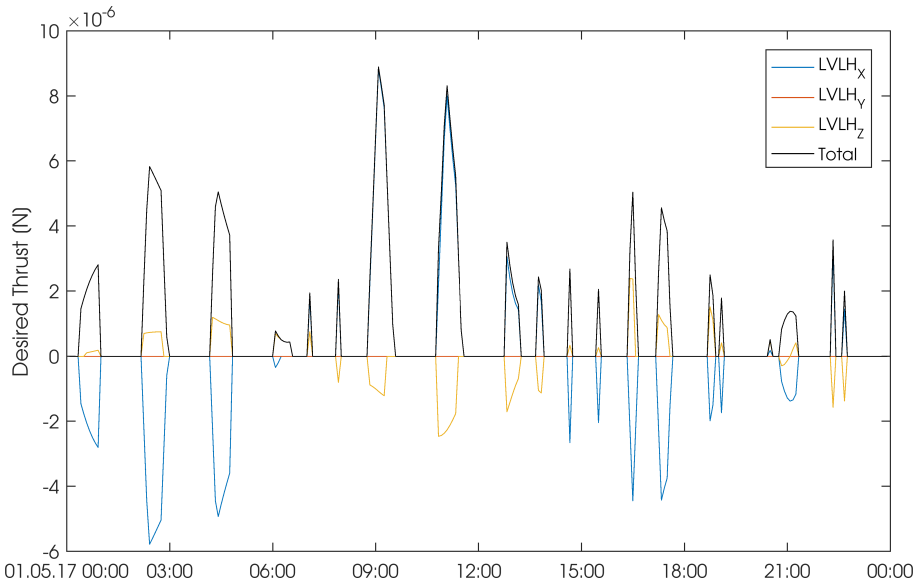

Figure 5.27: Desired thrust profile in LVLH during the ATF-1000 formation change maneuver.

direction, can be computed by comparing the satellite's attitude pointing performance. Since the satellite's target pointing is only defined during orbit control maneuvers the analysis is only carried out for these periods. The off-pointing is shown in Figure 5.30 as histogram. During the majority of time the AOCS points the thrust vector in target direction. The mean deviation is 0.997 ° with an RMS of 1.96 °. A total of 263 s during the orbit control maneuvers the AOCS cannot achieve correct pointing to within 10 ° which is only 1.1 % of the total maneuvering time. This means that for 98.9 % of the scenario time the AOCS achieves its demanded pointing requirement.

The Δv projected onto the target pointing vector, i.e. the part of the thrust generated in the perfect target direction, can be computed to be 0.045 83 m/s which corresponds to 99.7 % of the demanded Δv. The fuel usage during the complete formation change is in total 0.014 g which is almost evenly distributed among the four thrusters as shown in Figure 5.31 and is equivalent to 1.40 % of the satellite's total fuel reserves. Clearly visible are the two large maneuvers at ca. 09:00 UTC and 11:00 UTC during which the propellant usage quickly increases. The amount of fuel solely used for attitude control, i.e. during the 5 min period before an orbit control maneuver, is only 3.87 % of the total fuel used. The average power demand over the complete scenario amounts to 169 mW which is well within the satellite's capabilities.

Just before new orbit control maneuvers the satellite rotates with angular rates of up to 3.122 °/s while it achieves a mean angular rate over the scenario of only 0.1062 °/s. The angular rate after initialization and during the first maneuver is plotted in Figure 5.32. The

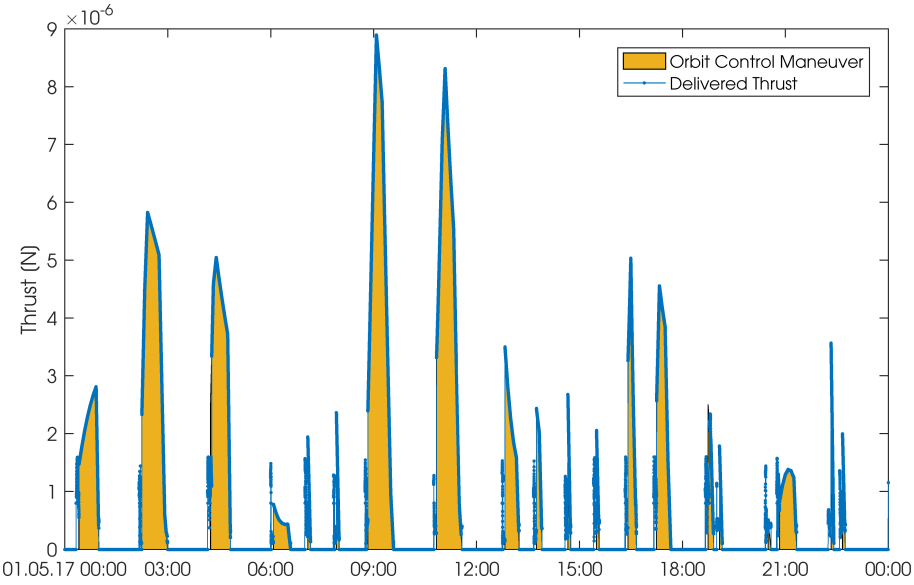

Figure 5.28: Delivered thrust profile during the ATF-1000 formation change maneuver.

scenario is initialized with a random angular rate of about 2 °/s which is quickly damped by the magnetic controller until the rate vector is parallel to the Earth's magnetic field at which point (ca. 00:37 UTC) the magnetic controller only slowly is able to further decay the angular rate. At 00:20 UTC the pointing controller is activated, five minutes prior to the first demanded thrust. At this point the satellite utilizes the magnetorquers and thrusters together to re-point its Z-axis which corresponds to an increase of the angular rate to a maximum of 2.6 °/s. At 00:25 UTC the orbit control maneuver begins and lasts until 01:00 UTC after which the controller switches to a pure magnetically controlled stabilization.

5.4.2.0.2 CWH-500 The initialization of a CWH belongs to the most complex formation change maneuvers that shall be demonstrated within the NetSat mission. The formation control not only requires thrust vectors within the orbit plane that change the orbit's semi-major axis or argument of perigee, but also requires orthogonal thrust vectors for change of the individual satellite's inclination. Furthermore, the demanded thrust vector does not stay constant within one maneuver but can change its direction considerably. Simulations performed for this type of maneuver typically require long durations on a time scale larger than 24 h. However, for attitude control purposes the simulation of only a part of the formation change maneuver is sufficient in order to evaluate the controller's performance.

During a total of 395 min (i.e. 27.4 % of the scenario) the formation controller demands a total Δv of 0.055 57 m/s with thrust levels of up to 12 µN. The desired thrust profile in

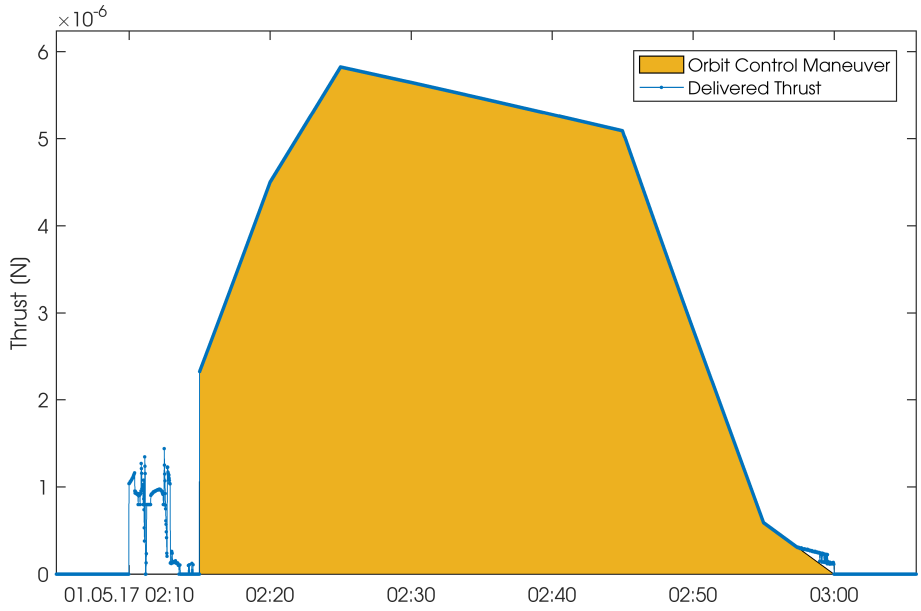

Figure 5.29: Zoom-in on a maneuver from 02:15 to 03:00 UTC where the attitude control activities before the orbit control maneuver are visible.

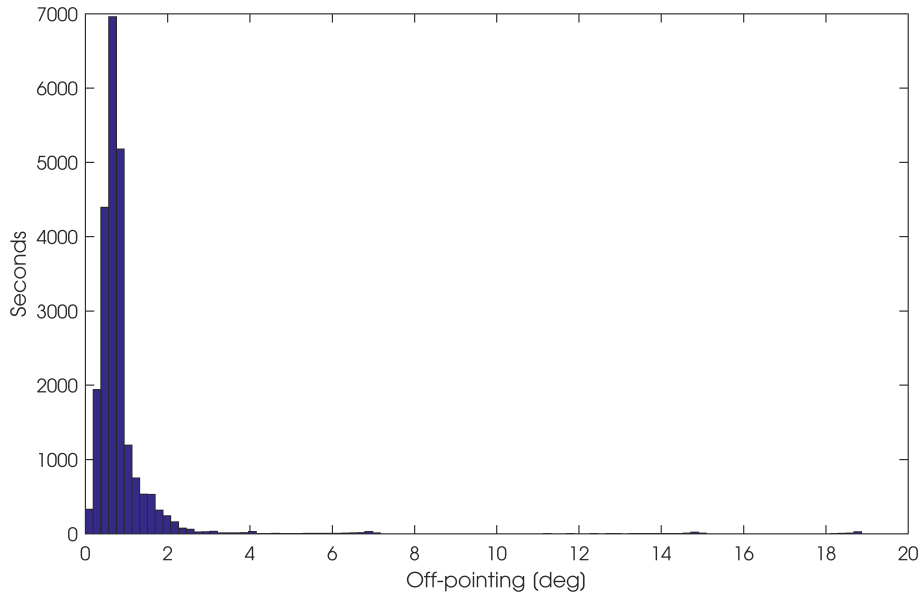

Figure 5.30: Histogram of the angular off-pointing during the ATF-1000 scenario simulation.

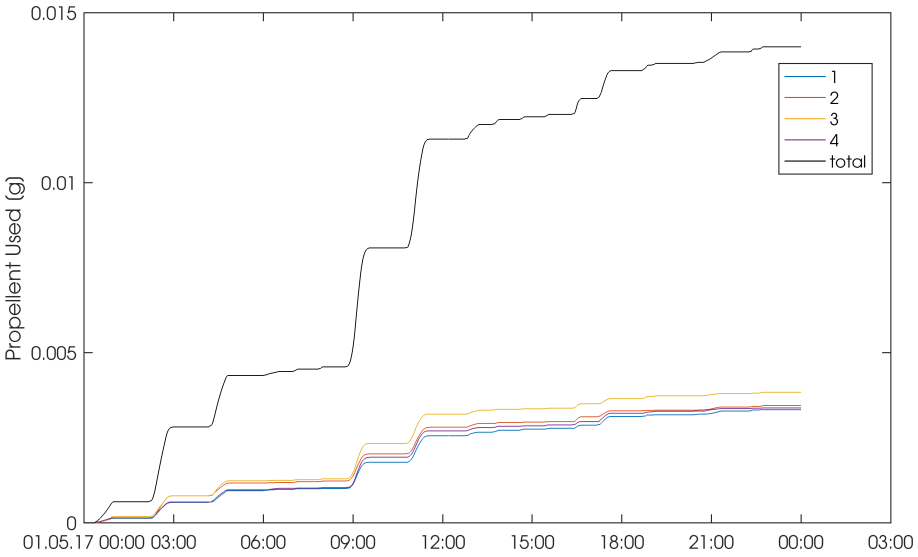

Figure 5.31: Propellant usage during the ATF-1000 scenario simulation.

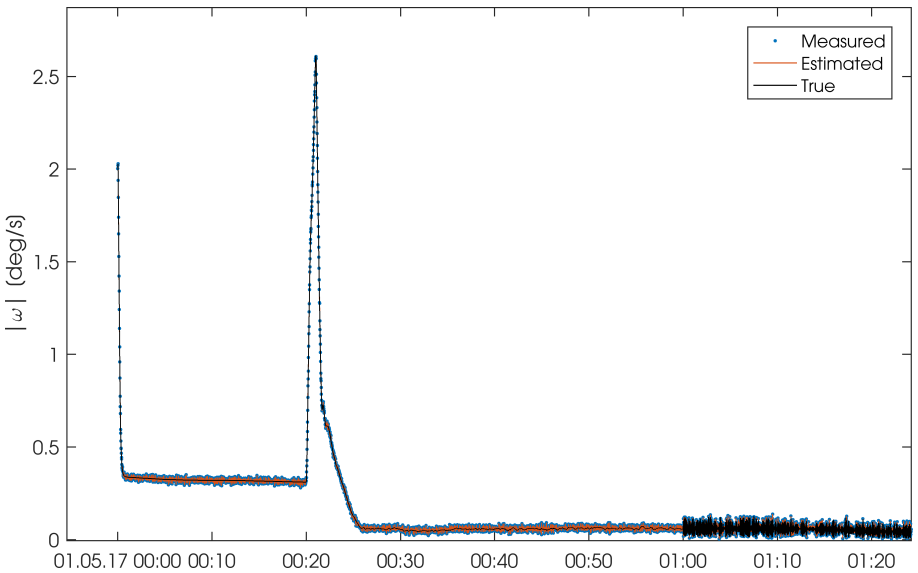

Figure 5.32: Angular rate of the satellite after initialization and during the first orbit control maneuver.

LVLH coordinates is shown in Figure 5.33. There are different maneuvers visible during which the thrust direction in LVLH changes significantly, e.g. at 11:00 UTC and 21:00 UTC.

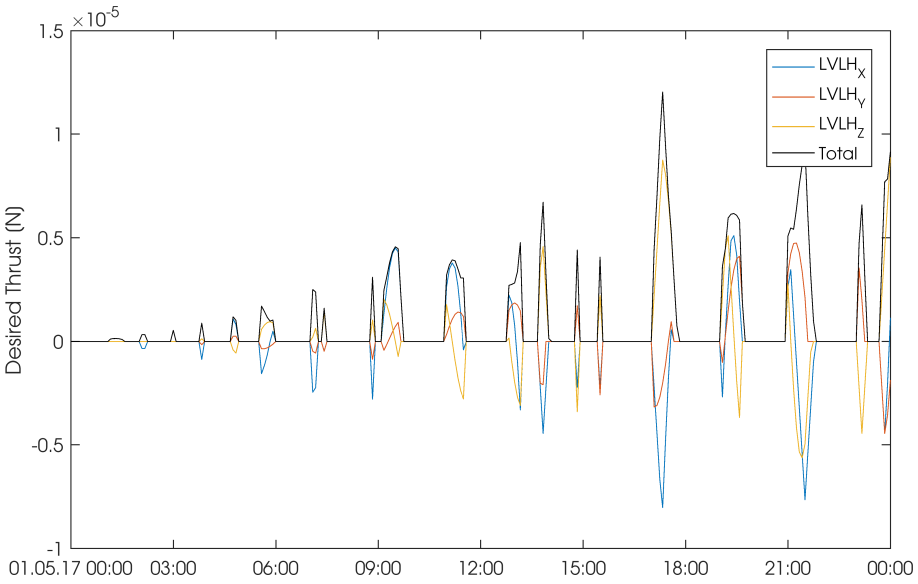

Figure 5.33: Desired thrust profile in LVLH during the ATF-1000 formation change maneuver.

The AOCS controller delivers a total Δv of 0.058 137 m/s and achieves a mean off-pointing of only 1.68 ° which is slightly higher than in the previous scenario. During 98.4 % of the scenario the controller is able to achieve its pointing requirements of better than 10 °.

The weighted Δv in the correct target direction is found to be 0.055 060 m/s which corresponds to 99.1 % of the desired thrust. The total fuel consumption is 0.018 88 g during this day of maneuvers and only 3.2 % of it is used solely for attitude control purposes. The propellant usage is shown in Figure 5.35.

During the scenario the propulsion system consumes an average of 184 mW which is slightly more than in the previous scenario. The angular rates of the satellite behave the same as in the case of the ATF-1000 simulation.

5.5 Summary

The technology advancements of the recent years have prepared the ground for a wide range of future small spacecraft missions in nearly all traditional satellite contexts. The miniaturization process increases the satellite's capabilities also in the key technology field

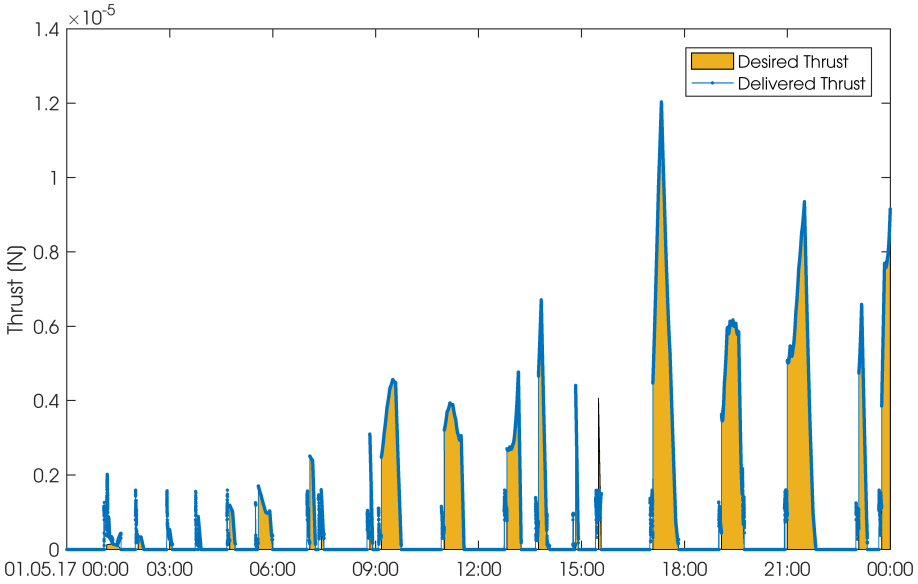

Figure 5.34: Delivered thrust profile during the CWH-500 formation change maneuver.

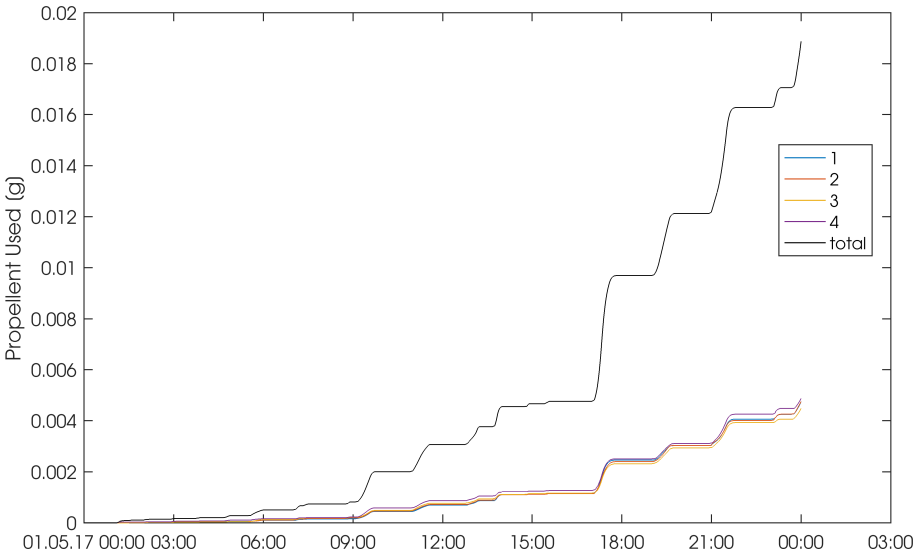

Figure 5.35: Propellant usage during the CWH-500 scenario simulation.

of guidance, navigation, and control. Highly efficient miniature electric propulsion systems have become a major field of development in order to complement the satellite's attitude control capabilities for advanced orbit and formation control.

UWE-4 is set out to test, characterize, and demonstrate the first suitable electric propulsion system for the 1U CubeSat class and thus pushes the boundaries of today's nanosatellite technology even further. The NanoFEEP electric propulsion system developed by TU Dresden has been integrated into the satellite in the most space-saving way and even further enhances the satellite's attitude control system. By their mechanical integration into the CubeSat's rails they can be used for fine thrust vector control and the propulsion system's characterization is achieved via its impact on the satellite's attitude dynamics.

Based on the experience and know-how gained throughout the UWE-3 satellite program an efficient and well-adjusted attitude determination and control system based on an hybrid attitude control using magnetic actuators and the electric propulsion system has been developed and simulated. The attitude estimation accuracy has been improved by an order of magnitude w.r.t. UWE-3 through a new set of attitude sensors. An on-board magnetic dipole estimator is able to detect the magnetic disturbance and evaluate its influence on the attitude controller in order for the satellite to improve its control capabilities and increase its autonomy.

The UWE-4 primary technical mission objective has been well prepared by adjusting the UWE-3 dipole estimation algorithm such that even very low thrust levels of the propulsion system are well detectable. The algorithm ensures a thrust measurement with an accuracy of better than 1 % for thrust levels higher than 1 µN and better than 10 % at thrust levels below.

The hybrid attitude and orbit controller developed here is well suited for the demanding mission requirements of UWE-4. Two formation flying scenarios were simulated in order to show its behavior during, both, simple formation control maneuver and an explicitly demanding control scheme. In both scenarios, the AOCS is able to deliver more than 99 % of the desired acceleration in the target direction and the pointing error is kept within the requirements of less than 10 ° for more than 98 % of the maneuvering time. Moreover, the mean off-pointing during maneuvers is much better than 2 °, despite the fact that the maneuvers were not scheduled outside of the orbit's eclipse periods.

By maximizing the use of magnetic control inherited from UWE-3 the fuel consumption for attitude control stays below 4 % of the total fuel usage during both scenarios. During each scenario less than 0.02 g of propellant, i.e. less than 2 % of the total fuel reserves, was used. The average power consumption of the propulsion system was estimated to be less than 200 mW with peaks of up to 1.5 W.

6

Conclusion

In the years 2009 – 2013 more than 50 % of the launched nano-satellites addressed technology advancements as demonstrator missions while of the current and future missions almost 70 % will target Earth observation/remote sensing or other scientific mission goals (Buchen, 2014). An increasing number of planned constellations of small satellites, also within the commercial communication sector, have been announced throughout the past years. With the increased application of distributed sensor and satellite systems also the requirements on miniature satellite attitude and orbit control systems have increased. Therefore, the trend of applying satellites in the pico-satellite class has lately been weakened in the pursuit of increased performance.

On the other hand, recently developed sensors and actuators and novel control software approaches allow to further increase the performance of pico-satellites in the context of attitude and orbit control. Combined with their cost efficiency and frequent launch options pico-satellites are still an increasingly attractive choice for a variety of space missions.

The work presented here addresses crucial challenges related to attitude and orbit control of pico-satellites and provides generic solutions. Their validity has been demonstrated in-orbit on board of the UWE-3 satellite and further developments towards orbit control have been initiated and are applied to the UWE-4 mission.

The main contributions are

- the in-orbit calibration of a typical set of pico-satellite attitude determination sensors,
- a method to estimate the attitude determination accuracy independently from an external sensor,
- an algorithm to precisely determine the magnetic residual magnetic dipole moment,
- a flexible attitude control architecture,
- a method to measure very low thrust levels of a pico-satellite electric propulsion system and

- a hybrid attitude and orbit control system using magnetorquers and an electric propulsion system.

6.1 Sensor Calibration and Attitude Determination Accuracy Estimation

The in-orbit calibration of attitude sensors usually requires an external reference such as a payload camera or a star tracker. However, pico-satellites often lack the space and power to accommodate these sensors such that a calibration procedure for magnetometers, gyroscopes, and sun-sensors independent from any external reference is required.

The method to calibrate the magnetometers developed and applied to the UWE-3 satellite in orbit is based on the attitude independence of the magnetic field strength. Under random rotation of the satellite the magnetic field is measured in every direction and offsets and mounting in-accuracies cause an attitude correlated mismatch between the measured field strength and its model value. In a post-processing algorithm this mismatch can be minimized which is equivalent to finding the correct offset vector and calibration matrix. The procedure has been applied to the magnetic field data of UWE-3 and provided an accuracy of 1.8 µT (99 % confidence). The magnetic offset was found to have significantly changed with respect to the pre-launch calibration which was an previously unexpected result. However, the magnetization of satellite parts during integration or even launch appears to be an often experienced issue increasing the need for an in-flight magnetometer calibration.

The gyroscope calibration makes use of the previously calibrated magnetometers and estimates the satellite's rotation rate through the change of the magnetic field. This method is applicable as long as the change of the magnetic field due to the satellite's orbital movement happens on a different time scale than the change due to its rotation, i.e. the satellite rotates with an angular rate much larger than $0.125\,^{\circ}/\mathrm{s}$ for a typical Sun-synchronous orbit. The calibration result of this procedure on UWE-3 flight data was found to be in well accordance with the on-ground calibration. This was anticipated since no significant impact of the launch on this type of sensor has been expected.

The same is valid for the sun-sensors but special focus here has to be on the Sun intensity which is difficult to assess during ground tests. The Sun-identification algorithm implemented with an adaptive intensity threshold was found to perform as expected in orbit on board of UWE-3.

Estimating a satellite's attitude determination accuracy also requires some sort of

reference in order to compare the computed attitude solution against. Very small satellites lack this information and therefore the assessment of their attitude determination accuracy is difficult to achieve. Nevertheless, analyzing the consistency of the attitude solution with respect to calibrated sensor data can be used to estimate a worst case assessment of its accuracy. This data analysis has been performed with UWE-3 and was subsequently compared to a simulated attitude determination system in order to validate this approach.

As a result, for UWE-3 a typical attitude estimation accuracy between 2 ° and 6 ° was found. This experience helped the development of a much more precise attitude determination system for the successor satellite UWE-4 which is estimated to achieve an attitude estimation accuracy in the order of 1 °.

6.2 Attitude Disturbance Estimation

The estimation of disturbance torques is necessary to increase a satellite's attitude control system performance. Especially for very small satellites, which in turn are equipped with matching weak attitude control actuators, already very small disturbance torques can easily become a critical issue and mission thread. An assessment of typical disturbance torques shows that the torque due to a residual magnetic dipole is by far the most significant for miniature satellites. On the other hand, magnetic cleanliness programs often are only applied to satellites carrying magnetic payloads and therefore are usually not in place for this class of satellites which further increases the risk of carrying a residual magnetic moment.

A method to precisely estimate the residual magnetic dipole moment of a satellite in orbit has been developed and applied to several satellites, notably UWE-3, ESTCube-1, and BEESAT-2. The algorithm is based on the identification of the satellite's dynamic behavior and matching it with the influence of a static magnetic dipole moment. The analysis is based on magnetic field and gyroscope data usually available on every small satellite.

Using this method, it was shown that UWE-3 carries a static residual dipole moment of about 50 mA m^2 independent from its battery charge, Sun illumination, or reaction wheel activation, thus, most likely linked to a permanently magnetized component. The dipole moment was found constant over the course of more than two years of operations and its orientation in the satellite's body points to the stainless steel antennas as the most probable cause. Its precise measurement allowed to cancel it using the magnetorquers of the satellite of which the magnetic moment was equally measured with the developed algorithm. The identification of the satellite's antennas as most likely cause motivated to change their

material for the successor satellite UWE-4 to Copper-Beryllium.

The application of this method to data provided by ESTCube-1 and BEESAT-2 also revealed residual magnetic moments which were estimated and reported back to the teams. While for ESTCube-1 the dipole moment was so large that it caused a serious thread to the satellite's mission, the residual dipole moment of BEESAT-2 can be taken into account in order to increase the attitude control accuracy.

An on-board residual magnetic moment estimator has been implemented in order for the attitude determination and control system to measure and counteract this disturbance torque autonomously. Simulations show the correct behavior of the system. Focus of this development also was a computational low weight in order for miniature satellites to incorporate it into their ADCS.

6.3 Flexible Attitude Control Architecture

Attitude control systems of traditional satellites are usually tailored to the specific satellite taking into account its shape, mass distribution, and control capabilities. The CubeSat standardization opens the opportunity to design an attitude control architecture flexible enough to support a whole class of satellites and actuators.

The attitude control architecture developed in this work is divided into three layers according to the time scales involved in each specific task. The highest layer ("objective control") is implemented in an efficient scripting language to support virtually any attitude control scheme required for the satellite's mission. Pure rate control algorithms, spin-pointing, and pointing control algorithms can easily be implemented with very little required knowledge about the satellite.

The underlying second layer handles the dynamics of the satellite system including its specific mass distribution and any known disturbance torques. This second layer translates angular acceleration commands from the objective control into a required control torque. By taking into account known disturbances this layer inherently optimizes the control output such that a static disturbance canceling is not required.

The third layer handles the actuators and serves as a driver to deliver the control torque. For this, the required torque can be split up onto any available actuators such as magnetorquers, reaction-wheels, or even attitude control thrusters as shown with the hybrid attitude and orbit control in Chapter 5.4.

The division of the control architecture is according to the specific timescales linked to each task. As such, the objective control acts on the largest timescale involved with update rates in the order of seconds. The second layer requires frequent updates in order

to counteract attitude dependent disturbance torques and re-calculate the required control torque. This usually happens on a timescale in the order of some hundred milli-seconds. The third layer requires permanent updates in order to provide for instance PWM settings for magnetorquers or rate updates to the reaction-wheels. Typical update rates are in the order of some tens of milli-seconds.

The application of this control architecture has been demonstrated on board of the UWE-3 satellite. The successful optimal counteraction of the satellite's residual magnetic dipole moment was shown as well as several control approaches. A highly efficient detumbling, rate control, and spin-axis control purely based on magnetic actuators was demonstrated in orbit despite the satellite's large magnetic disturbance.

6.4 Thrust Measurement of a Miniature Electric Propulsion System

Electric propulsion systems generate only very low thrust, typically in the order of mN, but achieve to date the highest mass efficiency of any propulsion system. Naturally, these propulsion systems are most suitable for very low mass satellites. The development of electric propulsion systems for CubeSats has therefore shown some major progress in the recent years.

In this context the electric propulsion system NanoFEEP has been developed by TU Dresden and shall be tested in orbit by the satellite UWE-4. With its high efficiency the propulsion system can provide up to 60 m/s of Δv to a 1U CubeSat with only 1 g propellent. However, due to its very low thrust of only some µN orbit control maneuvers have a very long duration. Thus, it is very difficult to measure the system's performance at various thrust levels via the change of the satellite's orbit.

However, the integration of the propulsion system also as attitude control thrusters allows to generate torques. Having established an algorithm to determine the magnetic disturbance of a satellite this method can be used to determine the torque provided by the electric propulsion system. From this it is possible to deduct the system's thrust level and efficiency.

It was shown in simulation that this method is suitable to estimate the thrust level to an accuracy of 1 % for thrust levels higher than 1 µN. It was found that there is an optimal maneuver duration for this method depending on the thrust level in test. Typically, an activation time of 10 min is sufficient to achieve an accurate thrust estimation while longer maneuvers tend to decrease the estimation accuracy due to larger spin-rates of the satellite.

6.5 Hybrid Attitude and Orbit Control

Orbit control requires successful attitude control in order to achieve the correct thrust vector pointing. For miniature satellites it is already difficult to integrate a propulsion system and the required attitude control actuators such as reaction-wheels into the limited space but to operate both at the same time usually is virtually impossible due to the satellite's power constraints. Therefore, it is favorable to achieve attitude and orbit control solely with the propulsion system and low footprint actuators such as magnetorquers.

The integration of a miniature electric propulsion system into the CubeSat's bars will enable the UWE-4 satellite to use the thrusters also as attitude actuators. In order to achieve thrust vector pointing an efficient hybrid attitude control system employing magnetorquers and the electric propulsion system itself has been developed. It is based on the flexible attitude control architecture developed in UWE-3 and optimizes the use of the magnetorquer, thus, minimizes the propulsion system's fuel consumption.

It was shown in several simulations that the system is suitable to provide precise thrust vector pointing for a variety of orbit control scenarios, including formation flying scenarios.

6.6 Future Perspectives

The recent developments in the area of miniature satellites, including the work presented here, has further increased the performance of future CubeSats. A flexible and precise attitude control paired with orbit control capabilities will open up new application scenarios for this satellite class. Especially in the domain of satellite formations, which are now in realistic distance also for small CubeSats, new opportunities arise for joint Earth observation, distributed communication networks, and even fractionated scientific instruments.

The cooperation of several satellites in a formation will create new perspectives for a broad spectrum of applications in the fields of Earth Observation (EO), navigation and communication, and scientific instrumentation. With the ever increasing technical capabilities of miniature satellites even demanding missions become feasible while challenges remain to be addressed in future missions. These are especially linked to attitude and orbit control, relative navigation, and precise pointing of miniature spacecraft such that future satellites can achieve their mission goal in cooperation. "The advantages are lower cost, better scalability and higher reliability." (Schilling et al., 2015)

6.6.1 Earth Observation

In the field of Earth Observation the joint observation of a target on ground from different aspect angles and directions from space opens up possibilities in the stereoscopic observation of large objects or multi-spectral imaging of wide areas.

Large objects that need stereoscopic monitoring are for instance volcanic ash clouds that have, in the past, shown their large influence on infrastructure services, such as air traffic or solar power plants. Their observation from space would enable global monitoring and more precise measurement of their density, cloud top height, and traveling speed (Zakšek et al., 2013). In the post-analysis of the 2010 Eyjafjallajökull volcanic eruption on Iceland it was stated by Zehner (2010) that ”(t)he largest uncertainty in the ability of numerical models to predict the spread of volcanic ash, and hence to advise aviation regulators, is in the observations of the eruption itself. Specifically, more accurate information on how high the ash is being emplaced at the source, the mass eruption rate and near source plume dynamics leads to better constraints on downstream ash locations.”

Nogueira et al. (2016) elaborate on measuring the cloud’s spatial distribution (especially its top height) and its temporal evolution with the help of a miniature satellite formation as depicted in Figure 6.1.

Another possible EO application scenario is the cooperation of miniature satellites with a larger radar satellite. In this scenario, the primary radar illuminates the scene underneath the formation and operates in its traditional mode while the formation of small satellites only receives the radar reflection as illustrated in Figure 6.2. By fusing precise relative position information with the radar signal the original radar image can be augmented and additional information can be obtained.

6.6.2 Navigation and Communication

While the main commercial satellite communication services typically require larger power budgets for their broadband applications, cooperative small satellites can be used in future to monitor existing radio sources in order to ensure interference free communication services for all entities. Concerns that the planned mega-constellations such as OneWeb or Starlink may affect existing communication services have been raised in the past (e.g. by de Selding (2015)) and measurements already with UWE-3 could show the significance of interference monitoring with CubeSats.

Figure 6.3 shows the signal strength (RSSI in dBm) as measured by the UWE-3 UHF transceivers over a period of 5 days in 2015. Clearly visible are noise sources in certain frequency bands in Europe and especially East Asia that are able to significantly disturb the

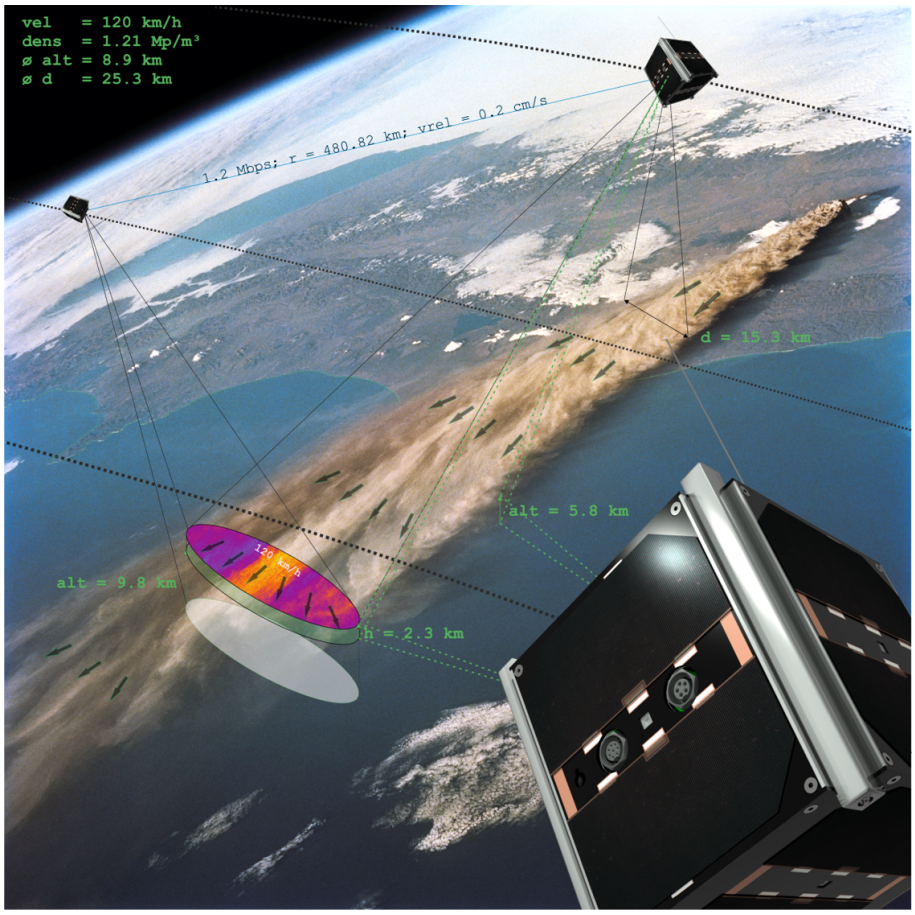

Figure 6.1: Conceptual design of an ash cloud monitoring mission with a formation of CubeSats.

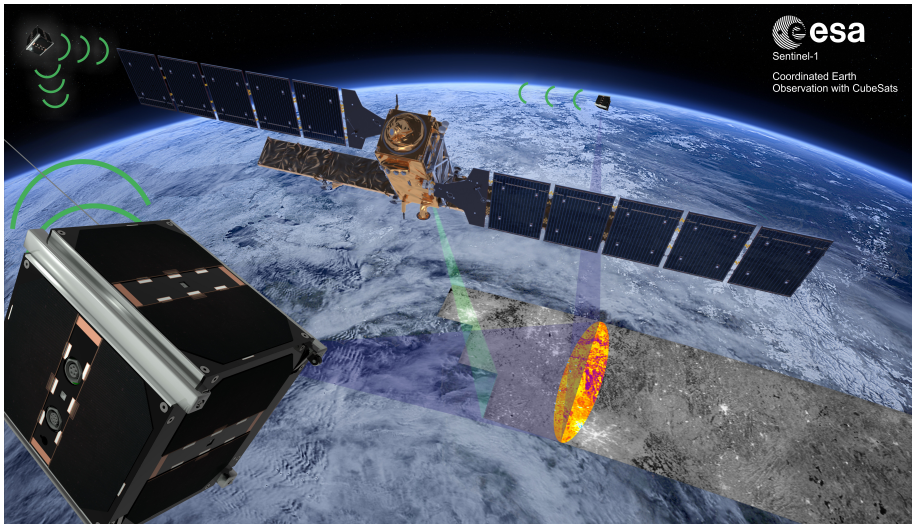

Figure 6.2: Conceptual design of a cooperative radar observation of CubeSats together with a primary illumination satellite (e.g. ESA Sentinel).

radio communication. With the help of formation flying satellites the precise locations of the radio jamming sources and their exact frequency can be measured either by triangulation or even a distributed signal wave analysis (precise correlation analysis). Such a mission could help to better coordinate the limited frequency space for orbital communication services in future and to detect threats for existing service providers.

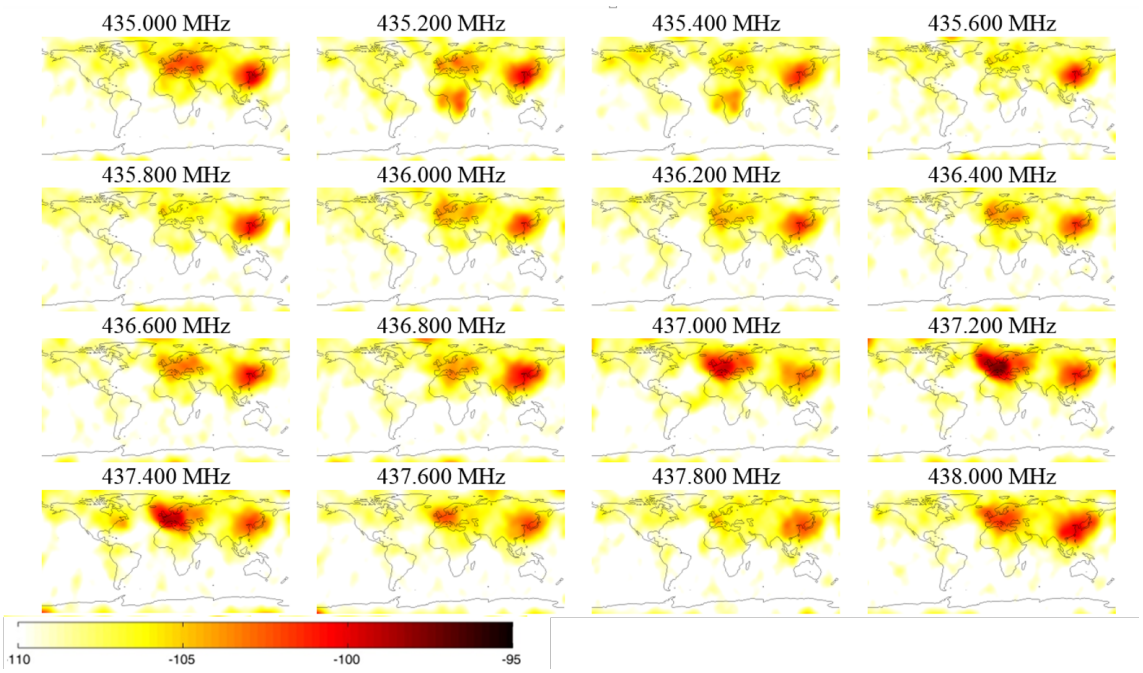

Figure 6.3: Interference map obtained by measurements of the RSSI in dBm of the on-board UHF transceivers of UWE-3 in 2015. (Busch et al., 2015)

6.6.3 Fractionated Scientific Instrumentation

The idea to divide a large scientific instrument into smaller pieces in order to reduce launch costs, increase redundancy, or even enable certain scientific observations is currently in discussion for a variety of space missions. Prominent examples are the ESA missions Proba-3 (fractionated coronagraph) and the former ESA mission Darwin (fractionated telescope). However, the technical requirements for such missions are so high that even larger satellite missions such as Darwin fail to be implemented (European Space Agency, 2009).

A mission concept of a fractionated miniature satellite mission is the NetSat-4G (Global GeomaGnetic Gradiometry) concept. It is similar to ESA's Swarm (Friis-Christensen et al., 2006) and NASA's ST-5 mission from 2006 (Purucker et al., 2007) and intends to precisely measure the Earth's geomagnetic field (Nogueira et al., 2015). The concept foresees a

formation of four miniature satellites equipped with precise vector magnetometers that fly in a Cartwheel-Helix formation at low altitude. By differential combination of the satellite's sensor readings geomagnetic gradients can be measured in all three dimensions without any time ambiguity. Thus, a full gradiometry mission could be established for the first time. The most stringent requirement, apart from the scientific instrument's precision, is on the satellite's attitude determination accuracy. In order to precisely combine the satellite's magnetic field vector readings, the actual satellite attitude needs to be well known. Any uncertainty degrades the scientific value of the data which is why the use of star trackers was considered inevitable. While the NetSat mission is still in development this particular scientific mission has been ruled out as it poses too many constraints on the satellite platform which in itself is the main focus of the formation flight demonstration mission NetSat.

The scientific mission concepts in general have tight requirements towards the satellite platform which are to date out of scope for miniature satellites. However, formation flight aspects and autonomy concepts tested on very small satellites create a valuable experience for this type of future missions. The implementation of the hybrid attitude and orbit controller is an indispensable cornerstone for formation control of miniature satellites with highly efficient electrical propulsion systems.

List of Tables

List of Figures

Bibliography of the Author

Bangert, P., Kramer, A., Schilling, K., UWE-4: Integration State of the First Electrically Propelled 1U CubeSat, 31st Annual AIAA/USU Conference on Small Satellites, Logan, USA, August 2017

Kramer, A., Azari, P., **Bangert, P.**, Schilling, K., Orbit control on the Pico-Satellite UWE 4 using a NanoFEEP propulsion system and a directive adaptive guidance algorithm, 35th International Electric Propulsion Conference, Antlanta, USA, October 2017

Kramer, A., **Bangert, P.**, Paries, F., Schilling, K., Preparations for Orbit control on the Pico-Satellite UWE-4, 11th IAA Symposium on small satellites for Earth observation, Berlin, 2017

Zagorski, P., **Bangert, P.**, Gallina, A., Identification of the orbit semi-major axis using frequency properties of onboard magnetic field measurements, Aerospace Science and Technology, http://dx.doi.org/10.1016/j.ast.2017.03.024, March 2017

Pietzka, M., **Bangert, P.**, Kramer, A., Lebeda, A., Schilling, K., Schein, J., Propulsion System for CubeSat Formation Flight, in: Busch, Schilling (eds.) Technology for Small Satellite Research, IAA. pp. 17-26 , 2016

Bangert, P., Dombrovski, S., Kramer, A., Schilling, K., UWE-4: Orbit Determination and Control on a Pico-Satellite scale, IAA Book Series: Small Satellites – Programs, Missions, Technologies and Applications, Volume 1, Number 6, ISBN/EAN IAA : 978-2-917761-49-6, 2016

Bangert, P., Busch, S., Kramer, A., Schilling, K., Preparation of Papers for IFAC Conferences & Symposia: Guidance, Navigation, and Control for Future Miniature Satellite Formations: Current Limitations and Impending Advancements, 20th IFAC Symposium on Automatic Control in AerospaceACA, Sherbrooke, Quebec, Canada, August 2016

Bangert, P., Dombrovski, S., Kramer, A., Schilling, S., UWE-4: Advances in the Attitude and Orbit Control of a Pico-Satellite, The 4S Symposium, Valletta, Malta, Mai 2016

Scharnagl, J., Kleinschrodt, A., Freimann, A., Ravandoor, K., **Bangert, P.**, Srinivasan, L., Schilling, K., Nanosatellite Constellations for Large-Scale Railway Transportation Monitoring, Proceedings of the 3rd IAA Conference on University Satellite Missions and CubeSat Workshop, Rome, Italy 2015

Bangert, P., Busch, S., Dombrovski, S., Kramer, A., UWE - Lessons Learned and Future Perspectives, 3rd 3rd IAA Conference on University Satellite Missions and CubeSat Work-

shop, Rome, 2015

Bock, D., Kramer, A., **Bangert, P.**, Schilling, K., Tajmar, M., NanoFEEP on UWE Platform - Formation Flying of CubeSats, Joint Conference of 30th ISTS, 34th IEPC, and 6th NSat, Kobe, Japan, 2015

Dadhich, S., **Bangert, P.**, Schilling, K., Attitude Control of UWE-4 for Orbit Correction During Formation Flying, 6th NSat, Kobe, Japan, 2015

Schilling, K., **Bangert, P.**, Busch, S., Dombrovski, S., Freimann, A., Kleinschrodt, A., Kramer, A., Nogoueira, T., Ris, D., Scharnagl, J., Tzschichholz, T., Netsat: A Four Pico/Nano-Satellite Mission For Demonstration Of Autonomous Formation Flying, Proceedings 66. IAC Congress, Jerusalem IAC-15-D1.4.2 . 2015

Dombrovski, S., **Bangert, P.**, Introduction of a new Sandbox Interpreter Approach for Advanced Satellite Operations and Safe On-Board Code Execution, Proceedings 66. IAC Congress, Jerusalem, 2015

Bangert, P., Busch, S., Schilling, K., In-Orbit Performance of the Pico-Satellite UWE-3, 10th IAA Symposium on Small Satellites for Earth Observation, Berlin, 2015

Arunkumar, R., **Bangert, P.**, Bock, D., Pietzka, M., Tajmar, M., Schilling, K., Structural Design, Integration of Micro Propulsion units and Thermal Analysis of UWE (University of Wurzburg's Experimental Satellites) Platform, 6th European Conference for Aeronautics and Space Sciences (EUCASS), 2015

Bock, D., **Bangert, P.**, Schilling, K., Tajmar, M., NanoFEEP on UWE platform - Formation Flying of CubeSats using Miniaturized Field Emission Electric Propulsion Thrusters, IEPC, Kobe, Japan, 2015

Busch, S., **Bangert, P.**, Dombrovski, S., Schilling, K., UWE-3, In-Orbit Performance and Lessons Learned of a Modular and Flexible Satellite Bus for Future Pico-Satellite Formations, Acta Astronautica, Vol. 117. 2015, pp.73-89

Busch, S., **Bangert, P.**, Dombrovski, S., Schilling, K., UWE-3, In-Orbit Performance and Lessons Learned of a Modular and Flexible Satellite Bus for Future Picosatellite Formations, 65th International Astronautical Congress, Toronto, September 2014

Busch, S., **Bangert, P.**, Schilling, K., Attitude Control Demonstration for Pico-Satellite Formation Flying by UWE-3, Small Satellite Systems and Services Symposium (4S), May 2014, Majorca, Spain

Bangert, P., Busch, S., Schilling, K., Performance Characteristics of the UWE-3 Miniature Attitude Determination and Conctrol System, 2nd IAA Conference on Dynamics and

Control of Space Systems (DyCoSS), March 2014, Rome, Italy

Busch, S., **Bangert, P.**, Reichel, F., Schilling, K., The UWE Satellite Bus, a Modular and Flexible Architecture for Future Picosatellite Formations, 64. IAC Congress, Beijing, China, 2013

Busch, S., Schilling, K., **Bangert, P.**, Reichel, F., Robust Satellite Engineering in Educational Cubesat Missions at the Example of the UWE-3 Project, 19th IFAC Symposium on Automatic Control in Aerospace, September 2013, Würzburg, Germany

Reichel, F., **Bangert, P.**, Busch, S., Schilling, K., The Attitude Determination and Control System of the Picosatellite UWE-3, 19th IFAC Symposium on Automatic Control in Aerospace, September 2013, Würzburg, Germany

Busch, S., Reichel, F., **Bangert, P.**, Schilling, K., The UWE Satellite Bus, a Modular and Flexible Architecture for Future Picosatellite Formations, 64th International Astronautical Congress, September 2013, Beijing, China

References

Aicher, M. (2016). Implementation and performance estimation of MEMS based Inertial Measurement Units for the Attitude and Orbit Control System of the CubeSat UWE-4. Bachelor's Thesis, University Würzburg.

Bangert, P. (2012). Attitude Determination System of UWE-3 – Development, Test, and Verification. Master's thesis, University Würzburg, Lulea Technical University.

Bangert, P., Busch, S., Dombrovski, S., Kramer, A., and Schilling, K. (2015a). UWE – Lessons Learned and Future Perspectives. In *Proceedings of the 3rd IAA Conference on University Satellite Missions and CubeSat Workshop*, Rome, Italy.

Bangert, P., Busch, S., Kramer, A., and Schilling, K. (2016). Preparation of papers for ifac conferences & symposia: Guidance, navigation, and control for future miniature satellite formations: Current limitations and impending advancements. *20th IFAC Symposium on Automatic Control in Aerospace ACA 2016*, 49(17):290–295.

Bangert, P., Busch, S., and Schilling, K. (2014). Performance Characteristics of the UWE-3 Miniature Attitude Determinatin and Control system. In *Advances in the Astronautical Sciences*, volume 153, pages 513–526, Rome. American Astronautical Scociety.

Bangert, P., Busch, S., and Schilling, K. (2015b). In-Orbit Performance of the Pico-Satellite UWE-3. In *10th IAA Symposium on Small Satellites for Earth Observation*, Berlin Germany.

Bangert, P., Reichel, F., Busch, S., and Schilling, K. (2012). *Design-und Verifikationstests des Lageerkennungs-und Lageregelungssystems für den Picosatelliten UWE-3*. Deutsche Gesellschaft für Luft-und Raumfahrt-Lilienthal-Oberth eV.

Bock, D. (2016). NanoFEEP specification data. Personal Communication.

Bock, D., Bethge, M., and Tajmar, M. (2014). Highly miniaturized FEEP thrusters for CubeSat applications. In *4th Spacecraft Propulsion Conference*, Cologne, Germany.

Bock, D., Kramer, A., Bangert, P., Schilling, K., and Tajmar, M. (2015). NanoFEEP on UWE platform – Formation Flying of CubeSats using Miniaturized Field Emission Electric Propulsion Thrusters. In *Joint Conference of 30th International Symposium on Space Technology and Science, 34th International Electric Propulsion Conference and 6th Nano-satellite Symposium*, Hyogo-Kobe, Japan.

Bock, D., Kramer, A., Bangert, P., Schilling, K., and Tajmar, M. (2016). NanoFEEP - Highly Miniaturized FEEP Propulsion System for Attitude and Orbit Control of CubeSats. In *Proceedings of the 5th Spacecraft Propulsion Conference*.

Buchen, E. (2014). SpaceWorks' 2014 Nano/Microsatellite Market Assessment. In *28th Annual AIAA/USU Conference on Small Satellites*.

Busch, S. (2015). CubeSat Subsystem Interface Definition. UNISEC Europe.

Busch, S., Bangert, P., Dombrovski, S., and Schilling, K. (2014a). In-Orbit Performance and Lessons Learned of a Modular and Flexible Satellite Bus for Future Picosatellite Formations. In *Proceedings of the 65. IAC Congress, Toronto, Canada*.

Busch, S., Bangert, P., Dombrovski, S., and Schilling, K. (2015). Uwe-3, in-orbit performance and lessons learned of a modular and flexible satellite bus for future pico-satellite formations. *Acta Astronautica*, 117:73 – 89.

Busch, S., Bangert, P., and Schilling, K. (2014b). Attitude Control Demonstration for Pico-Satellite Formation Flying by UWE-3. In *4S Symposium*.

de Selding, P. B. (2015). OneWeb Gets (Slide) Decked by Competitor at CASBAA. *http://spacenews.com*.

Dombrovski, S.; Bangert, P. (2015). Introduction of a new sandbox interpreter approach for advanced satellite operations and safe on-board code execution. In *66th International Astronautical Congress*, Jerusalem, Israel.

Ehrpais, H., Kütt, J., Sünter, I., Kulu, E., Slavinskis, A., and Noorma, M. (2016). Nanosatellite spin-up using magnetic actuators: Estcube-1 flight results. *Acta Astronautica*, 128:210 – 216.

European Space Agency (2009). Darwin: Study ended, no further activities planned. http://www.esa.int/Our_Activities/Space_Science/Darwin_overview.

European Space Agency: eoPortal – Sharing Earth Observation Resources (2017). https://directory.eoportal.org/web/eoportal/home.

European Space Agency: eoPortal – Sharing Earth Observation Resources (2018a). BRIght-star Target Explorer Constellation. https://directory.eoportal.org/web/eoportal/satellite-missions/b/brite-austria. Accessed: 2018-03-22.

European Space Agency: eoPortal – Sharing Earth Observation Resources (2018b). GOMX-3. https://directory.eoportal.org/web/eoportal/satellite-missions/g/gomx-3. Accessed: 2018-03-22.

European Space Agency: eoPortal – Sharing Earth Observation Resources (2018c). Planet Labs - Flock Imaging Constellation. https://directory.eoportal.org/web/eoportal/satellite-missions/f/flock-1. Accessed: 2018-03-22.

Flatley, T., Morgenstern, W., Reth, A., and Bauer, F. (1997). A B-Dot Acquisition Controller for the RADARSAT Spacecraft. In *Flight Mechanics Symposium, NASA Conference Publication*, pages 79–90.

Friis-Christensen, E., Lühr, H., and Hulot, G. (2006). Swarm: A constellation to study the Earth's magnetic field. *Earth, Planets and Space*, 58(4):351–358.

Helvajian, H. and Janson, S. (2009). *Small Satellites: Past, Present, and Future*. AIAA.

Inamori, T. and Nakasuka, S. (2012). Application of Magnetic Sensors to Nano and Micro-Satellite Attitude Control Systems. In Kuang, D. K., editor, *Magnetic Sensors-Principles and Applications*. InTech.

ISIS - Innovative Solutions In Space (2017). *ISIPOD CubeSat Deployer*.

Kiefel, P. (March 2011). Entwicklung, Kalibrierung und Verifikation eines Kalmanfilter basierten Lageerkennungssystem für den Picosatelliten UWE–3. Master's thesis, Julius-Maximilians-Univesität Würzburg.

Kiefel, P., Busch, S., Dröge, W., and Schilling, K. (2011). Implementation, Calibration and Verification of a Kalman Filter based Attitude Determination System for the Picosatellite UWE-3. In *Proceedings of 8th Int'l ESA Conference on Guidance & Navigation Control Systems*.

Kramer, A., Bangert, P., Paries, F., and Schilling, K. (2017). Preparations for Orbit control on the Pico-Satellite UWE-4. In *11th IAA Symposium on Small Satellites for Earth Observation*.

Latt, S., Slavinskis, A., Ilbis, E., Rosta, R., and Krömer, O. (2014). ESTCube-1 nanosatellite for electric solar wind sail in-orbit technologydemonstration. *Proceedings of the Estonian Academy of Sciences*, 63(2S):200–209.

Martinez-Sanchez, M. and Lozano, P. (Spring 2015). 16.522 Space Propulsion. Massachusetts Institute of Technology: MIT OpenCourseWare. License: Creative Commons BY-NC-SA.

MathWorks (2016). *MATLAB 2016b Documentation*.

Noca, M. and Ivanov, A. (2010). SwissCube Status 02 May 2010. EPFL Space Center.

Nogueira, T., Dombrovski, S., Busch, S., Schilling, K., Zakšek, K., and Hort, M. (2016). Photogrammetric Ash Cloud Observations by Small Satellite Formations. In *Metrology for Aerospace (MetroAeroSpace), 2016 IEEE*, pages 450–455. IEEE.

Nogueira, T., Scharnagl, J., Kotsiaros, S., and Schilling, K. (2015). NetSat-4G A four nano-satellite formation for global geomagnetic gradiometry. In *10th IAA Symposium on Small Satellites for Earth Observation*.

Picone, J. M., Hedin, A. E., Drob, D. P., and Aikin, A. C. (2002). Nrlmsise-00 empirical model of the atmosphere: Statistical comparisons and scientific issues. *Journal of Geophysical Research: Space Physics*, 107(A12):SIA 15–1–SIA 15–16. 1468.

Purucker, M., Sabaka, T., Le, G., Slavin, J., Strangeway, R., and Busby, C. (2007). Magnetic field gradients from the st-5 constellation: Improving magnetic and thermal models of the lithosphere. *Geophysical Research Letters*, 34(24).

Reichel, F. (2012). Attitude Control System of UWE–3. Master Thesis, Julius-Maximilians-Univesität Würzburg.

Reichel, F., Bangert, P., Busch, S., Ravandoor, K., and Schilling, K. (2013). The Attitude Determination and Control System of the Picosatellite UWE-3. In *19th IFAC Symposium on Automatic Control in Aerospace, Würzburg, Germany*.

Richard, M., George, F., and Ivanov, A. (2011). SwissCube... 2 years in Space. EPFL Space Center.

Rotteveel, J. and Bonnema, A. (2017). Launch Services 101, Managing a 101 CubeSat Launch Manifest on PSLV-C37. In *14th Annual Pre-Conference Workshop, Small Satellite Conference*, Logan, Utah.

Schalkowsky, S. and Harris, H. (1969). NASA Space Vehicle Design Criteria Monograph (Guidance and Control): Spacecraft Magnetic Torques. *NASA SP-8018, March*.

Schilling, K., Bangert, P., Busch, S., Dombrovski, S., Freimann, A., Kleinschrodt, A., Kramer, A., Nogoueira, T., Ris, D., Scharnagl, J., and Tzschichholz, T. (2015). Netsat: A Four Pico/Nano-Satellite Mission for Demonstration of Autonomous Formation Flying. *Proceedings 66. IAC Congress, Jerusalem IAC-15-D1.4.2*.

Scholz, A., Ley, W., Dachwald, B., Miau, J., and Juang, J. (2010). Flight results of the compass-1 picosatellite mission. *Acta Astronautica*, 67(9):1289 – 1298.

Slavinskis, A., Ehrpais, H., Kuuste, H., Sünter, I., Viru, J., Kütt, J., Kulu, E., and Noorma, M. (2016). Flight results of ESTCube-1 attitude determination system. *Journal of Aerospace Engineering*, 29(1):04015014.

Slavinskis, A., Pajusalu, M., Kuuste, H., Ilbis, E., Eenmae, T., Sunter, I., Laizans, K., Ehrpais, H., Liias, P., Kulu, E., Viru, J., Kalde, J., Kvell, U., Kutt, J., Zalite, K., Kahn, K., Latt, S., Envall, J., Toivanen, P., Polkko, J., Janhunen, P., Rosta, R., Kalvas, T., Vendt, R., Allik, V., and Noorma, M. (2015). ESTCube-1 in-orbit experience and lessons learned. *IEEE Aerospace and Electronic Systems Magazine*, 30(8):12–22.

Swartwout, M. (2018). CubeSat Database. https://sites.google.com/a/slu.edu/swartwout/home/cubesat-database. Accessed: 2018-03-24.

Swartwout, M. A. (2017). CubeSats and Mission Success: 2017 Update. presented at the 2017 Electronic Technology Workshop, NASA Electronic Parts and Packaging Program (NEPP), NASA Goddard Space Flight Center.

Tajmar, M., Genovese, A., and Steiger, W. (2004). Indium field emission electric propulsion microthruster experimental characterization. *Journal of Propulsion and Power*, 20(2):211–218.

Technical University of Berlin (2017). BEESAT-2 Website.

Wertz, J. (1978). *Spacecraft Attitude Determination and Control*. D. Reidel Publishing Company, Dordrecht, Holland.

Wertz, J. and Larson, W. (1999). *Space Mission Analysis And Design*. Microcosm Press, Inc. and W.J. Larson.

Zakšek, K., Hort, M., Zaletelj, J., and Langmann, B. (2013). Monitoring volcanic ash cloud top height through simultaneous retrieval of optical data from polar orbiting and geostationary satellites. *Atmospheric Chemistry and Physics*, 13(5):2589–2606.

Zehner, C. (2010). Monitoring volcanic ash from space: Proceedings of the ESA-EUMETSAT Workshop on the 14 April to 23 May 2010 Eruption at the Eyjafjoll Volcano, South Iceland. *ESA Publ. STM*, 280.

The author appreciated the support for UWE-3 and UWE-4 by the German national space agency DLR (Raumfahrt-Agentur des Deutschen Zentrums für Luft- und Raumfahrt e.V.) by funding from the Federal Ministry of Economic Affairs and Energy by approval from German Parliament with reference 50 RU 0901 and 50 RU 1501, respectively.